CHARACTERIZATION OF THE FIRST STAGE PROTOTYPE OF THE TIFFIN DETECTOR

by

Rachel Ashley

M.Phys., University of Liverpool, 2010

Thesis submitted in partial fulfillment
of the requirements for the degree of

Master of Science

in the
Department of Chemistry
Faculty of Science

SIMON FRASER UNIVERSITY
Summer 2014

APPROVAL

Name: Rachel Ashley

Degree: Master of Science

Title of Thesis: Characterization of the First Stage Prototype of the TIFFIN Detector

Examining Committee: Dr. Michael Eikerling, Professor
Chair

Dr. Krzyzstof Starosta, Senior Supervisor
Associate Professor

Dr. Adam Garnsworthy, Supervisor
Research Scientist, TRIUMF

Dr. Corina Andreoiu, Supervisor
Assistant Professor

Dr. Lee Hanlan, Supervisor
Associate Chair and Senior Lecturer

Dr. Paul Percival, Internal Examiner
Professor, Department of Chemistry

Date Approved: 16th July 2014

Partial Copyright Licence

The author, whose copyright is declared on the title page of this work, has granted to Simon Fraser University the non-exclusive, royalty-free right to include a digital copy of this thesis, project or extended essay[s] and associated supplemental files ("Work") (title[s] below) in Summit, the Institutional Research Repository at SFU. SFU may also make copies of the Work for purposes of a scholarly or research nature; for users of the SFU Library; or in response to a request from another library, or educational institution, on SFU's own behalf or for one of its users. Distribution may be in any form.

The author has further agreed that SFU may keep more than one copy of the Work for purposes of back-up and security; and that SFU may, without changing the content, translate, if technically possible, the Work to any medium or format for the purpose of preserving the Work and facilitating the exercise of SFU's rights under this licence.

It is understood that copying, publication, or public performance of the Work for commercial purposes shall not be allowed without the author's written permission.

While granting the above uses to SFU, the author retains copyright ownership and moral rights in the Work, and may deal with the copyright in the Work in any way consistent with the terms of this licence, including the right to change the Work for subsequent purposes, including editing and publishing the Work in whole or in part, and licensing the content to other parties as the author may desire.

The author represents and warrants that he/she has the right to grant the rights contained in this licence and that the Work does not, to the best of the author's knowledge, infringe upon anyone's copyright. The author has obtained written copyright permission, where required, for the use of any third-party copyrighted material contained in the Work. The author represents and warrants that the Work is his/her own original work and that he/she has not previously assigned or relinquished the rights conferred in this licence.

Simon Fraser University Library
Burnaby, British Columbia, Canada

revised Fall 2013

Abstract

A single-sided, gridded, gas ionization chamber with digital read-out and a dedicated gas-flow control system was built as the first stage prototype of the Twin Ionization chamber for Fission Fragment Investigation (TIFFIN) detector. The detector was tested with an α-particle source, and the operating parameters of the detector were probed to establish its response.

Investigation of the operating parameters of the prototype led to an energy resolution of 8.69(1)% when running the detector with a gas mixture of 90% argon and 10% methane (referred to as P10) at a gas pressure of 1800 Torr. Digital read-out of the signal allowed signal risetimes to be successfully evaluated on an event-by-event basis. However, electric field inconsistencies limited the energy resolution achievable. An electric field cage should be installed to encourage a uniform field between the detector plates.

The Nuclear Science Laboratories at Simon Fraser University are embarking upon a program of research to address various topics of interest to modern science such as the origin, production, composition and structure of exotic, neutron-rich isotopes. The study of fission fragments is an effective way to investigate neutron-rich nuclei. Ionization chambers are an appropriate and versatile tool with which to study fission fragments, and can be built in such a way as to allow energy, mass and charge measurements of both fragments. The single-sided prototype is a crucial first step towards the final design which will allow such measurements.

Keywords: Twin ionization chamber; fission fragment detection; alpha particle detection; detector development; Frisch grids

To Carl, for believing in me when I didn't believe in myself.

"If an expert is one who has made every conceivable mistake,
I became very expert in this field."

— *What Little I Remember*, OTTO FRISCH, *1979*

Contents

List of Tables

List of Figures

Chapter 1

Introduction

The Nuclear Science Laboratories at Simon Fraser University are embarking upon a program of research to address various topics of interest to modern science such as the origin, production, composition and structure of exotic, neutron-rich isotopes. There are two main ways to achieve this goal: to compete for beam time at national accelerator facilities such as the Tri-University Meson Facility (TRIUMF) [1] or to utilize spontaneous and neutron-induced fission in one's own laboratory. The Nuclear Science groups at SFU have programs engaging in both routes but this thesis is concerned only with the latter.

Combining heavy charged particle detection with γ-ray detection and fission sources will allow the collection of experimental information on many isotopes of great interest to nuclear science. In addition, the availability of this combination of detection systems in-house means long measurements can be taken which may not be possible at a national facility. The Twin Ionization chamber for Fission Fragment Investigation (TIFFIN) will provide a means of charged particle detection whilst the recent arrival of the 8π spectrometer array [2] will provide γ-ray detection and the Sub-critical Intense Multiplier Of Neutrons (SIMON) neutron generator will be used to generate neutrons for inducing fission.

1.1 Fission

1.1.1 Energy Balance in the Nucleus

The nucleus of an atom contains protons and neutrons, which are collectively known as nucleons. There is a charge-independent, attractive force that acts between all nucleons, known as the nuclear force. This force has a short range ($\approx 10^{-15}$m [3]) and therefore exhibits saturation: the force from one nucleon affects only those around it. Unlike neutrons which are neutral, protons have a positive charge and so a repulsive Coulomb force acts between them in addition to the nuclear force. The Coulomb force, F_{C} has the form shown in Eqn. 1.1 where q_1 and q_2 are the charges of the two charged particles experiencing the Coulomb force, r is the distance between the particles and ϵ_0 is the permittivity of a vacuum, which has a value of $\approx 8.85 \times 10^{-12}\mathrm{C}^2/\mathrm{Nm}^2$. Whereas the nuclear force has a very limited reach, the Coulomb force has an infinite range and so each proton in the nucleus affects all others. The competition between these forces changes depending on the size of the nucleus and the ratio of protons to neutrons. Competition between the forces acting on the nucleons control the stability of the nucleus.

$$F_{\mathrm{C}} = 4\pi\epsilon_0 \frac{q_1 q_2}{r^2} \tag{1.1}$$

The stability of a nucleus can be described using its binding energy. Using Einstein's mass-energy equivalence, $E = mc^2$, a nuclide of mass $M(Z,N)$, has a certain mass energy $M(Z,N)c^2$, given by Eqn. 1.2 where $m_A c^2$ is the mass energy of the atom, $Zm_e c^2$ is the mass energy of the Z electrons, and $\sum B_i$ is the sum of the atomic binding energy for the electrons.

$$E = M(Z,N)c^2 = m_A c^2 - Zm_e c^2 + \sum_{i=1}^{Z} B_i \tag{1.2}$$

The binding energy $E_B(Z,N)$, of a nucleus with Z protons and N neutrons, is the amount of energy it would take to remove all nucleons from the nucleus. Therefore the binding energy may be determined as the difference in mass energy between a nucleus with mass $M(Z,N)$, and its constituent parts as shown in Eqn. 1.3 where m_n is the mass of a neutron and the proton and electron masses have been grouped into Z neutral hydrogen atoms with mass, m_H, for simplicity.

$$E_B(Z,N) = \left[Zm_H + Nm_n - M(Z,N)\right] c^2 \tag{1.3}$$

1.1.2 Semi-Empirical Mass Formula

The binding energy, $E_B(Z,N)$, may be approximated by considering the effects of the forces at play in the nucleus. One possible method of estimating the binding energy of the nucleus is to use the semi-empirical mass formula [4]. The formula uses a series of theoretically derived terms describing different aspects of the nuclear forces, then matches the observed binding energies of real nuclei using experimentally derived coefficients. As mentioned previously, the short range nuclear force acts between neighbouring nucleons in the nucleus, so for the first stage of this approximation it is assumed that all nucleons have the same number of neighbours and thus the same contribution to the total binding energy. As a consequence of the incompressibility of nuclear matter, the volume, V, of a nucleus containing A nucleons is the sum of the volume, V_0, of those nucleons, which shows that the nuclear volume is proportional to A (see Eqn. 1.4).

$$V = AV_0 \tag{1.4}$$

Therefore the first term in the semi-empirical mass formula, the volume term, assumes that energy gained from the attractive nuclear force increases with A and takes the form shown in Eqn. 1.5, where α_V is the volume energy parameter.

$$E_V(Z,N) \;=\; \alpha_V A \tag{1.5}$$

Assuming the nucleus has a spherical shape, its volume is $V = \frac{4}{3}\pi r^3$ where r is the radius. This can be substituted for the volume of the nucleus in Eqn. 1.4 and rearranged. Then the radius of the nucleus may be written as shown in Eqn. 1.6, where r_0 is given by Eqn. 1.7.

$$r \;=\; r_0\, A^{1/3} \tag{1.6}$$

$$r_0 = \sqrt[3]{\frac{3V_0}{4\pi}} \tag{1.7}$$

Thus the radius of a nucleus can be approximated based on the number of nucleons it contains, A, using Eqn. 1.6 where $r_0 \approx 1.2$ fm.

The assumption that all nucleons feel the same nuclear force is not true for those nucleons at the surface of the nucleus, where the nucleons have fewer neighbours and are therefore less bound. A correction is made to Eqn. 1.5 to account for this; it is known as the surface term (see Eqn. 1.8). Assuming the nucleus is a sphere with a surface area of $4\pi r^2$, then the radius of the sphere, r, may be substituted for Eqn. 1.6 to show the dependence of surface area on A. It is clear that the surface term must scale with $A^{2/3}$.

$$E_S(Z,N) \;=\; -\alpha_S A^{2/3} \tag{1.8}$$

The Coulomb force, which causes a repulsion between the positively charged protons in the nucleus, reduces the binding energy felt between nucleons. The next term in the formula is known as the Coulomb term, shown in Eqn. 1.9 where α_C is the Coulomb energy parameter. Each charged particle is affected by the Coulomb force given by Eqn. 1.9 due to all other charged particles. In a nucleus with Z protons, each is affected by the force from $Z-1$ protons therefore the Coulomb term scales with $Z(Z-1)$. By assuming the nucleus to be a uniformly charged solid sphere the electrostatic self-energy due to the protons may be determined by integrating the electric field due to the protons over all space. This is found to have a dependence of $1/R$ where R is the radius of the charged sphere. Thus the Coulomb term features a factor of $A^{-1/3}$ when R is written in terms of A.

$$E_C(Z,N) \;=\; -\,\alpha_C \frac{Z(Z-1)}{A^{1/3}} \tag{1.9}$$

The symmetry term shown in Eqn. 1.10 may be understood by modelling the nucleons in the nucleus with the Fermi gas model. This model treats the nucleons as weakly interacting, independent particles, moving within the nuclear volume whilst still obeying the Pauli exclusion principle due to their nature as fermions. The binding potential for protons and neutrons may be considered in two separate potential wells, as they are distinguishable particles. Each energy state in the potential well may be occupied by two nucleons with opposite spin projections, and

Table 1.1: Experimentally determined values for parameters needed in the semi-empirical mass formula given in Eqn. 1.11. Values are taken from [3].

Description	Symbol	Value [MeV]
Volume energy parameter	α_V	16 MeV
Surface energy parameter	α_S	17 MeV
Coulomb energy parameter	α_C	0.6 MeV
Symmetry energy parameter	α_{sym}	25 MeV

when the nucleus is in its ground state all states will be filled up to the Fermi energy level. This means the nucleons move freely in the nucleus without collisions as there are no free states to move to. There is a Fermi momentum associated with the Fermi energy, and the number of states up to this momentum may be determined. The number of states allows the total kinetic energy to be found for a nucleus of N neutrons and Z protons. This kinetic energy gives the form of Eqn. 1.10 which is shown to be minimal when $N = Z$ and increases when the asymmetry between the number of protons and neutrons increases, reducing the binding energy. This is dominant for light nuclei, but as the Coulomb force increases with Z^2, the competition between the nuclear force and the Coulomb force at high Z means more neutrons are required to maintain stability, so high mass nuclei are found to be neutron-rich.

$$E_{sym}(Z,N) \, = \, -\,\alpha_{sym}\frac{(N-Z)^2}{A} \tag{1.10}$$

Finally putting all these terms together, the semi-empirical mass formula is completed in Eqn. 1.11 with the inclusion of the pairing term, δ. Nucleons are fermions with an intrinsic spin of 1/2. When the nucleus is in its ground state they arrange themselves in such a way as to minimize the total energy of the nucleus without violating the Pauli exclusion principle. Considering neutrons and protons separately, the exclusion principle indicates that the nucleons must organise themselves into pairs of opposite spin. Therefore the addition of an unpaired nucleon, occupying a new energy level, will cause a greater change in binding energy than the addition of a nucleon which completes a pair.

$$E_B(Z,N) \, = \, \alpha_V A \, - \, \alpha_S A^{2/3} \, - \, \alpha_C\frac{Z(Z-1)}{A^{1/3}} \, - \, \alpha_{sym}\frac{(N-Z)^2}{A} \, + \, \delta \tag{1.11}$$

It has been found experimentally that nuclei with an even number of neutrons and an even number of protons (referred to as even-even nuclei) are more stable than those with one odd amount (resulting in a odd mass number, referred to as odd-even nuclei) and more stable again than those with an odd number of neutrons and odd number of protons (odd-odd nuclei). For this reason the pairing term has three possible values, one for each of these scenarios. The values of the four parameters, (α_V, α_S, α_C, α_{sym}) are dependent on the binding energies used when determining them, a typical set for the first four is given in Table 1.1 and values for the pairing term are given in Table 1.2.

Table 1.2: Experimentally determined values for the pairing term, δ, in the semi-empirical mass formula given in Eqn. 1.11. The value used depends on the number of protons and neutrons in the nucleus where "even-even" describes a nucleus with an even number of protons and an even number of neutrons; "odd-mass" describes a nucleus with either an odd number of protons (and even neutrons) or an odd number of neutrons (and even protons) so that the total mass number is odd; and "odd-odd" describes a nucleus with an odd number of protons and odd number of neutrons. Values are taken from [3].

Even-even nuclei	$\frac{25}{A}$ MeV
Odd-mass nuclei	0
Odd-odd nuclei	$-\frac{25}{A}$ MeV

$$\frac{E_B(Z,N)}{A} = \alpha_V - \alpha_S A^{-1/3} - \alpha_C \frac{Z(Z-1)}{A^{4/3}} - \alpha_{sym} \frac{(N-Z)^2}{A^2} + \frac{\delta}{A} \tag{1.12}$$

It is useful to consider the average binding energy per nucleon described by Eqn. 1.12 when comparing the binding energies of different nuclei. The binding energy per nucleon is shown in Fig. 1.1 for experimentally measured data. Figure 1.1 shows that there is a maximum in average binding energy per nucleon which occurs around $A \simeq 60$, and so there are two ways to increase the binding energy per nucleon in a system. If the nucleus is light, i.e. it contains fewer than 60 nucleons, fusing another light nucleus to it to increase its mass will increase the average binding energy per nucleon and so create a more stable nucleus. Conversely, a nucleus which is more massive than $A \simeq 60$ can only increase its binding energy per nucleon by fission into two or more fragments.

1.1.3 The Fission Process

For those nuclei with A greater than $\simeq 60$, fission into smaller fragments increases the average binding energy per nucleon in a nucleus due to changes in the surface and Coulomb terms in Eqn. 1.12. The surface energy term increases causing the average binding energy per nucleon to decrease as a larger proportion of the total number of nucleons are now at the surface of the nucleus. However, this is overshadowed by the decrease in the Coulomb energy term which arises due to the total number of protons now being split across two nuclei, thereby resulting in a net increase in binding energy per nucleon for the fission fragments. Of the other terms in the semi-empirical mass formula, the volume term (when considering binding per nucleon) is maintained, and changes in the symmetry and pairing terms are less significant [3].

The sequence of increased deformation leading to fission is depicted in Fig. 1.2. The steps leading to the fission of a nucleus begin when a massive nucleus, shown here in a potential energy well, may assume an elongated, deformed shape which can be energetically favourable as it allows two groups of nucleons to form inside the nucleus. They are separated by an initially very small distance, still within the nucleus. If energy can be gained due to a reduction in the Coulomb energy term by stretching the shape of the nucleus and separating the groups of nucleons further,

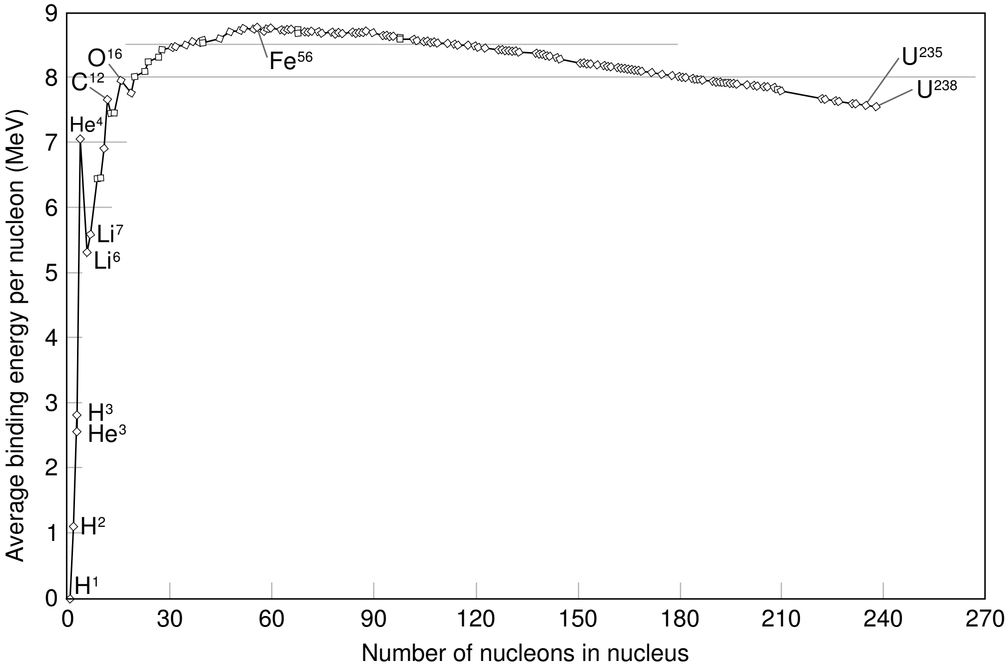

Figure 1.1: The average binding energy per nucleon changes as a function of the number of nucleons in a nucleus. There is a maximum at $A \simeq 60$ so an increase in binding energy per nucleon can be achieved by moving towards that mass of nucleons. Binding energies of nuclei shown in this figure were determined with data from [5] omitting nuclei whose mass has not been measured experimentally and unstable nuclei.

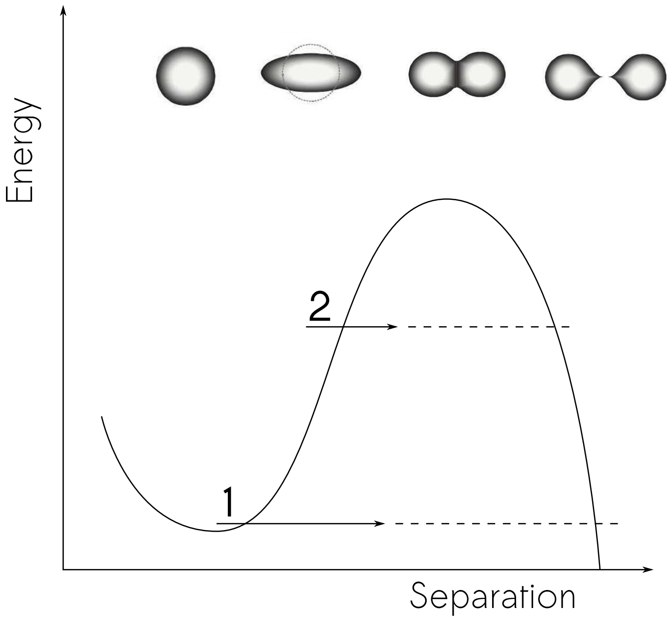

Figure 1.2: The stages of a fissioning nucleus. Assuming an initial spherical starting shape, the diagram shows the nucleus becomes increasingly elongated until full fission into two or more fragments occurs. The barrier width that prevents the fission of a nucleus depends on the excitation energy of the nucleus. The barrier becomes narrower as the nucleus becomes more excited and tunnelling probability increases. Energy 1 corresponds to a nucleus in its ground state and energy 2 corresponds to an excited nucleus.

it will continue to do so until eventually fission occurs [4]. The groups of nucleons, the fission fragments, are now separated by a large distance which lowers the Coulomb energy term thereby increasing the binding energy of the fission fragments.

Fission does not happen instantaneously as it is hindered by the energy barrier called the “fission barrier”, which is a superposition of the binding nuclear force and the repulsive Coulomb force and reflects the energy needed for fragments to escape the short range nuclear force exerted on them in the nucleus. Any bound nucleus does not classically have the energy to overcome this barrier, and in order for fission to occur the fragments must quantum mechanically tunnel through it. The width of the barrier depends on the excitation energy of the nucleus, where a more excited nucleus will have a narrower barrier through which to tunnel. Figure 1.2 illustrates this situation. A nucleus in its ground state will experience the barrier at energy 1 in the figure, whereas a nucleus in an excited state will experience the barrier at energy 2. The tunnelling probability depends on the barrier width and therefore the excitation state of the nucleus.

There are two types of fission; spontaneous and induced. Spontaneous fission occurs without any external influences i.e. the width of the barrier to fission is narrow enough to make it possible for the fragments to tunnel through. In induced fission the nucleus must be stimulated by energy supplied by an external source, for example a neutron capture, into an excited state making fission more probable.

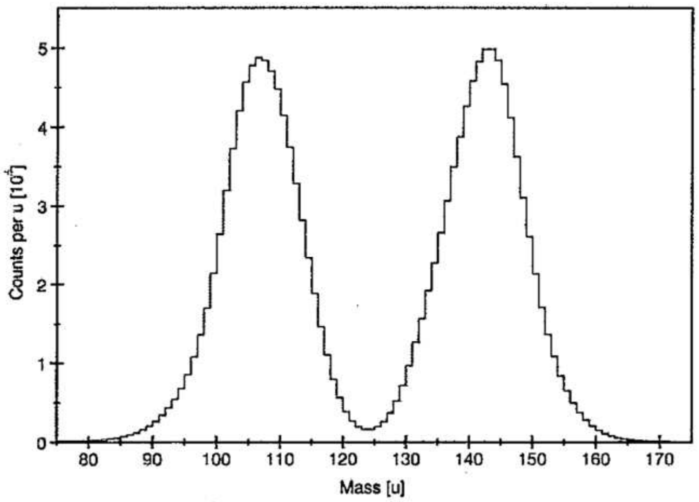

Figure 1.3: The mass distribution of fission fragments from the fission of ^{252}Cf [7]. Reprinted with permission from [7]. Copyright 1995 AIP Publishing LLC.

When fission does occur, the fragments produced are not strictly determined and a number of different products are possible, provided the nucleon number and charge conservation laws are fulfilled. The mass distribution of possible fission fragments from the fission of ^{252}Cf is shown in Fig. 1.3. The bimodal, asymmetric distribution seen in this example stems from the preference of nuclei to contain specific numbers of protons or neutrons which are found to be particularly stable. These "magic numbers" occur at 2, 8, 20, 28, 50, 82 and 126 [6]. The heavy fragment emitted is centred near $^{132}_{50}\mathrm{Sn}_{82}$ which has both a magic number of protons and a magic number of neutrons. When a nucleus has a magic number of neutrons (or protons) it is described as having a full shell of neutrons (or protons). The Shell Model is used to predict the location of these magic numbers.

To determine the energies involved when a heavy nucleus undergoes fission into lighter fragments, the mass difference, Eqn. 1.3, is used. The binding energy change determined using the mass difference is the energy absorbed or released in such a reaction and is known as the Q-value. For example, for a reaction such as neutron induced fission where the addition of a neutron, x, to a heavy nucleus, X, causes X to fission into fragments y and Y (as shown in Eqn. 1.13), the Q-value can be found using Eqn. 1.14. For spontaneous fission where a heavy nucleus X spontaneously fissions to produce fragments y and Y as shown by Eqn. 1.15, the Q-value is determined by Eqn. 1.16.

$$x + X \rightarrow y + Y \tag{1.13}$$

$$Q = [m_x + m_X - m_y - m_Y]\, c^2 \tag{1.14}$$

$$\mathrm{X} \rightarrow \mathrm{y} + \mathrm{Y} \tag{1.15}$$

$$Q = \left[m_{\mathrm{X}} - m_{\mathrm{y}} - m_{\mathrm{Y}}\right] c^2 \tag{1.16}$$

1.1.4 Fission Spectroscopy

There are roughly 7000 isotopes which have been predicted to exist based on the current understanding of the forces involved in allowing nuclei to be bound. Of this 7000, fewer than half have been observed experimentally [6]. Current state-of-the-art nuclear models provide accurate predictions of nuclear properties for many nuclei that lie close to stability. When moving away from stability towards more extremely neutron-rich or proton-rich nuclei these models begin to break down. Therefore data on these unstable nuclei are vital in order for theorists to constrain and test new nuclear models.

Using the semi-empirical mass formula to approximate the forces in the nucleus, it was shown in the previous section that the attractive strong force acting between neighbouring nucleons scales with A, but Coulomb repulsion, which acts between all protons in the nucleus, scales with Z^2. In order for the nucleus to stay bound as it becomes more massive, more neutrons, N, are needed to balance out the repulsion due to the protons. As a consequence, heavy mass nuclei are neutron-rich. When a nucleus undergoes fission, the daughter fragments have a similar N/Z ratio to the parent which means the daughter fragments will be very neutron-rich, exotic isotopes that lie far from stability. Studying fission fragments is therefore a very effective way to examine the nuclear structure of medium mass, exotic, neutron-rich nuclei which are far from stability.

Any nucleus susceptible to fission produces a broad distribution of fission fragments, as was shown for the example of ^{252}Cf in Fig. 1.3. Fission is a highly complex process and no current models can accurately predict the yields of fragments produced [8]. Using TIFFIN to identify these fragments will allow measurements of fission yields to be made. Precise measurements of fission fragment yields as well as the decay information of those fragments gives valuable insight into both nuclear structure and the fission process.

Fragment-γ Coincidence Measurements

A portion of the Q-value from fission can manifest as excitations of either fragment nucleus above its ground state. The excited states of the fragments are typically short-lived and the energy is dissipated via the emission of γ-rays within 1 ns of fission [9]. This is within the time it takes a fission fragment to be detected by the TIFFIN detector, thereby allowing the γ-rays to be detected in coincidence with the fission event. By using TIFFIN in conjunction with γ-ray detection and a suitable data acquisition system, it is possible to study these fragment-γ coincidence measurements.

Each fission fragment produced may be in a different excited state. The γ-rays emitted depend on the state populated and there may be multiple γ-rays which can be emitted from a certain state. The relative probability of each decay occurring is described by its branching ratio. Measuring the energies and branching ratios of the γ-rays emitted gives valuable information about the structure of nuclei which may not have been studied in detail before. For example the excited states of ^{139}Te, which was produced from the spontaneous fission of ^{248}Cm, were first observed in 2000 [10]. More recently, the excited states of ^{87}Se, also produced from the fission of ^{248}Cm, were observed for the first time in 2013 [11]. However, without accurate identification of the fragment nucleus, the decay information gained from the γ-ray spectroscopy of isotopes created via fission has been attributed to the wrong nucleus numerous times. For example the excitation scheme first attributed to ^{147}Pr in 2000 [12] was later assigned to ^{144}La in 2009 [13] and ^{151}Pr was first assigned a level scheme in 2000 that had initially been assigned to ^{149}Pr in 1998 [12] [14]. TIFFIN will allow for the proper identification of γ-rays emitted from the detected fragments.

1.2 Alpha Decay

1.2.1 Energy Balance in Alpha Decay

The emission of an α-particle can be represented by the process given in Eqn. 1.17 where A is the number of nucleons in the nucleus, Z is the number of protons and N is the number of neutrons. An α-particle is a helium nucleus; it contains two protons and two neutrons.

$$ {}^{A}_{Z}\mathrm{X}_{N} \rightarrow {}^{A-4}_{Z-2}\mathrm{Y}_{N-2} + \alpha + Q \tag{1.17}$$

Alpha decay is particularly favoured in heavy nuclei with A>150. In light nuclei the amount of energy needed to separate an α-particle from the nucleus is comparable to the energy needed for nucleon emission, whereas at higher mass numbers, the energy for α-decay becomes much less than that for nucleon emission. This is shown in Fig. 1.4.

The Q-value is the net energy released in the decay of the nucleus, as outlined in Sec. 1.1.3. For α-decay specifically, Q_α is found with Eqn. 1.18. The Q-value can be calculated in this way for the emission of various light ions. For heavy nuclei which are not at the limits of nuclear existence, the emission of an α-particle often leads to a positive Q-value, making it stand out against the emission of other light ions. This is shown for the example of ^{241}Am (which was used in this work) in Table 1.3 and is the phenomenon which leads to the trend seen in Fig. 1.4.

$$Q_\alpha = [m_\mathrm{X} - m_\mathrm{Y} - m_\alpha]\, c^2 \tag{1.18}$$

Due to the particular stability of having two protons and two neutrons together, it is not unreasonable to consider an α-particle behaving as though it were pre-formed within a large parent nucleus. The α-particle may be thought of as moving within a potential well, the height

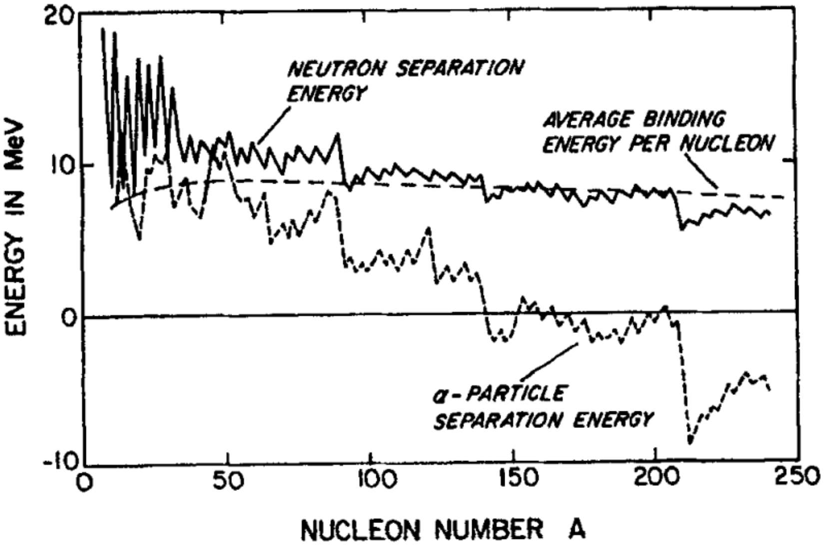

Figure 1.4: The calculated energy required to separate a neutron or an α-particle from a stable nucleus, compared to the average binding energy per nucleon, is plotted as a function of nucleon number. Reproduced with permission [3].

Table 1.3: The calculated Q-value (energy release) for various modes of decay of ^{241}Am. Masses for calculations taken from [15].

Emitted Particle	Energy Release [MeV/c^2]	Emitted Particle	Energy Release [MeV/c^2]
n	-6.647	^{4}He	+5.638
^{1}H	-4.480	^{5}He	-1.675
^{2}H	-8.790	^{6}He	-5.676
^{3}H	-8.179	^{6}Li	-2.071
^{3}He	-9.452	^{7}Li	-0.118

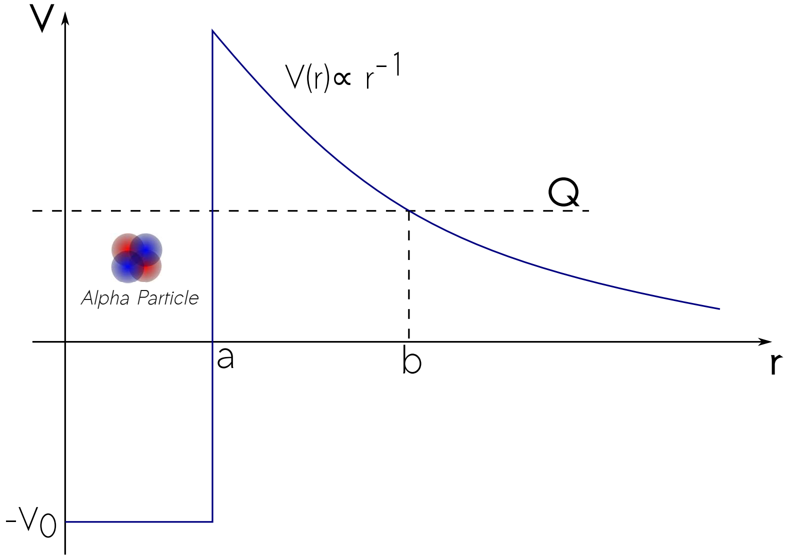

Figure 1.5: The relative potential energy, V, of an α-particle and daughter nucleus system as a function of their separation, r. The nuclear surface is at $r = a$. Beyond this point only the Coulomb repulsion operates between the α-particle and the daughter nucleus at $r > a$. The α-particle must tunnel from a to b to be emitted from the nucleus.

of which is dependant on the Coulomb repulsion from the daughter nucleus. The width of the well is assumed to be the radius of the parent nucleus which has a mass A. The radius, r, was approximated by Eqn. 1.6.

The potential well as described here is depicted in Fig. 1.5. The α-particle is bound inside the nucleus when $r < a$. Classically, the α-particle should have more energy than the height of the potential well in order to be emitted. Experimentally, the energy of emitted α-particles is found to be much less than the energy expected from this classical approximation. As was the case for fission, the emission of an α-particle depends on its probability of tunnelling through the potential barrier.

It has been found that the energy of emitted α-particles, which is determined by the Q-value of the reaction, shows limited variation, whereas there is a huge variation in the α-decay half-lives observed. Futhermore, a large Q_α-value specifically corresponds to a short half life and a small Q_α-value corresponds to a long half life. This relationship between half-life and Q_α is called the Geiger-Nuttall Law and is shown in Fig. 1.6.

The general features of Fig. 1.6 were explained in 1928 simultaneously by Gamow as well as by Gurney and Condon. Their explanation was based on the quantum mechanical tunneling of a pre-formed α-particle inside the parent nucleus as outlined above [17]. The barrier to decay accounts for the fact that a nucleus, which is unstable to α decay, does not decay immediately and that there is a wide variation in half-life for only a narrow variation of Q-values. Each time the α-particle approaches the barrier there is some probability it may tunnel through. The decay constant, λ, is inversely proportional to the half-life. In this theory, the decay constant for an

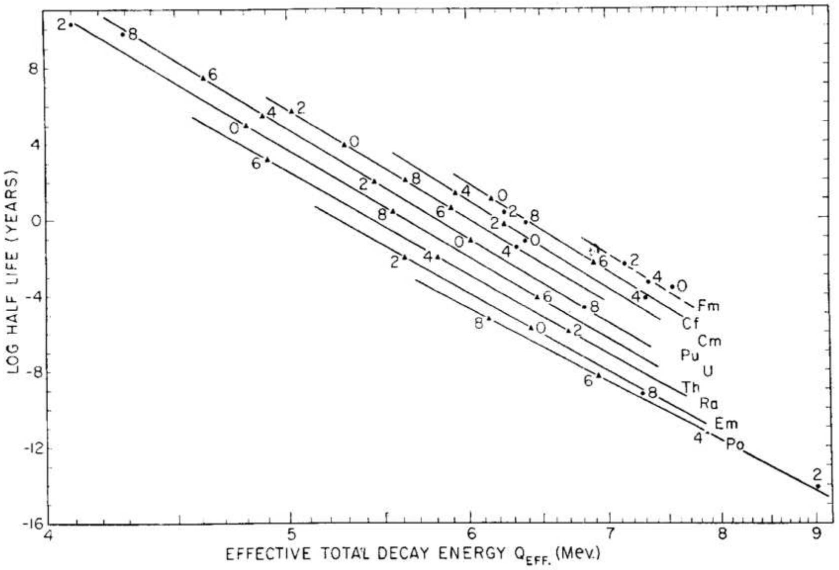

Figure 1.6: The relationship between the Q_α-value and the α-decay half life which is referred to as the Geiger-Nuttall Law. The last digit in the mass number for the α emitter is given beside each point [16]. Only even-even nuclei are included in this plot. Reprinted from [16] with permission from Elsevier.

α emitter is given by Eqn. 1.19 where f is the frequency at which the α-particle approaches the potential barrier and P is the probability of tunnelling through [4].

$$\lambda = fP \tag{1.19}$$

This theory is able to explain the trends of the Geiger-Nuttall Law, (Fig. 1.6) but it does not accurately predict the magnitudes of the lifetimes observed. The hindrance factor, HF, is the factor by which an α decay rate is slower than would be expected from calculations. In practice it is calculated as the ratio between the calculated and measured decay constants, λ_{cal} and λ_{exp}, or the ratio between the experimental half-life, $t_{1/2}^{\text{exp}}$, and theoretical half-life, $t_{1/2}^{\text{cal}}$, as shown in Eqn. 1.20.

$$HF = \frac{\lambda_{\text{cal}}}{\lambda_{\text{exp}}} = \frac{t_{1/2}^{\text{exp}}}{t_{1/2}^{\text{cal}}} \tag{1.20}$$

1.2.2 Alpha Spectroscopy

Many heavy nuclei decay via α-decay into exotic, neutron-rich isotopes, which are of interest to the nuclear science community. These nuclei often emit multiple α-particles each at a different, but distinct, energy. For example, ^{241}Am emits α-particles at 25 different energies [18]. Each one represents a transition to a different excited state of the daughter nucleus. By detecting the energy of the α-particle the Q-value of the reaction may be deduced by Eqn. 1.21 where

T_α is the energy of the detected α-particle, Q_α is the net energy released due to the α decay, as outlined previously in Sec. 1.2, m_α is the mass of an α-particle and m_{Y} is the mass of the daughter nucleus produced after α decay.

$$Q_\alpha = T_\alpha \left(1 + m_\alpha / m_{\mathrm{Y}}\right) \tag{1.21}$$

Populating different excited states through α decay allows the examination of nuclear structure by measuring hindrance factors, decay rates and branching ratios [17].

α-γ Coincidence Measurements

As mentioned in the previous section, nuclei that α decay often emit multiple α-particles at different energies - each representing the transition to a particular state of the daughter nucleus. If the state populated in the daughter is an excited state, it will then emit γ-rays in order to reach its ground state. This is illustrated in Fig. 1.7 which shows the three levels with the largest branching ratios for the α decay of ^{241}Am to ^{237}Np, and the ground state of ^{237}Np for reference. The subsequent γ decays from those levels are also shown. 84.8% of the time ^{241}Am decays via a 5485.56 keV α-particle to an excited state in ^{237}Np which may then decay via γ-ray emission to the ground state. In a similar fashion to the fragment-γ coincidence measurements, TIFFIN can be used to take α-γ coincidence measurements by coupling it with γ-ray detection apparatus. Studying the angular correlations and angular distributions of the γ emissions provides a means of determining the angular momentum transfer involved in the decay [19], and measuring the energies of the decays allows the energy levels to be found. These measurements are of interest to the nuclear science community for tracking evolution of single particle level energies and testing nuclear models as well as checking decay schemes to improve upon energy and branching ratio measurements [20].

1.3 Current Experimental Infrastructure at SFU

The combination of facilities in production at Simon Fraser University means that it will be possible to conduct in-house experiments on exotic, neutron-rich nuclei. One advantage of doing in-house experiments rather than accelerator facility based experiments is that there are fewer time constraints on the experiment, allowing long periods of data collection which will be particularly beneficial for observing weak transitions or measuring sources with low activity.

1.3.1 Gamma-Ray Detection

The 8π γ-ray spectrometer array shown in Fig. 1.8 consists of 20 Compton suppressed high purity germanium (HPGe) detectors, each with $\sim 23\%$ relative efficiency [2] and the entire array is about 1% efficient at 1.3 MeV. A typical energy resolution is between 1.8 - 2.2 keV at 1.3 MeV

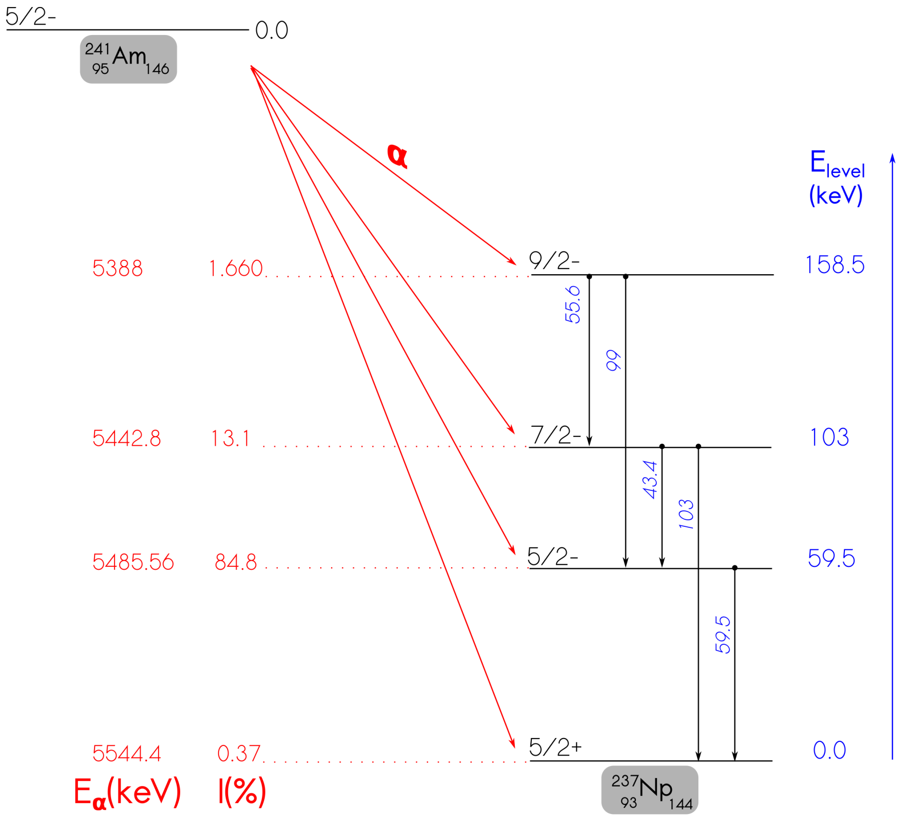

Figure 1.7: Decay scheme showing selected decays from ^{241}Am which was used for this work. Red arrows from ^{241}Am show α decays to various excited states of ^{237}Np which then γ decays (represented by the vertical, black arrows) to the ground state. Data from [18].

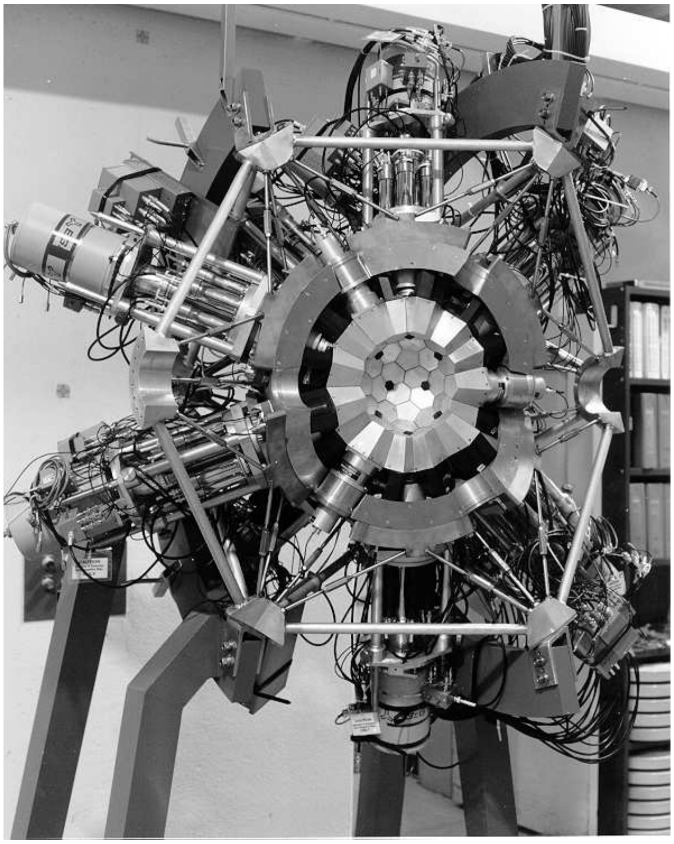

Figure 1.8: Photograph of one hemisphere of the 8π gamma-ray spectrometer which has recently been relocated to Simon Fraser University Chemistry Department. There are 10 HPGe per hemisphere, each surrounded by Bismuth Germanate (BGO) Compton suppression shields [2]. The currently vacant inner volume has a diameter of 19.8 cm and will house the TIFFIN detector upon its completion.

[21]. The array has recently been relocated to the laboratory at Simon Fraser University for use by the nuclear science groups.

Germanium detectors are used to detect γ-rays and using an array allows the source of radiation to be surrounded by detectors, ensuring a high efficiency for γ-ray detection. As outlined in Sec. 1.1.4, after fission occurs the decay fragments emit γ-rays which, when detected in coincidence with the fragments, allow the examination of the nuclear structure of the isotope detected. By placing a spontaneous fission source inside TIFFIN and installing it at the center of the 8π array, fission fragments and their decays may be observed.

1.3.2 Neutron Generator

The Subcritical Intense Multiplier Of Neutrons (SIMON) is a proposed neutron generator facility to be located in a vault below the Nuclear Science lab. SIMON will use the Thermo Scientific P 385 Neutron Generator [22] with a moderator which will allow the generation of neutrons at a variety of energies. SIMON will produce neutrons which will be used to bombard targets containing material that fissions after capturing a neutron, such as ^{235}U. TIFFIN can be installed in the neutron vault with such material inside the detector, allowing fission fragments to be observed when fission is induced and the distribution of fission fragments to be measured.

Chapter 2

Ionization Chamber Theory

2.1 Interactions of Heavy Charged Particles in a Gas

As charged particles move through a material they transfer their kinetic energy to the matter until they lose all their energy and come to rest. The distance travelled by a charged particle in a material is known as its range. The range depends on the type and probability of reactions allowed to a certain species of radiation as well as the amount of kinetic energy the particle possess upon entering the medium. These characteristics also determine how the radiation may be detected. In general, the passage of all charged radiation through matter is governed primarily by two electromagnetic processes:

1. inelastic collisions with atoms where energy is transferred to the atomic electrons,
2. elastic collisions with nuclei.

The probability of an interaction occurring between two particles depends on the density of possible scattering targets and also on the nature of the interaction. An individual interaction probability may be conveniently described by the cross section of that interaction, σ which is defined in Eqn. 2.1 where $d\Xi$ is the probability of undergoing an interaction of a certain type, in a thin section of material, dx, that contains a number density of scattering targets N_V [23]. A large cross section therefore corresponds to a greater likelihood of the interaction taking place.

$$d\Xi = dx N_V \sigma \tag{2.1}$$

For heavy charged particles the cross section for inelastic collisions with atoms, where energy is transferred to the atomic electrons, is such that almost all of a charged particle's energy is lost in this way as it passes through matter. As the incident charged particle radiation interacts with the atomic electrons the Coulomb interaction between them causes energy to be transferred from the kinetic energy of the particle to the atomic electrons. Each collision transfers only a small fraction of the total kinetic energy of the particle but the collisions happen so frequently

Table 2.1: Values for the energy needed to create one ion pair in a selection of gases [24].

Gas Species	1st Ionization Potential (eV)	W-value (eV/ion pair)
Ar	15.7	26.3
CH_4	14.5	29.1
Air		35.1
He	24.5	42.7
H_2	15.6	36.4
N_2	15.5	36.4
O_2	12.5	32.2
C_4H_{10}	10.8	23.0

the particle soon transfers all its energy to the medium and comes to a stop. The amount of energy transferred to the atomic electron in a single collision is usually enough to cause it to be liberated from the atom, leaving the atom ionized. The detection of radiation in an ionization chamber relies on the collection of this free charge produced through ionization.

2.1.1 Ion Pair Formation

The first ionization potential is the energy required to liberate the least bound electron from a previously neutral atom, resulting in a free electron and an ion which are collectively known as an ion pair. The magnitude of the first ionization potential is a property of the gas type. Some common gases used in ionization chambers are listed in Table 2.1. However, not all interactions with the incident radiation result in ionization and so the empirically determined W-value is more often used for realistic calculations of ion pair formation. The W-value is a measure of the average energy needed for an ion pair to be created and is dependent on the type of incident radiation (i.e. the W-value for a gas being ionized by α-particles is different to the W-value for that same gas being ionized by fast electrons due to the different interaction cross sections for the different particles, in part due to their different charges).

Gases chosen for ionization chambers have low W-values to ensure many ion pairs are created per unit energy, which improves the response of the detector by reducing the statistical limit to the energy resolution achievable by the detector. This will be explained further in Sec. 2.4.

2.1.2 Stopping Power

The rate at which the incident radiation deposits its energy in the gas is described by the stopping power, S, Eqn. 2.2. It is more formally known as the specific energy loss.

$$S = -\frac{dE}{dx} \tag{2.2}$$

This specific energy loss is described by the Bethe formula given in Eqn. 2.3 where the factors depending on the material and incident particle are as follows: W is the mean excitation energy which is determined experimentally; z and v are the charge and velocity of the incident particle;

and, N_V and Z are the number density and atomic number of the atoms in the absorber material. The constants are m_e, the rest mass of an electron; e, the electronic charge; and ϵ_0, the electric permittivity of free space.

$$-\frac{dE}{dx} = \frac{1}{4\pi m_e}\left(\frac{e^2 z}{\epsilon_0 v}\right)^2 N_V Z\left[\ln\frac{2m_e v^2}{W} - \ln\left(1-\frac{v^2}{c^2}\right) - \frac{v^2}{c^2}\right] \qquad (2.3)$$

This formula shows that the behaviour of the rate of energy loss is dependent principally on the multiplicative factor, $(\frac{e^2 z}{v})^2$ as the rest varies very slowly with energy. It shows that as the particle velocity decreases, the rate of energy loss increases, and it also shows that as the charge on the particle increases the rate of energy loss increases. This means that a more heavily charged particle will lose its energy faster than a particle carrying less charge even if they have the same initial energy. It also means that a particle will lose more energy the slower it travels because of the $1/v^2$ factor. The formula breaks down when the particle is travelling very slowly, as charge transfer becomes much more probable.

2.1.3 Energy Loss Characteristics - The Bragg Curve

A plot of the rate of energy loss or stopping power against the distance travelled in a medium is know as a *Bragg curve*, shown in Fig. 2.1 (a).

As explained in the previous paragraph, the rate of energy loss is heavily dependent on the nuclear charge and energy (which dictates the velocity) of the incident radiation. These dependencies are reflected in the Bragg curve. For example, the larger the nuclear charge of a particle the sooner the Bragg curve will peak, as the rate of energy deposition increases with z^2. Figure 2.1 (b) illustrates the case for three particles of different z. If these particles all had the same energy then the integrated areas would be equal. For particles with the same nuclear charge but different energies, the curve will reach the same maximum value for energy loss but the shape is truncated for those with less energy. This situation is shown in Fig. 2.1 (c).

In order to utilise this information, not only the total energy deposited in the detector but also the distribution of its deposition must be recorded. If the detector is sensitive to this distribution of charge then it is possible to reproduce the Bragg curve and identify the species.

2.1.4 Range

As mentioned previously, the distance a particle travels in a gas before depositing all its energy is known as its range. In order to measure the full energy of the radiation the range of the particle must be fully encompassed by the detector. The rate of energy loss (Eqn. 2.3) and therefore also the range, is dependent on the material absorbing the energy via its number density, N_V, and atomic number of the absorber nuclei, Z. For a given choice of gas it is therefore possible to ensure the particles stop in the detector by adjusting the pressure, which is proportional to number density.

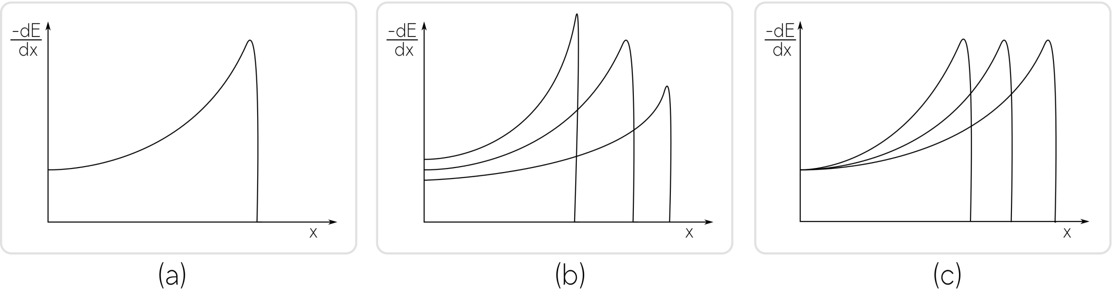

Figure 2.1: (a) The plot of the specific energy loss along the track of a charged particle is known as a Bragg curve. (b) The rate of energy loss increases as the charge (z) on the particle increases. From the left to the right of the plot, the Bragg curves represent the energy loss of particles with higher to lower z. If the particles have the same kinetic energy, the area under these curves would be the same. (c) Particles with the same z but different kinetic energy will produce Bragg curves of the same height but different area where the curve with the greatest area corresponds to the particle with the most energy.

2.2 The Ionization Chamber

Putting together the concepts outlined in Sec. 2.1, a basic understanding of how an ionization chamber works can be outlined. The simplest configuration of an ionization chamber is a container filled with a suitable gas, which can be used to detect charged radiation. When the radiation enters the chamber it interacts with the gas causing the gas to ionize and produce electron-ion pairs. There are two electrodes inside the chamber; when bias is applied, the electric field between them encourages the separation of the electron-ion pairs that have been formed by the radiation. The movement and collection of electrons on the plates form a signal. The size of this signal is dependent on the number of electrons formed in the chamber. Therefore the size of the signal is dependent on the energy of the radiation detected. A simple, general design of an ionization chamber is shown in Fig. 2.2. The negative electrons are attracted to the anode and the positive ions to the cathode. The next stage is to garner an understanding of how the signal is formed by discussing charge collection concepts in Sec. 2.3.

2.3 Charge Collection

2.3.1 Drift Velocity of Electrons

In the absence of an applied field, electrons and ions move with energies distributed according to the Maxwell-Boltzmann energy distribution, where the most probable energy is $\frac{3}{2}k_BT$ corresponding to a most probable thermal velocity: Eqn. 2.4 where m is the mass of the particle, k_B is Boltzmann's constant and T is temperature.

$$v_t = \sqrt{\frac{3k_BT}{m}} \tag{2.4}$$

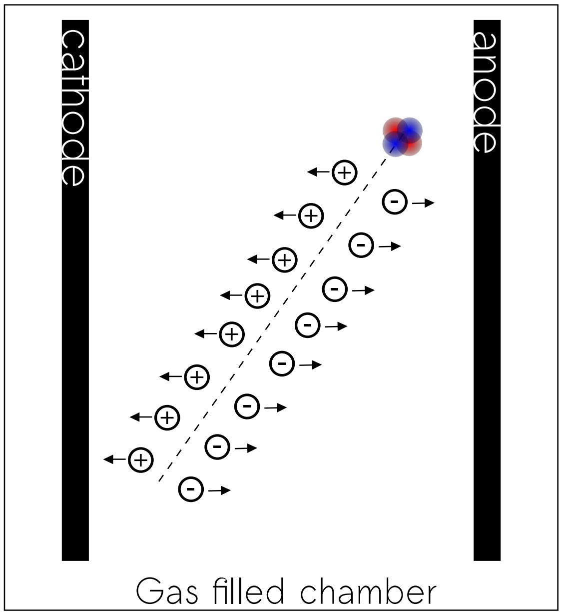

Figure 2.2: An α-particle is detected in a simple representation of an ionization chamber.

Charged particles in the detector are accelerated with the application of an electric field, ϵ. The magnitude of this acceleration can be estimated with Eqn. 2.5 where e is the electronic charge, ϵ is the electric field applied and m is the mass of the particle being accelerated.

$$a = e\frac{\epsilon}{m} \tag{2.5}$$

The mean free path of a particle, λ, is the distance it can travel before colliding with another particle. Therefore, the average time between collisions, τ, is λ over the thermal velocity of the particles, v_t, Eqn. 2.6.

$$\tau = \frac{\lambda}{v_t} \tag{2.6}$$

The resulting drift velocity in the direction of the field is therefore Eqn. 2.7. Kinetic theory assumes that the particle stops after each collision and is then accelerated again from the initial speed of 0 to the final speed of $a\tau$: the average of $a\tau/2$ for the motion at constant acceleration in such conditions is used in Eqn. 2.7 as the magnitude of the drift velocity. Substituting for acceleration and average time between collisions (from Eqn. 2.5 and 2.6) gives Eqn. 2.8 and finally substituting for thermal velocity gives Eqn. 2.9 for the drift velocity of electrons in terms of the electric field and the mean free path.

$$\begin{aligned}\nu_d &= \frac{a\tau}{2} && (2.7)\\ &= e\frac{\epsilon}{m}\frac{\lambda}{2v_t} && (2.8)\\ &= \frac{e\epsilon\lambda}{\sqrt{12k_BTm}} && (2.9)\end{aligned}$$

Mean free path is inversely proportional to the collision cross section, σ, and the number density of the gas, N$_V$. Using the ideal gas formula as shown in 2.10 and then substituting $n = N_V V/N_A$ and $R = k_B N_A$, the formula can be rearranged to $P = N_V k_B T$.

$$\begin{aligned}PV &= nRT\\ \frac{P}{RT} &= \frac{n}{V} && (2.10)\end{aligned}$$

Thus λ may take the form shown in Eqn. 2.11. Therefore the drift velocity for electrons in an electric field is dependent on the strength of that electric field, the pressure of the gas and the cross section for interaction in the gas.

$$\lambda = \frac{1}{N_V\sigma} = \frac{k_BT}{P\sigma} \qquad (2.11)$$

A commonly used gas in ionization chambers is argon; the drift velocity in argon is shown in Fig. 2.3. This figure shows that the addition of methane to argon increases the maximum drift velocity achievable in the gas, this is due to its lower interaction cross section. Calculated drift velocity data for P10, the mixture of methane and argon used for this work, is shown in Fig. 2.4 as a function of ϵ/P.

Electrons travelling through the gas may scatter from atomic electrons via Rutherford scattering due to the Coulomb repulsion between them. The Rutherford cross section is expected to decrease with increasing energy of the incident particle. However, this is not found to be the case for very low energies ($\approx$ 1 eV). Ramsauer and Townsend independently observed that at low electron energies, such as those of electrons in ionization chambers, σ increases with increasing energy due to the wave-like properties of the electron [28]. When the electron scatters there is a phase shift of its wave function, and at a particular electron velocity this phase shift results in destructive interference of the scattered contributions. The resulting minimum in the cross section as a function of energy is known as the Ramsauer dip, and it corresponds to the peak drift velocity seen in Fig. 2.3, as the electrons can traverse the gas nearly unhindered.

2.3.2 Regions of Operation

Without external influence, the ion pairs created in the gas would recombine to form neutral atoms and the detector will not produce a signal. An electric field is applied in order to minimise

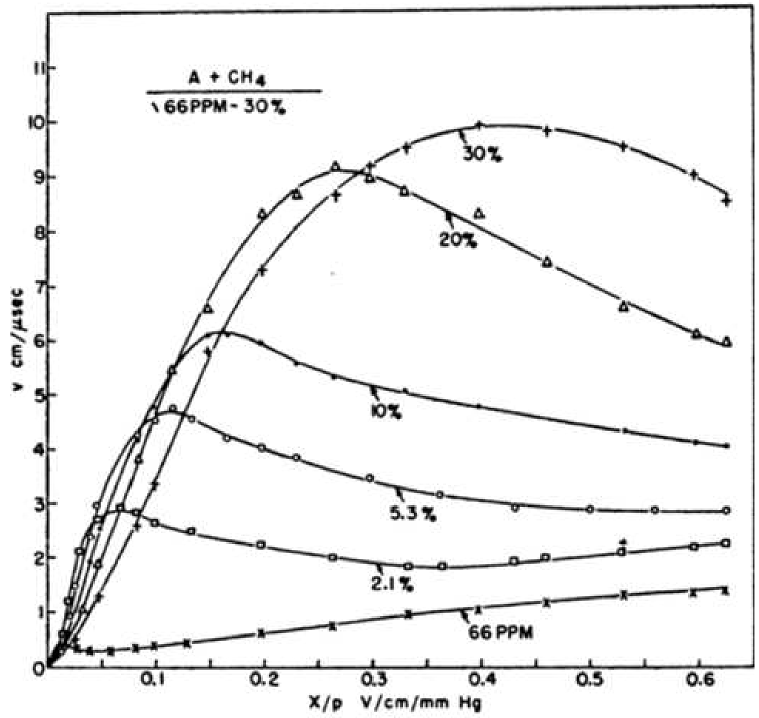

Figure 2.3: The relationship between drift velocity of electrons and ϵ/P (given here as X/P) for methane and argon gas mixtures which vary between 66 ppm methane to 30% methane [25]. ©2008 Canadian Science Publishing. Reproduced with permission.

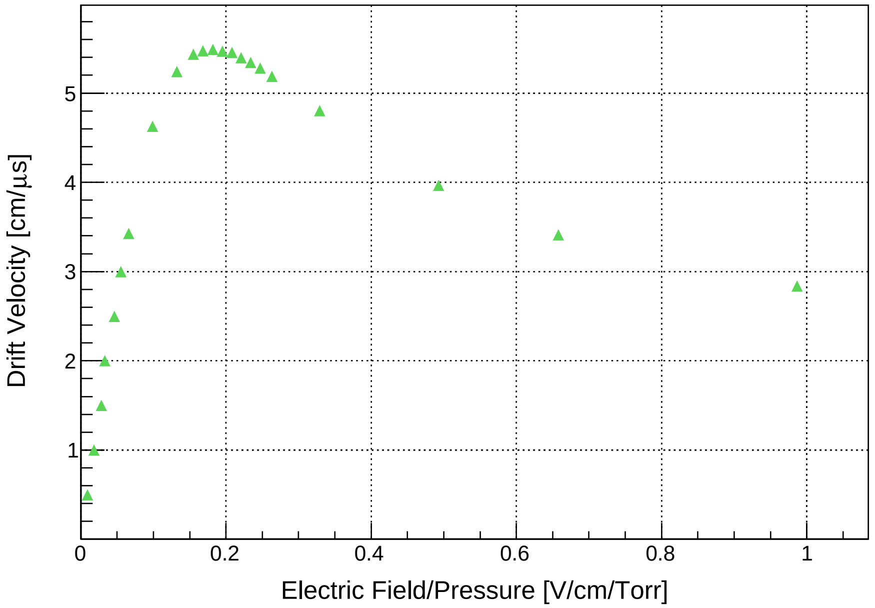

Figure 2.4: The calculated relationship of drift velocity with changing ϵ/P for P10 at room temperature. Plotted using data from [26] [27].

electron loss due to recombination. The behaviour of a gas detector under a range of applied electric fields is illustrated in Fig. 2.5a.

A small amount of applied bias will create a weak field encouraging some electrons to be collected. As the applied bias increases, full electron collection is assured and the detector enters the region of operation known as the "Ionization Chamber Region". As the electric field between the plates increases in strength, free electrons in the detector are lent greater amounts of kinetic energy by the field thereby increasing their drift velocity. These electrons collide with molecules in the gas and have such energy that they cause further ionization to occur, leading to more free charge to be produced, a phenomenon referred to as gas multiplication. This stage is known as the "Proportional Region" of operation because the signal size produced by the detector is proportional to the energy of the incident radiation and continues linearly with applied bias until the "Region of Limited Proportionality" is reached. The dense concentration of positive ions produced is sufficient to alter the field in the detector, resulting in limited proportionality at large electric field strengths. Finally, when the applied field is high enough, the resulting avalanche from the gas multiplication will cause total breakdown of any proportionality, so that the signal is the same regardless of the energy of the incident radiation. This is named the Geiger-Müller Region. Data was taken over a range of applied bias for this work, as shown in Fig. 2.5b, and the pulse height was found to be consistent across all data sets, indicating operation in the ionization chamber region. Operating the detector in the proportional region or higher was not possible due to the bias supply used, which could not provide a potential greater than 4000 V.

2.3.3 Signal Generation

An ionization chamber may be represented by an equivalent circuit in order to better understand the flow of charge and signal generation. Such an equivalent circuit for a simple ionization chamber is drawn in Fig. 2.6. An electric field, ϵ, exists between the two plates of the chamber due to the potential difference caused by the power source, V_0. The capacitance between the plates of the detector is represented by C and a signal is read out from the detector by measuring the potential difference across R, V_R.

When there is nothing in the chamber to be detected, a state of static equilibrium exists and there is no movement of charge: $V_R = 0$. A heavy charged particle may enter the chamber and deposit all its energy in the gas resulting in the creation of free charge between the detector plates as shown in Fig. 2.6. For simplicity, we consider an event where the trajectory of the track of the radiation is parallel to the detector plates. The introduction of moving charge between the detector plates removes the state of equilibrium and a potential difference, V_R is seen across the load resistor, R. The magnitude of this potential difference is equal to the potential drop across the chamber caused by the movement of ions and electrons in the chamber. V_R may be determined using arguments based on the conservation of energy. The energy required to move this charge comes from the energy stored in the capacitor, $\frac{1}{2}CV_0^2$. The energy required for this movement is $Q\Delta\phi$ where Q is the charge of the particle being moved and $\Delta\phi$ is the potential difference it was moved through. The resulting potential difference across the chamber due to the presence of the ion pairs is V_{ch} and the remaining energy stored by the capacitor can be determined using V_{ch}. The relationship between theses quantities is shown in Eqn. 2.12.

$$\begin{aligned}\text{Original Stored Energy} &= \text{Ions} + \text{Electrons} + \text{Leftover Stored Energy}\\ \frac{1}{2}CV_0^2 &= Q\Delta\phi_+ + Q\Delta\phi_- + \frac{1}{2}CV_{\text{ch}}^2 \qquad (2.12)\end{aligned}$$

The distance travelled in the electric field is $\nu_+ t$ for ions and $\nu_- t$ for electrons, where ν_+ and ν_- are the corresponding drift velocities, and t is the time they have spent travelling. The amount of charge in the detector, Q is equal to the number of ion pairs created, n_0, multiplied by the electronic charge, e. Thus the amount of energy absorbed by the ions and electrons to move them in the detector may be determined in terms of the electric field, as shown in Eqn. 2.13.

$$\frac{1}{2}CV_0^2 = n_0 e\epsilon\nu_+ t + n_0 e\epsilon\nu_- t + \frac{1}{2}CV_{\text{ch}}^2 \qquad (2.13)$$

Equation 2.13 can be rearranged, collecting the remaining energy with the stored energy on the left-hand side as shown in Eqn. 2.14. Then, recalling that the electric field in a capacitor is equal to the V/d where V is the potential difference across the plates and d is the separation between the plates, the relationship can be written as shown in Eqn. 2.15.

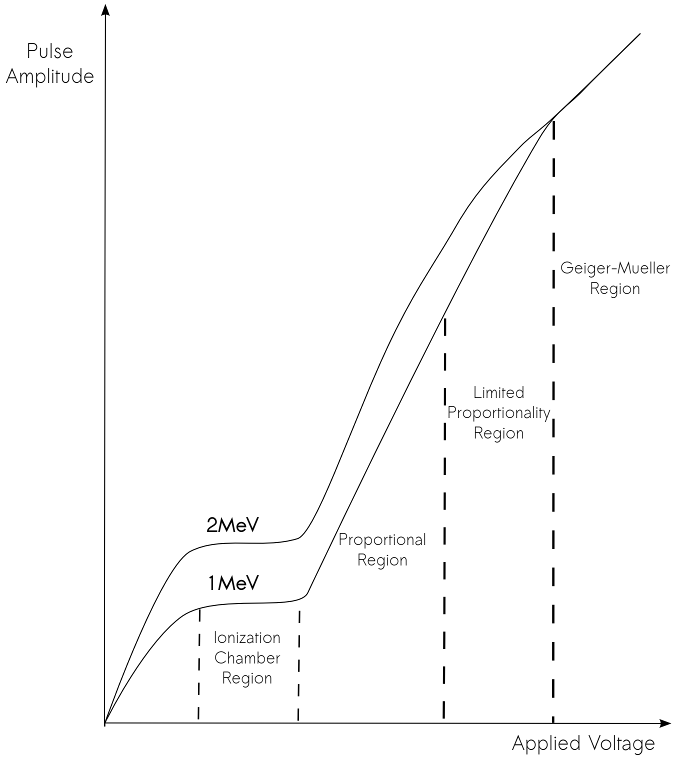

(a)

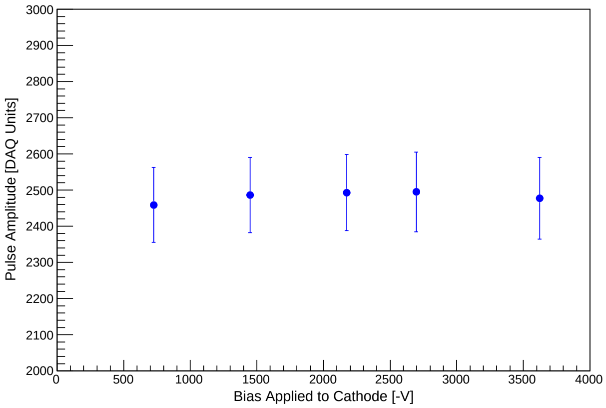

(b)

Figure 2.5: Depending on the bias applied, gas detectors exhibit different regions of operation. This is demonstrated by plotting the bias applied against the observed pulse amplitude. Figure (a) is an illustration of this for events depositing two different amounts of energy in the gas (taken from [24]). Figure (b) shows data from this work which does not appear to extend beyond the ionization chamber region.

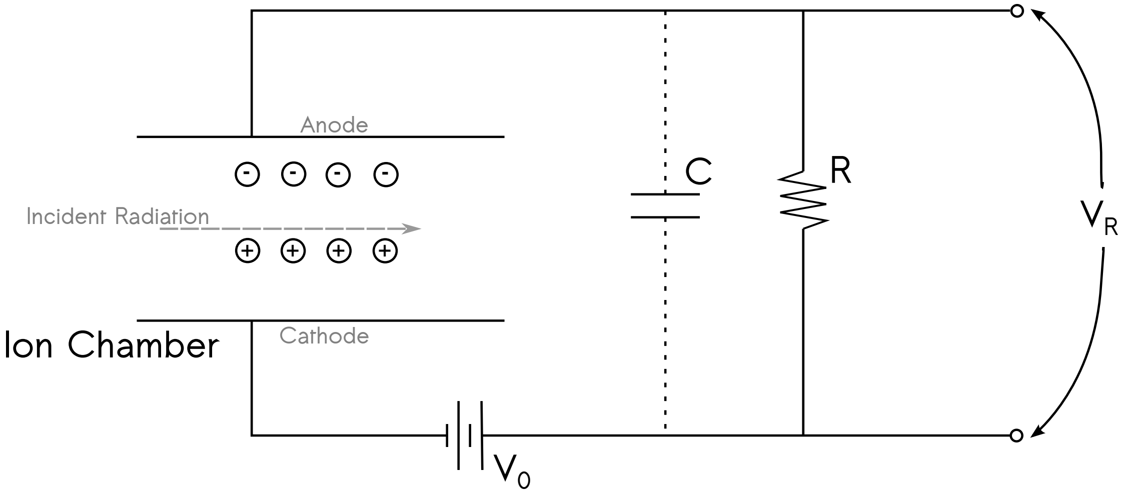

Figure 2.6: Equivalent circuit drawn for an ionization chamber where the radiation enters parallel to the electrodes.

$$\frac{1}{2}C(V_0^2 - V_{\rm ch}^2) = n_0 e \varepsilon(\nu_+ + \nu_-)t \tag{2.14}$$

$$\frac{1}{2}C(V_0 + V_{\rm ch})(V_0 - V_{\rm ch}) = n_0 e \frac{V_{\rm ch}}{d}(\nu_+ + \nu_-)t \tag{2.15}$$

The signal across the load resistor is V_0 - $V_{\rm ch}$ = V_R, but as the potential difference across the chamber is significantly larger than the change due to the ions it is possible to make the assumptions given in Eqn. 2.16. Taking these assumptions into account, then Eqn. 2.15 can be rearranged to give the magnitude of the signal, V_R, shown in Eqn. 2.17.

$$\begin{aligned} V_R &\ll V_0 \\ V_0 + V_{\rm ch} &\cong 2V_0 \\ \frac{V_0}{d} &\cong \frac{V_{\rm ch}}{d} \end{aligned} \tag{2.16}$$

$$V_R = \frac{n_0 e}{Cd}(\nu_+ + \nu_-)t \tag{2.17}$$

A maximum change in potential difference occurs when all the ion pairs have been collected, as shown in Eqn. 2.18.

$$V_{\rm max} = \frac{n_0 e}{C} \tag{2.18}$$

Frisch Grids

The time taken for all electrons to collect is ≈ 1 μs, and in some cases faster but the time for ions to collect is on the order of ≈ 1 ms. This makes the response of the detector very slow. If

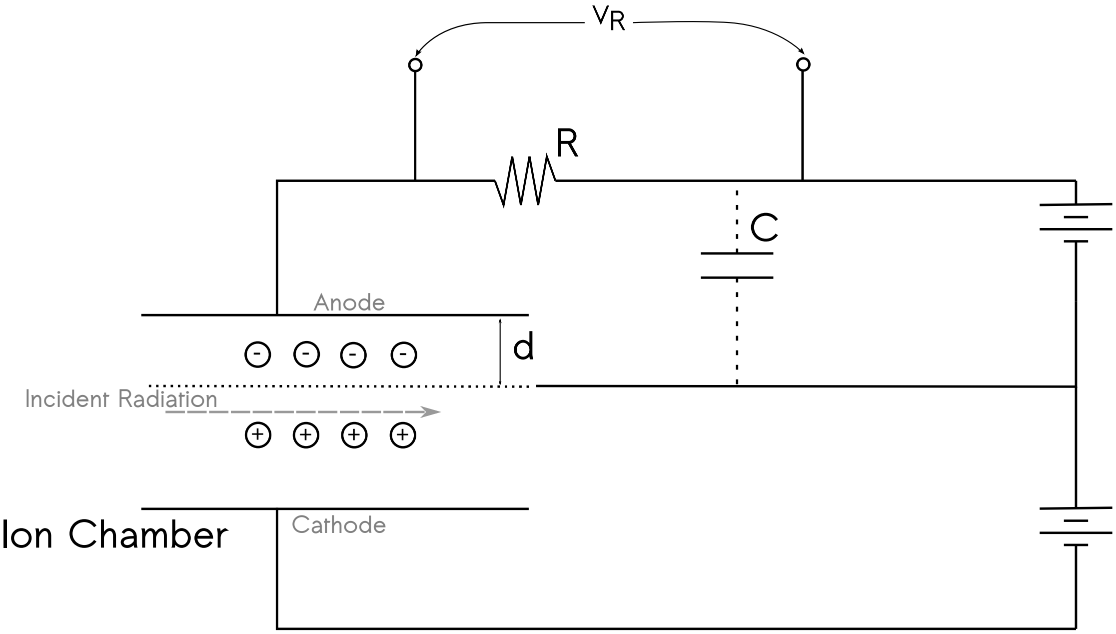

Figure 2.7: Equivalent circuit including Frisch grid drawn for an ionization chamber where the radiation enters parallel to the electrodes.

only the electrons were collected then the response of the detector would be much faster.

The solution was invented in 1944 by Otto Frisch [29] in the form of a grid of wires which is biased to some value between that of the cathode and anode, and placed between the electrodes of the ionization chamber such that the radiation particle stops in the gas between the cathode and the grid. This grid is made as transparent as possible to the electrons, which pass through it en route to the anode, but it shields the anode from the influence of the moving ions. This is more clearly represented in the equivalent circuit drawn in Fig. 2.7, this time with a grid of wires included. The load resistor is now located in a loop separate from the cathode, and so the signal across it reflects changes in the field between the grid and the anode only.

The time-dependent signal across the load resistor is now shown by Eqn. 2.19, where d is now the distance between the grid and the anode, and the effective capacitance is between the grid and the anode. All other symbols are the same as before.

$$V_R = \frac{n_0 e}{dC} \nu_- t \tag{2.19}$$

With this grid in place the maximum signal is still given by Eqn. 2.18. The number of ion pairs produced, n_0, is the same as the number of electrons produced and is determined using Eqn. 2.20, where E is the energy of the incident radiation and W is the average energy needed to create an ion pair (typical W-values were given in Table 2.1).

$$n_0 = \frac{E}{W} \tag{2.20}$$

The size of the signal produced by an α-particle in the TIFFIN detector may be estimated using Eqn. 2.18. The quantities involved are outlined in Table 2.2. From this series of calculations it is clear that the height of the signal generated is directly related to the number of ion pairs produced in the detector. Furthermore, the same information can be gained about the incident radiation by detecting only the electrons as would be gained from detecting the whole ion pairs, but faster.

Table 2.2: The quantities required for the calculations in this chapter. There are two drift velocities listed because the two regions of the detector, which are separated by the Frisch grid, have different electric fields strengths and therefore different drift velocities.

Symbol	Description	Value
W_{P10}	Average energy needed to create an ion pair in P10 gas.	26.58 eV/ion
e	Charge on an electron.	1.6 $\times 10^{-19}$ C
E_α	Alpha particle energy.	5.486 MeV
ϵ_r	Dielectric constant of argon.	1.000127 [30]
ϵ_0	Electric permittivity of free space.	8.54 $\times 10^{-12}$ F/m
d_1	Separation between cathode and Frisch grid.	4.4 cm
d_2	Separation between Frisch grid and anode.	0.4 cm
A	Area overlap of 2 plates.	6.36×10^{-3} m^2 (r = 0.045m)
R	Alpha particle range in detector.	0.0226 m (at 1600 Torr) [31]
m_α	Mass of α-particle.	3.72 GeV/c^2 [32]
ν_{d1}	Drift velocity of electrons in the region between the cathode and the grid.	4 cm/µs (at 0.075 cm^{-1}Torr^{-1})
ν_{d2}	Drift velocity of electrons in the region between the grid and the anode.	5.45 cm/µs (at 0.2 Vcm^{-1}Torr^{-1})

1. Capacitance between the detector plates, C:

$$\begin{aligned} C &= \epsilon_r \epsilon_0 \frac{A}{d_2} \\ &= 1.36 \times 10^{-11} \text{ F} \\ &= 13.6 \text{ pF} \end{aligned} \tag{2.21}$$

2. Number of electrons produced by one α-particle, n_0:

$$\begin{aligned} n_0 &= \frac{E_\alpha}{W_{P10}} \\ &= 2.06 \times 10^5 \text{ electrons} \end{aligned} \tag{2.22}$$

3. Signal produced, V_R:

$$\begin{aligned} V_R &= \frac{n_0 e}{C} \\ &= 2.43 \times 10^{-3} \text{ V} \\ &= 2.43 \text{ mV} \end{aligned} \tag{2.23}$$

It is also possible to estimate the time it takes for a signal to collect in the detector based on its geometry and drift velocity calculations. In the discussion of signal generation the geometry of the theoretical detector in question was such that the radiation being detected entered the chamber parallel to the plates. In order to calculate a signal collection time let us instead consider the scenario that the source is located at the centre of the cathode as shown in Fig. 2.8, as this is the situation in the TIFFIN detector. In this illustration, C is the cathode, FG is the Frisch Grid, A is the anode, ν_{d1} is the drift velocity in the region between C and FG (this is known as the stopping region) and ν_{d2} is the drift velocity in the region between FG and A (this is known as the detection region). $\boldsymbol{\epsilon}_S$ represents the electric field in the stopping region, and $\boldsymbol{\epsilon}_D$ represents the electric field in the detection region. The radiation could be emitted at angles from 0-90°, where at 0° the particle is emitted parallel to the electric field and at 90° it is emitted perpendicular to the electric field. Considering first the case where the radiation is emitted parallel to the electric field:

1. If one assumes a constant velocity of the α-particle for simplicity, then the time, $t_{\alpha_{\text{stop}}}$, for an α particle to stop in P10 at 1600 Torr:

$$E_\alpha = \frac{1}{2}mv^2$$

therefore:

$$\begin{aligned} v &= \sqrt{\frac{2E_\alpha}{m_\alpha}} \qquad (2.24) \\ &= 1.63 \times 10^7 \text{ms}^{-1} \\ t_{\alpha_{\text{stop}}} &= \frac{R}{v} \\ &= \frac{2.26 \times 10^{-2}\text{m}}{1.63 \times 10^7 \text{ms}^{-1}} \\ &= 1.39 \text{ ns} \end{aligned}$$

2. Time, $t_{(\text{first to A})}$, for the first ionization to reach the anode (A):

   - Time to reach the grid (G) from the cathode (C):

$$\begin{aligned} t_{(\text{C to G})} &= \frac{d_1}{\nu_{d1}} \qquad (2.25) \\ &= 1100 \text{ ns} \end{aligned}$$

   - Time to reach the anode from the grid:

$$\begin{aligned} t_{(\text{G to A})} &= \frac{d_2}{\nu_{d2}} \qquad (2.26) \\ &= 73 \text{ ns} \end{aligned}$$

   - Total time from source to anode, $\text{t}_{(\text{first to A})} = t_{(\text{C to G})} + t_{(\text{G to A})} = 1173$ ns.

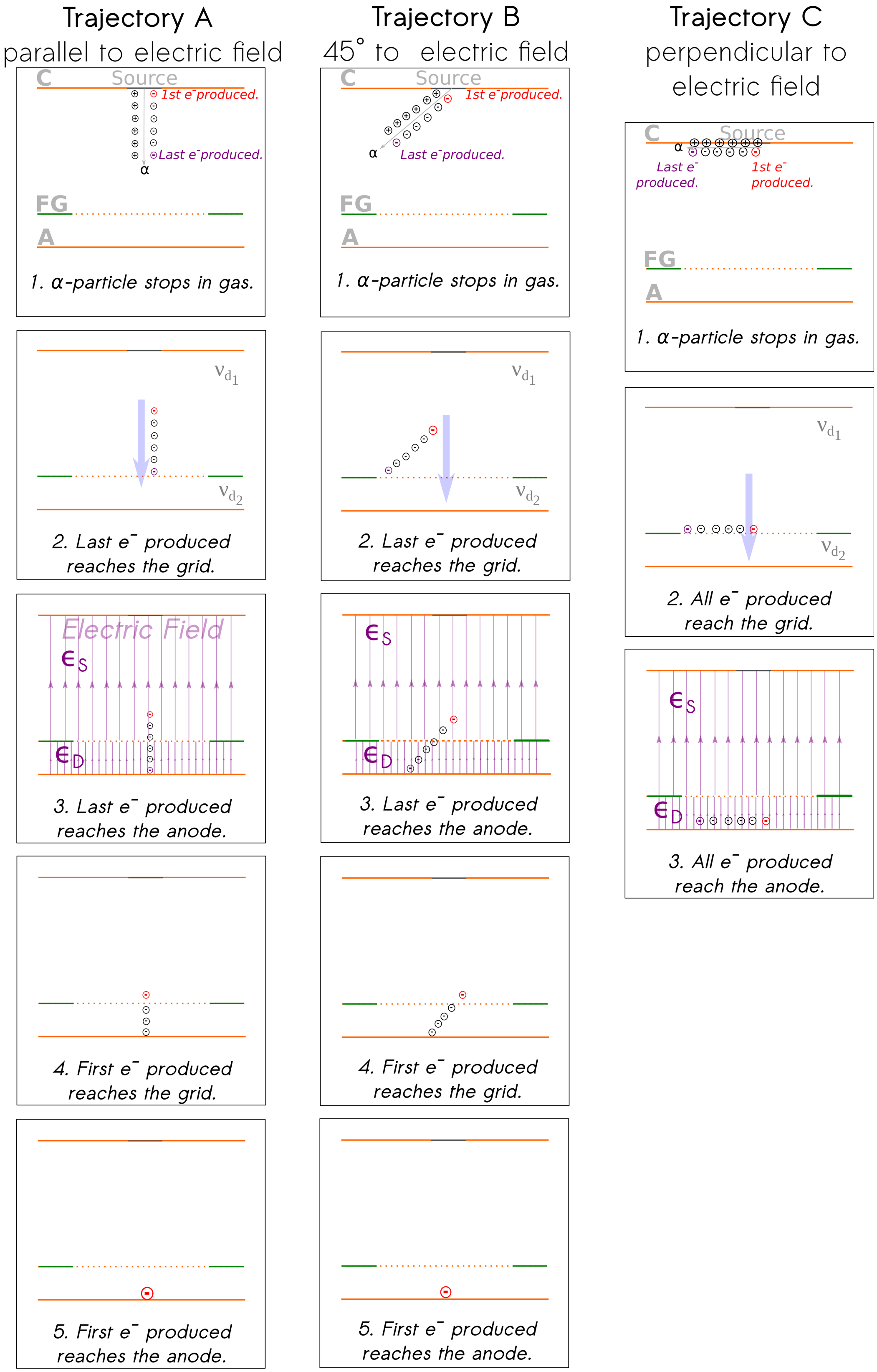

Figure 2.8: An illustration of the various trajectories of an α-particle emitted from an isotropic source and the resultant motion of the electrons produced by ionization of the gas.

3. Time, $t_{(\text{last to A})}$, for the last electron produced to reach the anode (assuming the α-particle has a trajectory parallel to the electric field). The last electron produced is at a distance R away from the cathode and has a distance, x, yet to travel to the grid:

   - Time to reach the grid from the cathode:

$$\begin{aligned} x &= d_1 - R \qquad (2.27) \\ &= 2.14\,\text{cm} \\ t_x &= \frac{x}{\nu_{d1}} + t_{\alpha_{\text{stop}}} \\ &= 536\ \text{ns} \end{aligned}$$

$$(2.28)$$

   - Time to reach the anode from the grid:

$$\begin{aligned} t_{(\text{G to A})} &= \frac{d_2}{\nu_{d2}} \qquad (2.29) \\ &= 73\ \text{ns} \end{aligned}$$

   - Total time from source to anode, $t_{(\text{last to A})} = t_x + t_{(\text{G to A})} = 609$ ns.

These calculations give us the following approximate time line:

#1 α-particle stops in the gas *1.39 ns*

#2 Last electron produced reaches the grid *536 ns*

#3 Last electron produced reaches the anode *609 ns*

#4 First electron produced reaches the grid *1100 ns*

#5 First electron produced reaches the anode *1173 ns*

As the signal seen starts when the last electron produced reaches the grid (#2) and ends when the first electron produced reaches the anode (#5), it can be estimated that the signal will take approximately 634 ns to rise to its full amplitude when the ϵ/P in the stopping region is 0.075 $\text{Vcm}^{-1}\text{Torr}^{-1}$ and 0.2 $\text{cm}^{-1}\text{Torr}^{-1}$ in the detection region.

2.3.4 Risetime Variation

The above calculations were based upon a particle being emitted parallel to the electric field, however, there is a distribution of signal risetimes depending on the track orientation of the isotropically emitted radiation.

If the particle was instead emitted perpendicular to the electric field, the risetime would still start when the first electron passed the Frisch grid into the detection region but, assuming that the electrons travel through the stopping region at the same velocity, all the electrons will pass the grid at the same time. Figure 2.8 shows an illustration of such a scenario as Trajectory C. The risetime then is simply the time to reach the anode from the grid, Eqn. 2.26, 73 ns.

Figure 2.8 illustrates three possible trajectories for α-particles emitted from the source, and the subsequent movement of electrons created in the gas volume as the particle deposits all its energy. Based on calculations (2.24) - (2.27), approximate risetimes for each trajectory may be calculated. It was predicted that the risetime varies between 73 ns and 640 ns when the angle of emission is varied between 0° and 90° for ϵ/P of 0.2 $\mathrm{Vcm^{-1}Torr^{-1}}$ in the stopping region and 0.075 $\mathrm{Vcm^{-1}Torr^{-1}}$ in the detection region.

2.4 Energy Resolution

As previously outlined, radiation is detected in a gas ionization chamber as it produces ion-electron pairs in the gas. The amount of charge produced is directly proportional to the energy of the incident radiation. Due to uncertainties in both the charge production process and charge measurement, an energy distribution is observed for a single charge particle energy. The width of this energy distribution indicates the uncertainty with which an energy measurement can be made. The distribution is caused by a number of factors, some of which are outlined here:

1. statistical uncertainty in charge production,
2. electronic noise,
3. incomplete charge collection,
4. ballistic deficit and,
5. drift in operating characteristics.

The uncertainty in charge production is due to the statistical nature of the processes by which the incident charged particle radiation interacts with the gas. For each collision between the radiation and an atom in the gas, there is some probability of an ion pair being produced. Repeated collisions can be considered as multiple trials and the charge produced as the counted successes, hence charge production may be modelled using the Poisson distribution. The standard deviation of the Poisson distribution is equal to the square root of the mean of the distribution [24]. If n charge carriers are expected to be produced the uncertainty, σ, on this value is therefore $\sqrt{n}$. As a consequence, the fractional uncertainty $\sqrt{n}/n$ decreases as the number of charge carriers increases. Therefore using a gas with a low W-value (the average energy needed to form an ion pair, discussed in Sec. 2.1) results in a smaller statistical uncertainty. For large values of n, the Poisson distribution approximates a Gaussian distribution. Therefore the contribution to the measured energy distribution due to statistical uncertainty is approximated with a Gaussian distribution. The Gaussian distribution function is shown in Eq. 2.30, where A is the area, the standard deviation, σ, is referred to as the width, and x_0 is the peak centroid or the mean value of the distribution.

$$G(x) = \frac{A}{\sigma\sqrt{2\pi}} \exp\left(- \frac{(x - x_0)^2}{2\sigma^2} \right) \tag{2.30}$$

The Full Width at Half Maximum ($FWHM$) i.e. the width of the peak at half of the height of the peak is related to sigma through Eqn. 2.31 [23].

$$FWHM = 2\sqrt{2\ln 2}\,\sigma \simeq 2.35\,\sigma \tag{2.31}$$

The Poisson distribution assumes that each trial is independent - in this case that corresponds to assuming each case of ion pair formation is independent. In reality the probability of ionization occurring depends on previous collisions. This correlation is accounted for with an experimentally determined factor known as the Fano factor; see Eqn. 2.32. This factor varies depending on the detector medium but is found to be ≈ 0.1 for gases [23] and specifically 0.19 for a gas mixture of 92% argon and 8% methane [33].

$$F = \frac{\text{Observed variance in } n}{\text{Poisson predicted variance}(= \sigma^2 = n)} \tag{2.32}$$

The Fano factor can be used then to calculate the theoretical minimum $FWHM$ based on the observed variance from the mean rather than the Poisson predicated variance. The $FWHM$ becomes Eqn. 2.33, where n is the number of ion pairs created and F is the Fano factor. n may be estimated from the energy of the incident radiation, as shown previously in Eqn. 2.20.

$$FWHM = 2.35\sqrt{Fn} \tag{2.33}$$

Equation 2.33 is the uncertainty on n. In order to get the fractional uncertainty on the energy measurement, Eqn. 2.33 must be multiplied by W (the average energy per ion pair produced) and divided by the energy of the incident radiation, E_α. This results in a statistical limit on the energy resolution of 0.23% for 5.486 MeV α-particles in P10 gas.

The charge signal produced by the detector is also convolved with some amount of random electronic noise. In a radiation detector, (provided experimental sources of noise such as ground loops or field inhomogeneities are eliminated) the dominant source of electronic noise is typically thermal noise generated by the thermal agitation of charge carriers inside an electrical conductor. It is proportional to detector capacitance and can also be approximated with a Gaussian distribution.

Whereas statistical uncertainty in charge production and electronic noise produce symmetric contributions that can be approximated with a Gaussian, the final three factors listed would cause asymmetric contributions to the distribution. Incomplete charge collection, where not all the electrons produced by the radiation are collected at the anode, would result in a low energy tail on the energy distribution. This could be caused, for example, by inhomogeneities in the electric field between the plates. A phenomenon referred to as ballistic deficit may prevent the signal from reaching its full height - this will be discussed later in Chap. 4. Finally, drift in operating characteristics may broaden the energy distribution measured. For example, changes in the temperature of the room may cause a drift in the gain of the readout electronics.

As the dominant sources of noise in the detector are the statistical uncertainty on charge production, σ_{stat}, and electronic noise, σ_{elec}, both of which can be well represented with Gaussian distributions, the overall shape of the distribution is also expected to be Gaussian. These contributions can be summed to give a total distribution width, σ_{total} as shown in Eqn. 2.34.

$$\sigma^2_{total} = \sigma^2_{stat} + \sigma^2_{elec} \tag{2.34}$$

The $FWHM$ can be measured experimentally and compared to the theoretical calculation from Eqn. 2.33. The $FWHM$ as a fraction of the experimentally measured mean, $\bar{x}_{\text{exp}}$ is used to establish the resolution of the detector using Eq. 2.35, which is a dimensionless quantity often expressed as a percentage [24].

$$\text{Resolution [\%]} = \frac{FWHM}{\bar{x}_{\text{exp}}} \cdot 100 \tag{2.35}$$

Chapter 3

Literature Review

3.1 Early Radiation Detection

In 1898, the Polish born, French naturalized physicist and chemist, Marie Skłodowska-Curie used an early example of an ionization chamber with uranium, leading to the discovery of radium and polonium with her husband, Pierre. As gas filled detectors were one of the few methods known at the time for charged particle detection, the motivation behind ionization chamber development was to further the general understanding of radioactivity, which had only just been discovered in 1896. Further momentum in the development of the ionization chamber was gained with the discovery of fission.

3.2 Discovery of Fission

Leading up to the discovery of fission, German chemist Otto Hahn wrote to his former colleague, the Austrian physicist Lise Meitner, describing the results of an experiment in which he had bombarded uranium atoms with neutrons and subsequently detected something which appeared to be identical to barium. Meitner discussed this letter with her nephew, the Austrian-British physicist Otto Frisch, and they proposed the mechanism for what is now known as nuclear fission, leading to its discovery in 1939 [34]. They suggested the name "fission" due to the similarity to the splitting of cells in Biology [35].

Experimental evidence for fission was quickly obtained by many laboratories. Frisch used a uranium-lined ionization chamber with a neutron source inside it, and connected the chamber to a linear amplifier to detect bursts of ionization. It was found that no such bursts were detected when the neutron source was not present, and that the number of bursts was proportional to the strength of the neutron source [36].

The discovery of fission provided a much greater variety of isotopes than had been witnessed up until that point, in quantities large enough to study, which meant developments in the understanding of nuclear theory were progressing at an astounding rate [37].

The fission of uranium by neutron bombardment produces more neutrons than it consumes, and so the possibility of a chain reaction to create a "superbomb", or to use for sustained energy production, was proposed very quickly upon its discovery [38]. Research into fission at this point was heavily motivated by the Second World War. In 1940, Frisch and German-born, British physicist Rudolf Pierls initiated the British Atomic Bomb Committee after calculating that an atomic bomb was indeed possible. They soon joined efforts with scientists in America at Los Alamos National Lab as part of the Manhattan Project [35]. The early development of ionization chambers is closely entwined with that of the investigation into fission, as they are ideally suited to the detection of fission fragments.

3.3 Ionization Chamber Development

Gridded Chambers

A major development in ionization chambers was the invention of the gridded chamber in 1940 by Frisch. The addition of a grid of wires between the anode and the cathode meant that if a signal were taken from the anode, it would be shielded from the charge induced by the slow moving, positive, ions and be purely based on the movement of the electrons. As electrons move with a greater velocity than ions under the same electric field, the signal produced from a gridded chamber is faster when shielded in this way. Therefore individual pulses could be measured without "pile-up" (signals stacking on top of one another), and so the energy of each particle detected could be reported. This was discussed at greater length in Chap. 2. The introduction of this grid, soon known as a Frisch grid, changed the electric field environment inside the chamber. In 1949, Bunemann, Cranshaw and Harvey wrote the seminal paper, "Design of Grid Ionization Chambers" which theorized and tested the behaviour of the two electric fields created due to the grid, outlining a criterion to ensure minimal electron capture by the grid, (see Eqn. 3.1 [39]).

$$\frac{\epsilon_D}{\epsilon_S} > \frac{1+\rho}{1-\rho} \tag{3.1}$$

$$\rho = \frac{2\pi r}{\mathrm{p}} \tag{3.2}$$

Written in this form, the parameter ρ, as given by Eqn. 3.2, is entirely geometry dependent: r is the radius of a single grid wire and p is the separation between the grid wires, which is known as the pitch. For a particular detector geometry, the criterion provides a guideline for what bias should be applied to the detector plates to ensure minimal electron capture on the grid wires. In the experiments to test their findings, Bunemann at al. used 10 cm square parallel plates for electrodes, 6 cm apart, housed in a cylindrical chamber filled with argon gas at approximately 2280 Torr. The distance between the cathode and the Frisch grid, shown in Fig. 3.1b as length

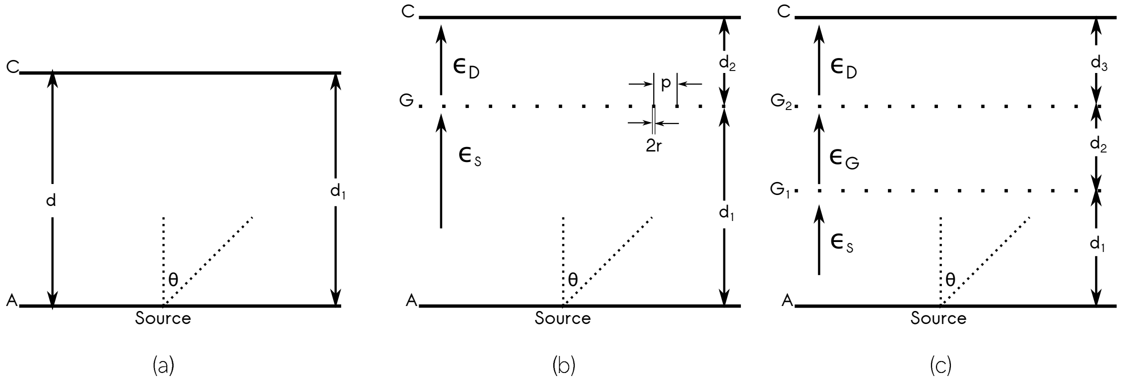

Figure 3.1: (a) Parallel-plate ion chamber; (b) Gridded ion chamber; (c) Two-grid chamber - all with the source located inside the chamber.

d_2, could be either 1.43 cm or 0.67 cm. Two Frisch grids were tested, both made with copper wires, one with a pitch of 14.3 mm and the other with a pitch of 6.7 mm. An energy resolution of 50 keV or ~1% was achieved with a collimated ^{210}Po α source using the smaller value of d_2 and pitch.

Two Grid Chambers

In 1961 Ogawa, Doke and Tsukda described a new type of gridded ionization chamber which featured two grids (G_1 and G_2 in Fig. 3.2), instead of one [40]. A signal was taken from G_1 and G_2 was grounded. Taking a signal from G_1 allowed a crude angle determination, which was used principally for "electronic collimation". The grids were both made of tungsten wires, G_1 had a pitch of 2 mm and G_2 had a pitch of 1 mm. The chamber used was made of iron plated with nickel and filled with argon gas at a pressure of 1650 Torr. The configuration of the plates inside the chamber is shown in Fig. 3.2, where the lengths are given in millimetres. A ^{210}Po α source with an area of 16.5 cm^2 was used to test the detector. The expected pulse height on G_1, V_g, is expressed by Eqn. 3.3, where Q_0 is the total charge of the ions, C_g is the capacitance of the system between the cathode and the grid, d_1 is the distance between the plate labelled K on Fig. 3.2 and G_1, and θ is the angle of emission.

$$V_g = \frac{Q_0}{C_g}\left(1 - \frac{R^*}{d_1} cos\theta\right) \tag{3.3}$$

R^* is referred to in the paper as a quantity which represents the particle range but is independent of θ. Particles emitted at small angles (where an emission angle of 90° is perpendicular to the cathode) suffered significantly from energy straggling in the large, thick sources used, and these signals reduced the resolution unless they could be removed from the data. The second grid was employed for "electronic collimation" by taking only those signals close to $V_g = \frac{Q_0}{C_g}\left(1 - \frac{R^*}{d_1}\right)$, i.e. close to $\theta = 90°$. This was also found to be an effective way of getting rid of background noise. Without the second grid Ogawa et al. saw an energy resolution of 17%; using the second

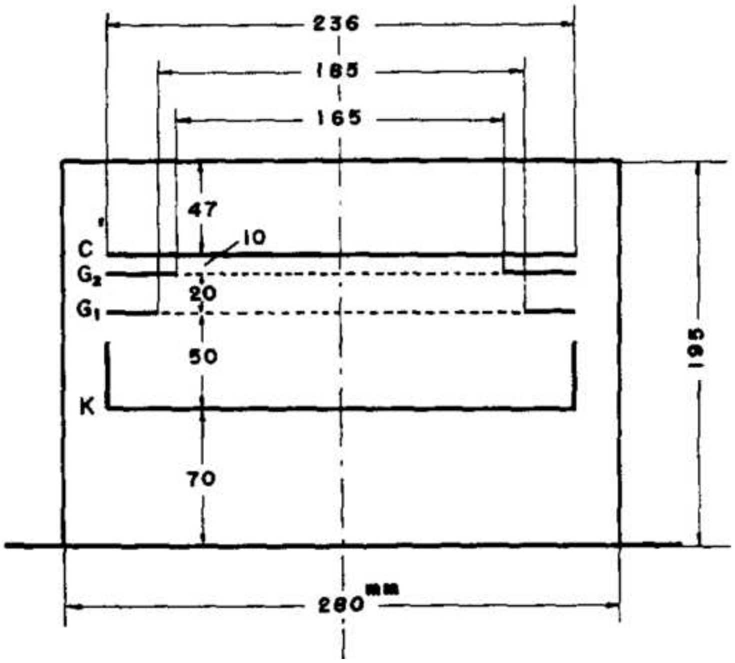

Figure 3.2: Electrode arrangement of Ogawa ionization chamber [40]. Lengths are in millimetres. Reprinted from [40] with permission from Elsevier.

grid a resolution of ≈ 2% was achieved. See Fig. 3.3, reproduced from the paper [40].

In 1975 Sann et al. utilized a second grid referred to as the "θ-grid", to create what they claimed was the "first position-sensitive chamber for detection of heavy ions". Their detector featured a window in one side of the detector where the radiation to be detected entered and travelled almost parallel to the electrodes. The detector configuration is shown in Fig. 3.4. A collimator with 5 slits 3 mm apart and 1 mm wide was installed in front of the entrance window. The grid closest to the cathode is the Frisch grid, and the second grid is the θ-grid. The Cu-Be grid wires were 50 µm in diameter. The Frisch grid had a pitch of 0.8 mm but the θ-grid wires fan out from the approximate point where the radiation enters the detector, with 1° separation between them. This is so that they lie parallel to the track of the radiation entering the detector, regardless of the emission angle. The chamber was made of plexiglass and encased in a grounded aluminium box. The gas used was P10: 10% methane, 90% argon, at a pressure of 450 Torr when using a ^{210}Po α-particle source, and 200 Torr when using the a ^{252}Cf spontaneous fission source for fission fragments. A dehydrating filter of silicagel crystals was used to clean the gas before it entered the chamber.

The energy of the incident radiation was measured from the amplitude of pulses on the anode. The drift time of the electrons from the origin to the Frisch grid was used to determine the x-coordinate, and the y-coordinate was determined with the aid of the θ-grid. The height of the signals induced on the individual wires of the θ-grid take a maximum value for the wires adjacent

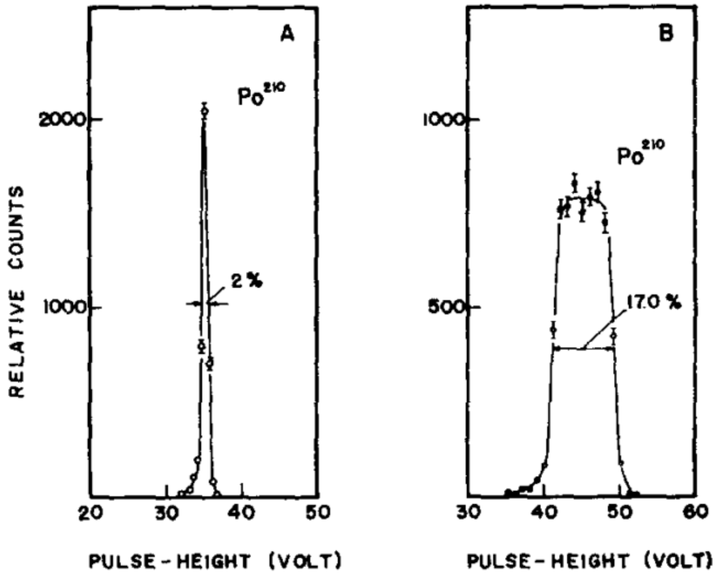

Figure 3.3: Improvement seen with the addition of the second grid which provided electronic collimation. A: Energy spectrum of α-particles from ^{210}Po obtained with the double-grid chamber; B: Energy spectrum obtained with a single-grid chamber [40]. Reprinted from [40] with permission from Elsevier.

to the drift path of the electrons. This allows an emission angle measurement to be taken from which the y-coordinate can be found.

Using this method an energy resolution of 1.2% was achieved for α-particles; a position resolution of Δx <0.8 mm and Δy <1.1 mm, and time resolution of t<2 ns on the drift time was achieved for fission fragments [41].

Segmented Chambers

In 1981 Rosner et al. created an ionization chamber with a segmented anode, thereby inventing a new method for measuring the second position coordinate without the need for a θ-grid [42]. They claimed that using a θ-grid was found to limit the counting rate of the detector and degrade the resolution. Rosner's segmented electrode is shown in Fig. 3.5. It was made from epoxy with a copper layer deposited on it to create the contacts. The trapezoidal shape of the plate was to account for the opening angle of the ionization chamber, and the triangular segments were found to give the best linearity to the results. The chamber was run with P10 gas at a pressure of 80 Torr and a 0.5 mm collimator was used. With this configuration the position resolution in the y direction was 0.3 mm, the energy resolution 0.3 %, and the time resolution 150 ps for 142 MeV ^{32}S ions.

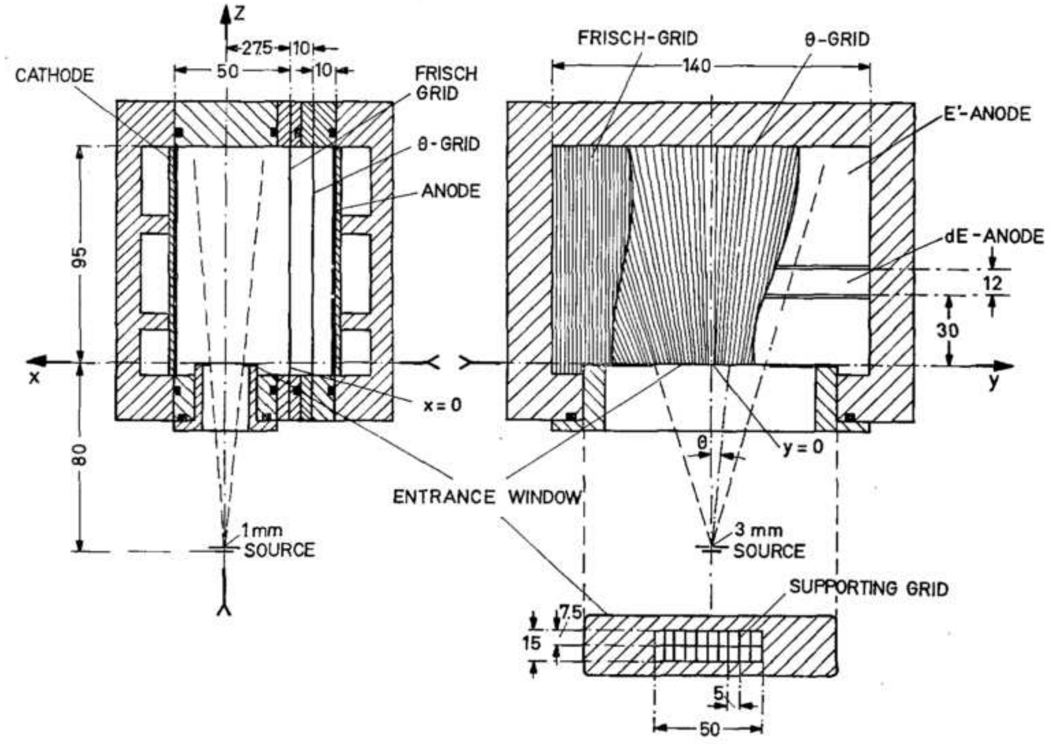

Figure 3.4: Schematic view of the prototype of the position-sensitive ionization chamber made by Sann et al. [41]. Reprinted from [41] with permission from Elsevier.

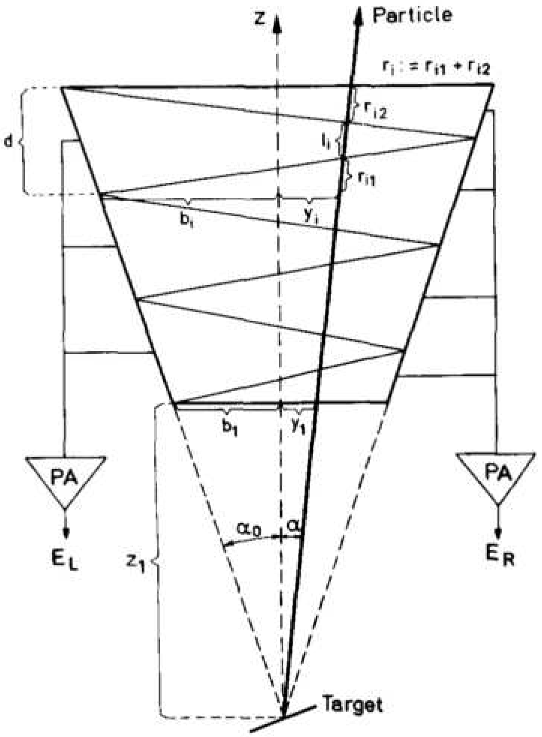

Figure 3.5: Rosner schematic diagram of position sensitive anode [42]. Reprinted from [42] with permission from Elsevier.

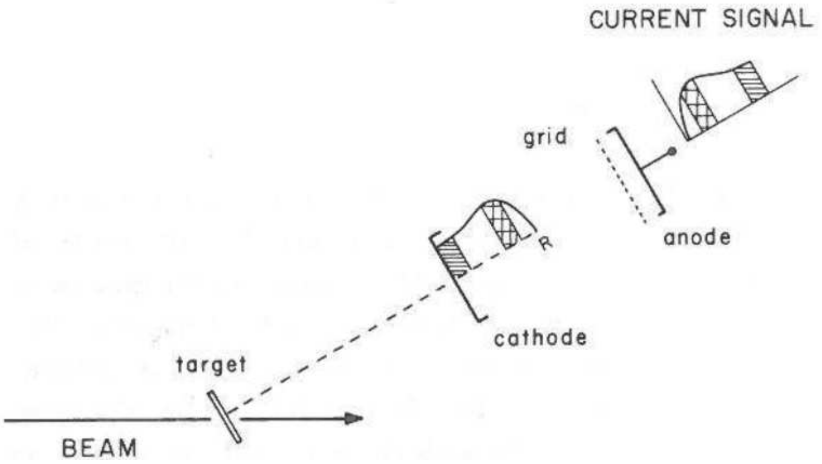

Figure 3.6: The geometry for Gruhn's testing of the Bragg curve spectroscopy concept. Reprinted from [43] with permission from Elsevier.

Bragg Curve Spectrometers

With the increasing use of cyclotron facilities, many detectors were being constructed with a window through which the particles could pass from the beam line. In 1982 Gruhn et al. introduced the then new method of Bragg curve spectroscopy (BCS), which was described in Chap. 2. It was implemented as shown in Fig. 3.6 in an ionization chamber mounted at an angle to the beam line at Lawrence Berkeley National Laboratory, with the intention of providing particle identification [43]. BCS makes use of the fact that the height of the Bragg peak is uniquely linked to the charge of a ion. In this case, the curve itself is deduced from the shape of the risetime of the signal as shown in Fig. 3.6. By measuring the Bragg curve and the range of the particle in the gas they achieved an energy resolution of 0.7% and a charge resolution of 1.2% for ions with $Z \leqslant 26$, but predicted that better charge resolution would have been possible if they were not limited by the energy straggling in the transmission window [43].

Closely following Gruhn's BCS ionization chamber was a similar detector made by Schiessl et al., also in 1982 [44]. This detector uses a field cage, as shown in Fig. 3.7, that ensured that the field lines in the detector were straight, which is important for accurate measurement of the Bragg curve. An energy resolution of 0.4% and a charge resolution of 0.2% were measured for 130 MeV ^{32}S ions.

Twin Ionization Chambers

Twin ionization chambers were being used as early as 1940, when W. Jentschke and F. Prankl used one with a self-supporting, collimated foil of uranium. The source was irradiated with neutrons, and the complimentary fragments emitted from the resulting neutron induced fission were detected in coincidence in the two chambers [45]. The schematic for this detector is shown in Fig. 3.8.

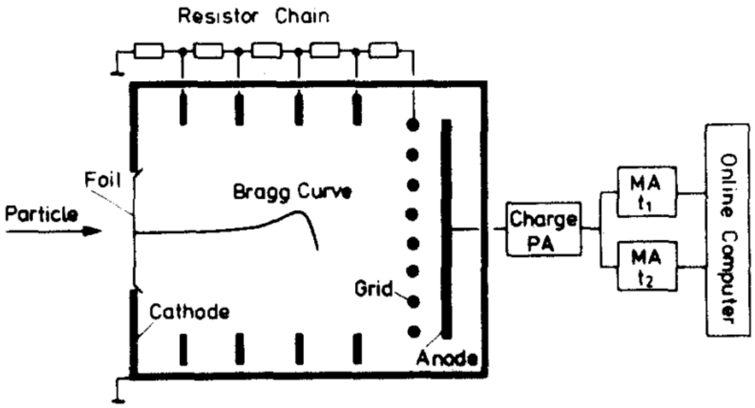

Figure 3.7: Schematic view of Schiessel detector. Reprinted from [44] with permission from Elsevier.

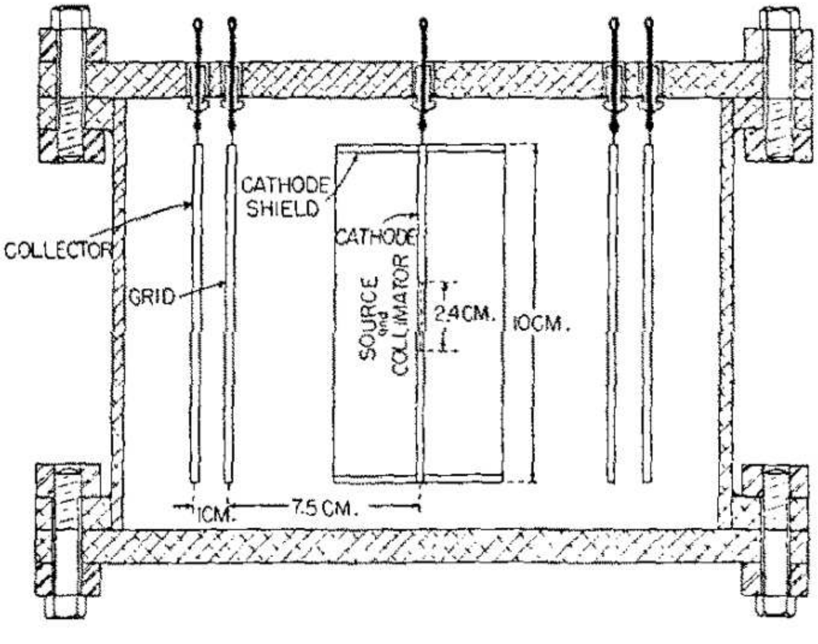

Figure 3.8: A twin ionization chamber used in 1940 by W. Jentschke and F. Prankl with a uranium source irradiated with neutrons to induce fission [45]. Reprinted from [45] with permission from Elsevier.

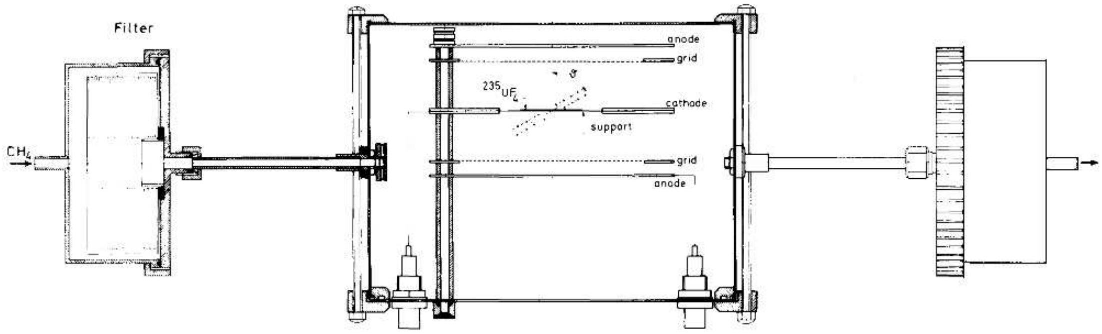

Figure 3.9: A schematic of the twin ionization chamber developed by C. Budtz-Jørgensen et al. The electrodes were circular with a diameter of 12 cm, the anode was made of aluminium and the grids were mounted on stainless steel discs which had an inner diameter of 9 cm. The grids were 0.1 mm wires on a 1 mm pitch. The cathode to grid distance was 2.3 cm and the grid to anode distance was 0.7 cm [47]. Reprinted from [47] with permission from Elsevier.

By detecting both fragment energies and applying laws of mass and momentum conservation (but neglecting neutron emission), they found that it is possible to determine the mass of the emitted fragments, as shown in Eqn. 3.4 where the sub-scripts L and H stand for light and heavy fragment respectively. However, this relation only stands in the case of cold fission, i.e. when no neutrons are emitted from the fission fragments. Using this detector they were amongst the first to show the mass asymmetry of fragments produced from the fission of ^{235}U.

$$\frac{E_L}{E_H} = \frac{M_H}{M_L} \tag{3.4}$$

A twin ionization chamber was build by Knitter and Budtz-Jørgensen et al. in 1982 [46], and with various collaborators Knitter and Budtz-Jørgensen went on to do much work through the 1980's using a gridded twin ionization chamber to measure fission fragments, culminating in their paper with Straede, Hambsch and Vogt in 1987 which inspired the design for the TIFFIN detector [47]. The schematic of the Budtz-Jørgensen et al. detector is shown in Fig. 3.9. It features two anodes 12 cm in diameter, two Frisch grids of steel wires, where each wire has a diameter of 0.1 mm, on a 1 mm pitch, and a common cathode where the fissile source material is mounted. In this case both ^{235}UF$_4$ and ^{252}Cf sources were used. Different to other detectors discussed in this chapter, the Budtz-Jørgensen chamber features a gas flow system to maintain a steady pressure of 750 Torr in the chamber and to remove fission fragments stopped in the gas. Both pure methane and the P10 mixture were tested, and it was found that P10 resulted in slightly lower angular resolution. It is speculated in the paper that this could mean that the resolution is limited by angular dispersion in the gas due to atomic collisions which would be more prominent in heavier gases such as argon. An energy resolution of <0.5 MeV for cold fission fragments is reported, a mass resolution of ∼2 atomic mass units, and a charge resolution of better than 1.5 charge units when using the Bragg curve spectroscopy technique.

3.4 Advantages of the TIFFIN Detector

Although there are now other very good methods of detecting charged particles, ionization chambers are ideally suited for use with fission sources for a number of reasons. Fission fragments are very heavy and cause significant damage to solid state detectors, which results in a reduction of performance over time, whereas ionization chambers experience no such damage. By putting the source of radiation inside the detector chamber the detection efficiency is much greater than for solid detectors, which are limited by their solid angle coverage. Furthermore, ionization chambers are versatile in their operating parameters, allowing a wide range of particle masses and energies to be detected.

TIFFIN will ultimately incorporate many of the positive aspects of past detectors. It will have Frisch grids allowing energy measurements; it will be double sided allowing mass measurements; it will be segmented and use digital signal processing, allowing improved charge measurements. In past ionization detectors either physical or electronic collimation has been used to eliminate those particles emitted at large angles to normal. The TIFFIN detector will utilize digital readout and processing for pulse shape analysis to correct for losses due to angular distribution, thereby improving the efficiency of the detector and preventing the need for any sort of collimation.

Chapter 4

The TIFFIN Detector

4.1 Single-sided Prototype Geometry

The single-sided chamber prototype of the TIFFIN detector is shown in Fig. 4.1. It consists of three electrodes 120 mm in diameter; a copper cathode and anode, both made by the Mechanical Workshop at SFU and a Frisch Grid which was designed by the Electronics Shop at SFU. The cathode features a hole into which a radioactive source can be placed. The Frisch grid has an inner diameter of 90 mm and is hand-strung with gold-plated, 0.07 mm diameter wires on a 1 mm pitch, which was done with the assistance of the Detector Group at TRIUMF. A photo of one of the grids is shown in Fig. 4.2. The grid and the anode are 44 mm and 48 mm away from the cathode respectively. The plates are fixed to a sturdy brass plate to reduce vibrations, centred inside a stainless steel 13 litre chamber. When in operation the chamber is filled with P10 gas (10% methane, 90% argon), and a dedicated gas flow system attached to the chamber allows the pressure of gas to be regulated.

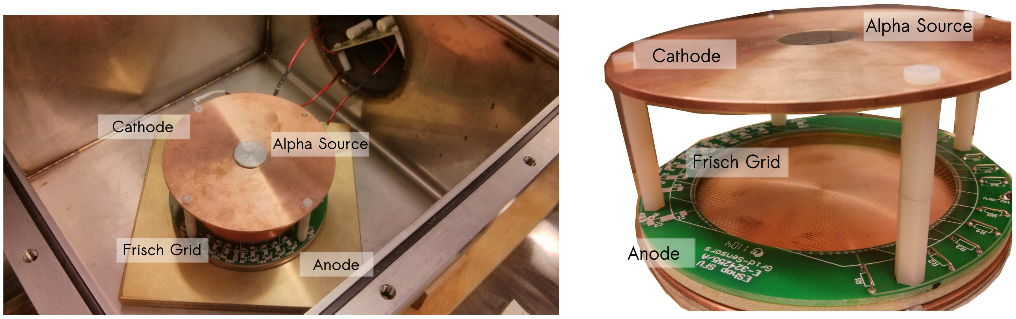

Figure 4.1: The photo on the left shows the inside of the TIFFIN detector chamber. The detector plates are screwed down onto a brass plate with plastic screws to reduce vibrations. The anode is electrically isolated from the brass plate. On the right, a photo of the TIFFIN detector plates.

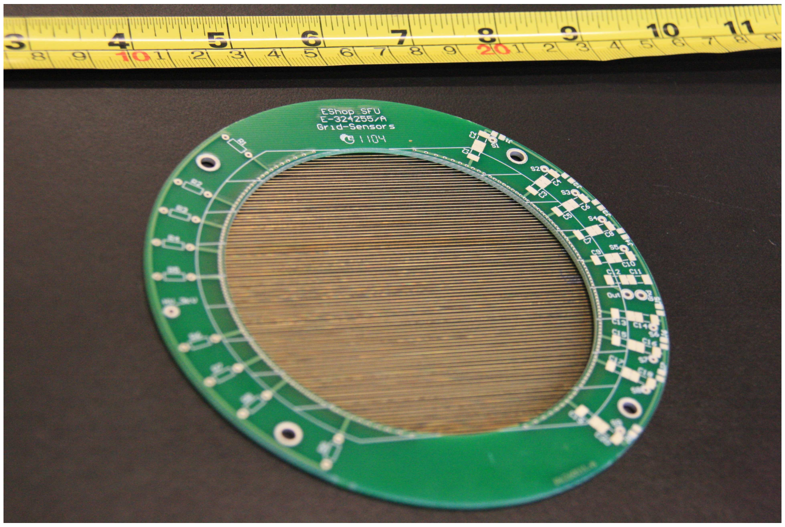

Figure 4.2: A photo of one of the Frisch grids made for this work.

4.2 Gas Handling System

The importance of pressure for range and electron drift velocity was outlined in Sec. 2.1.4 and Sec. 2.3.1 respectively. The stability of the pressure of the gas within the chamber is therefore integral to the reliable operation of the detector. For this reason, a gas handling system has been developed to monitor and regulate the pressure in the chamber. The full system is shown in the lab in Fig. 4.3, and a schematic in Fig. 4.4 shows detail hidden in the photograph.

The gas control system consists of three key parts:

1. *MKS Type M100b Mass-Flo® Controller [48], located downstream of the chamber:*
   This mass flow control unit from MKS Instruments allows a controlled flow of gas out of the chamber. The desired flow of gas is set by the user, and this remains constant regardless of the pressure upstream or downstream from the unit.

2. *MKS πPC PC99 Integrated Pressure Controller with Mass Flow Meter [49], located upstream of the chamber:*
   The πPC from MKS Instruments allows the user to specify a desired pressure to be maintained downstream from the unit via the flow of gas allowed through the device.

3. *MKS Baratron® Type 722B Absolute Pressure Transducer [50]:*
   A separate measure of the pressure inside the chamber.

All three units report their respective pressure and flow measurements to a 4-channel MFC power supply and controller, the CCR Model 400, from which set-points can be programmed. The system features three pneumatically actuated valves and one solenoid valve, all of which are controlled from a central location. The system has two gas inputs and the valves allow the

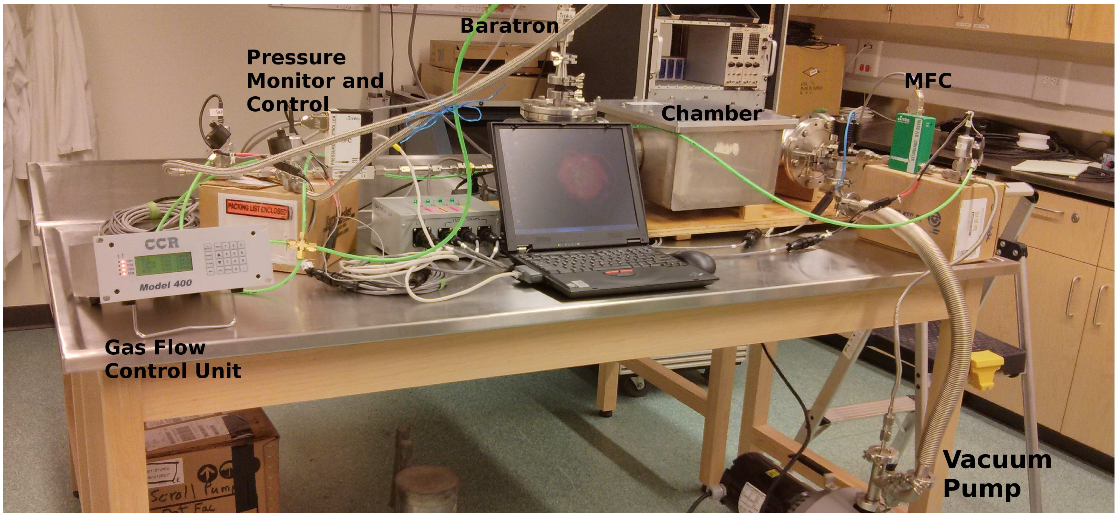

Figure 4.3: The TIFFIN detector set-up at Simon Fraser University.

user to control which gas enters the chamber. The detector is operated with P10 gas, which is explosive at volumes between 45% and 51% in air [51] and if it is exposed to an ignition source. For this reason the second input is pure argon, which is used to flush out the chamber after running, to ensure all traces of P10 are removed before opening to air.

4.3 Electronics and Signal Processing

Attached to the plates inside the chamber is the wiring for applying bias and receiving signals when particles are detected. A schematic for the electronics is shown in Fig. 4.5. The combination of resistor and capacitor in the wiring to the bias supply form a low pass filter, which increases the stability of the voltage supply by allowing high frequency spikes to bleed off to ground through the capacitor. The cathode and the grid can be biased up to 4000 V; the anode is at ground.

4.3.1 Pre-amplifier

The output from the detector is shaped by a preamplifier to allow it to be transmitted through potentially very long cables to the data acquisition system (DAQ). Resistance between the detector and the preamplifier may decrease the signal-to-noise ratio. Therefore it is important that the preamplifier be located as close to the detector as possible. The preamplifier changes the decay length of the signal as a short signal pulse coming directly from the detector is not convenient for measurement. The longer duration signal from the preamplifier output allows repeated sampling by the digital DAQ. The random electronic noise on the signal averages towards zero over the multiple samples, increasing the precision of the measurement.

The preamplifier used for this work was a charge-sensitive model made by the SFU Electronics Shop using a Cremat CR-110 preamplifier chip [53]. The voltage output of the preamplifier is

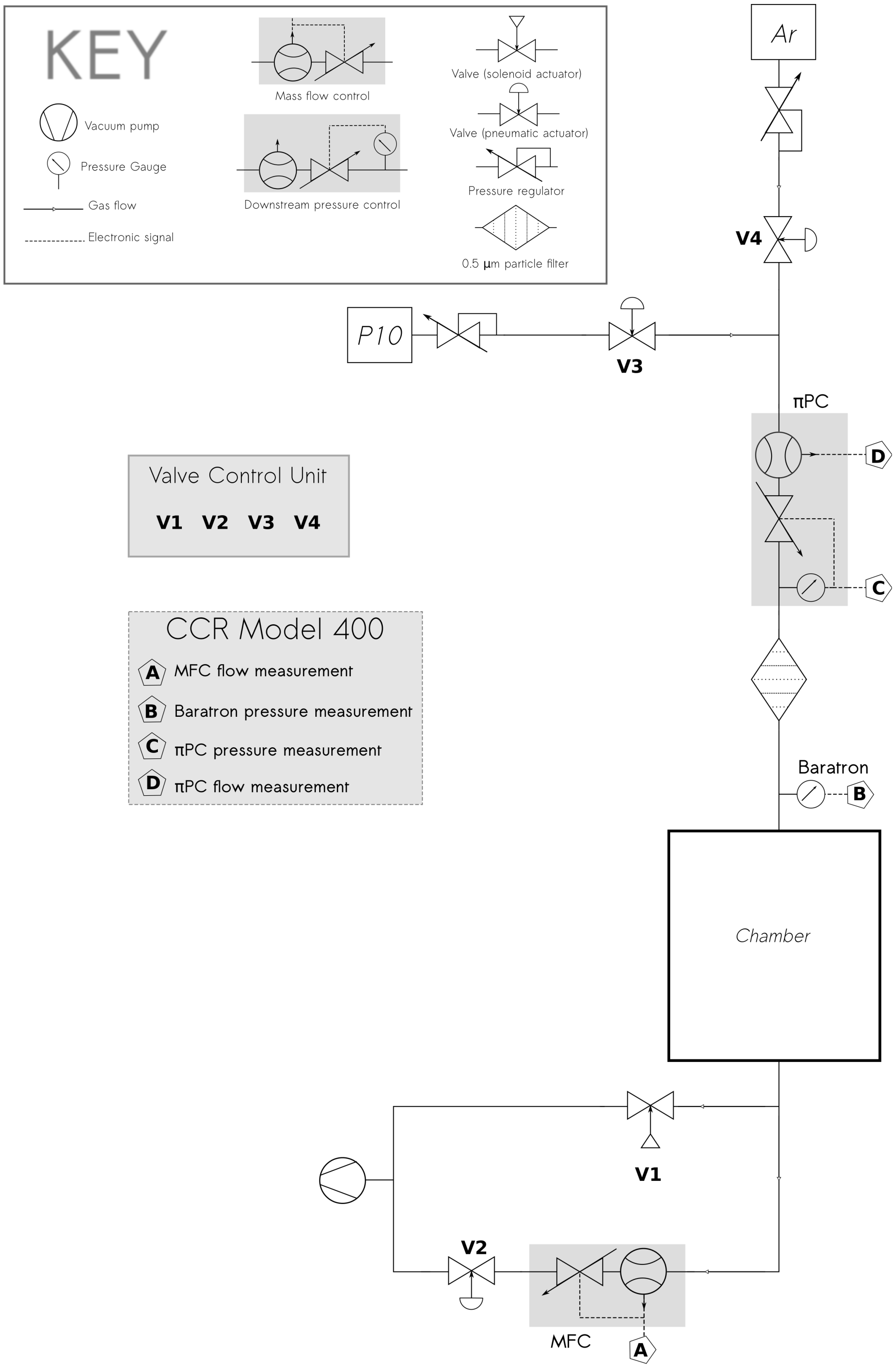

Figure 4.4: Schematic of the detector set-up to illustrate the gas flow system.

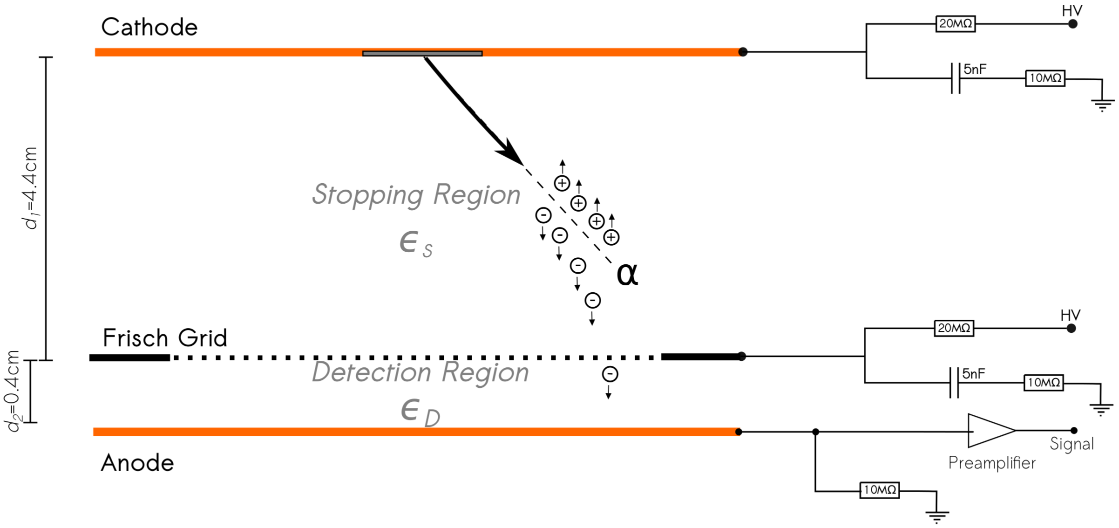

Figure 4.5: Schematic of the detector including detector electronics. The cathode holds the radiation source and is negatively biased. The signal is taken from the anode which is at ground. The Frisch grid is at an intermediate potential between the cathode and the anode.

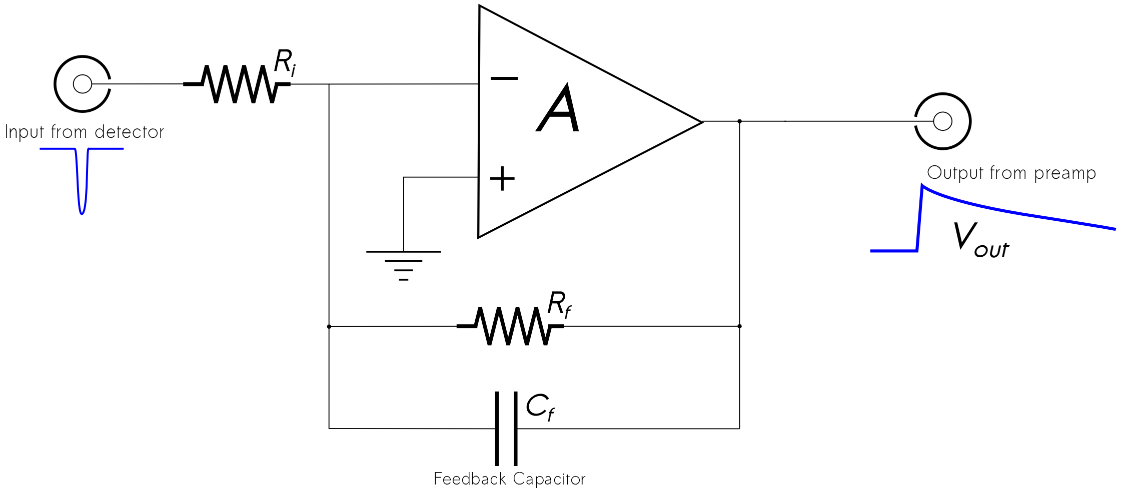

Figure 4.6: A simplified schematic of an inverting, charge-sensitive preamplifier adapted from [52].

proportional to the total integrated charge from the input [24]. The size of the voltage output is dictated by the gain, A, of the preamplifier as shown in Eqn. 4.1. In this case the CR-110 preamplifier chip had a gain of 1.4 V/pC. This voltage was then further amplified by operational amplifiers added into the final preamplifier design by the Electronics Shop.

$$V_{\mathrm{out}} = A \cdot Q_{\mathrm{in}} \tag{4.1}$$

A simplified diagram of a charge-sensitive preamplifier is shown in Fig. 4.6, and the detailed electronic drawing of the preamplifier from the SFU Electronics Workshop is included in Appendix A. The equivalent voltage signal from the detector, V_{in}, charges the feedback capacitor, C_{f}, which subsequently decays through the resistor, R_{f}, thereby creating an exponential tail to the signal from the preamplifier, V_{out}.

This can be understood by first outlining the following laws and definitions:

Kirchoff's Voltage Law, sum of voltage drops around a closed loop = sum of voltage sources

Ohm's Law, $V = IR$

Definition of capacitance, $C = \frac{Q}{V}$

Definition of current, $I = \frac{\mathrm{d}Q}{\mathrm{d}t}$

The RC circuit in Fig. 4.6 is a closed loop. Applying Kirchoff's Voltage Law yields Eqn. 4.2 for the voltages across the two components in the loop: namely the feedback capacitor and feedback resistor.

$$0 = V_{C_{\mathrm{f}}} + V_{R_{\mathrm{f}}} \tag{4.2}$$

This equation may be re-written using Ohm's Law and the definition of capacitance as Eqn. 4.3 and re-arranged to Eqn. 4.4.

$$0 = \frac{Q}{C_{\mathrm{f}}} + IR_{\mathrm{f}} \tag{4.3}$$

$$I = \frac{-Q}{R_{\mathrm{f}}C_{\mathrm{f}}} \tag{4.4}$$

Using the definition of current this becomes Eqn. 4.5. The solution to this differential equation is shown in Eqn. 4.6, where Q_{max} is the full charge on the capacitor at $t = 0$ when it starts discharging. $R_{\mathrm{f}}C_{\mathrm{f}}$ is known as the time constant, τ_{RC}. It is the time for the charge on the capacitor to fall to Q_{max}/e.

$$\frac{\mathrm{d}Q}{\mathrm{d}t} = \frac{-Q}{R_{\mathrm{f}}C_{\mathrm{f}}} \tag{4.5}$$

$$Q = Q_{\mathrm{max}}\, e^{\frac{-t}{R_{\mathrm{f}}C_{\mathrm{f}}}} \tag{4.6}$$

By differentiating Eqn. 4.6 to find the current, then using definition of capacitance and Ohm's law, it is shown that the output voltage also decays exponentially: Eqn. 4.7. Thus the RC circuit in the preamplifier creates an exponential decay tail on the signal produced.

$$V_{\text{out}} = V_{\text{max}}\, e^{-\frac{t}{\tau_{RC}}} \tag{4.7}$$

Ballistic Deficit

The charge integrated across the preamplifier begins to decay as soon as the preamplifier starts to charge. If the signal risetime is comparable to the decay time of the signal, the signal will not reach its full amplitude. This effect of the preamplifier decay on the signal amplitude is known as ballistic deficit. If the signal risetimes are consistent, even a large ballistic deficit is easily handled as it can be calibrated out. However, if there is a large variety of risetimes then the impact of the ballistic deficit becomes more of an issue. The preamplifier decay time is made to be long to minimize the impact on the signal height from ballistic deficit. The signal from the preamplifier can be divided into two parts: the rise and the fall. The rise time can be assumed to take the form $\left(1 - e^{-\frac{t}{\tau_R}}\right)$ where τ_R is dependent on the detector. The fall can be assumed to take the form $e^{-\frac{t}{\tau_{RC}}}$ where τ_{RC} is dependent on the RC constant of the preamplifier. The total signal therefore can be described by Eqn. 4.8 where A is the signal amplitude, A_{max} is the maximum value of the amplitude, t is the time elapsed since the signal began to rise, τ_R and τ_{RC} are the risetime and the decay time constants respectively.

$$A = A_{\text{max}}\left(1 - e^{-\frac{t}{\tau_R}}\right)e^{-\frac{t}{\tau_{RC}}} \tag{4.8}$$

Differentiating Eqn. 4.8 with respect to t and solving for the time at which a maximum is reached gives the result shown in Eqn. 4.9.

$$t_{\text{max}} = \tau_R \ln\left(\frac{\tau_R + \tau_{RC}}{\tau_R}\right) \tag{4.9}$$

An estimate of the impact from the ballistic deficit is attained by using the result from Eqn. 4.9 for given values of τ_R and τ_{RC} in Eqn. 4.8 and assuming a maximum amplitude, $A_{\text{max}} = 1$. For example, if the values of τ_R and τ_{RC} are 1 µs and 100 µs respectively, the signal reaches 95% of the full amplitude due to the decay of the preamplifier. A range of risetimes are expected from the detector. In the examples calculated in Sec. 2.3.3 the variation was between 73 ns and 640 ns. The ballistic deficit expected for the risetimes calculated using Eqn. 4.8 is a reduction in signal height of 4% for a risetime of 73 ns and 5% for 640 ns which would affect the energy resolution on the order of 1%. If τ_R and τ_{RC} are such that ballistic deficit is an issue, then the significance of the impact depends on the signal risetime. In this case a correlation between risetime and signal amplitude will be observed for incident radiation of the same energy, where long risetimes will correspond to a smaller than average signal amplitude being measured.

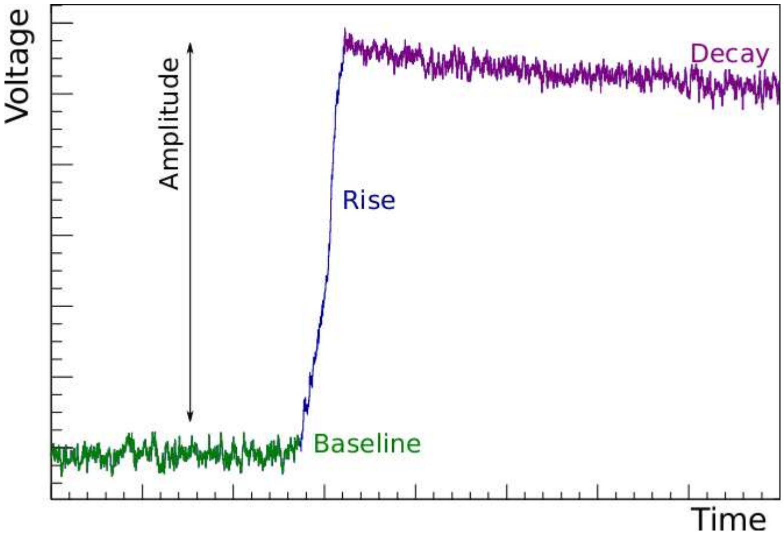

Figure 4.7: A waveform recorded by the DAQ during this work.

4.3.2 Data Acquisition System

The preamplifier passes the signal onto the data acquisition system. The data acquisition system (DAQ) used for this work was a fully digital system originally designed for the TRIUMF-ISAC Gamma-Ray Escape Suppressed Spectrometer (TIGRESS) at TRIUMF [54]. The system includes: TIG-10 digitizer cards, each of which can take ten inputs; TIG-C collector cards, configured to be either a master or a slave. Each slave can take the input from twelve TIG-10s and the master can take the input from twelve slaves. In its current form the detector only requires a single channel, but many channels will be required in the future.

The signal from the preamplifier is an analog voltage. This signal is digitised by a TIG-10 card which features a 14 bit analog-to-digital converter with a sampling rate of 100 MHz, allowing the output voltage from the preamplifier to be sampled every 10 ns. The TIG-10 identifies the presence of signals from the detector and measures the signal amplitude online. This will be explained in more detail below.

This method of data collection allows the signal shape itself to be captured along with the energy and timing information available to analog systems. These recorded signal shapes are called waveforms. A waveform from this work is shown in Fig. 4.7. Waveforms of 40 µs in length were recorded by the DAQ to use for offline analysis, allowing precision risetime measurements to be made. The offline analysis done as part of this work is explained in Chapter 5 with the results.

Triggering

The DAQ features a “trigger” which identifies when data should be recorded. Effective triggering ensures that the timing of information read out from the digitisers coincides with the occurrence

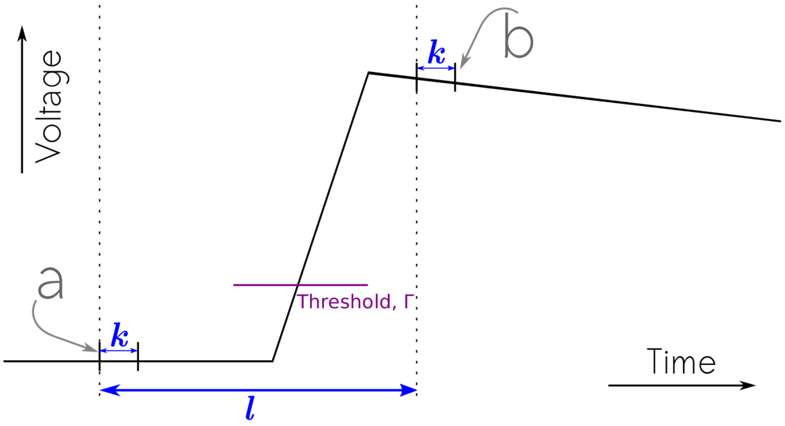

Figure 4.8: A visualization of the parameters relevant to triggering.

of events of interest. The DAQ continuously records the input but only reports to the user when the trigger conditions are met. A threshold value, Γ, is used to determine if the system should record the data or not. To assess when the threshold has been crossed, two windows are set, shown as a and b in Fig. 4.8. The windows are of width k and separated by a time l. If the difference between the averaged sum of the points in each window is greater than the scaled Γ as shown in Eqn. 4.10, then the trigger statement returns "true", a trigger signal is sent, the amplitude of the signal is evaluated, and the waveform is recorded if required. If the difference is not greater, then a "false" status is returned and nothing is recorded.

$$\text{if } \left(\frac{1}{k+1} \sum_{i=0}^{k} \mathrm{b}_i - \frac{1}{k+1} \sum_{i=0}^{k} \mathrm{a}_i \geqslant \Gamma \times (k+1) \right) \text{ then return true} \tag{4.10}$$

Signal Amplitude Evaluation

The signal amplitude evaluation process employs various filters, which are illustrated Fig. 4.9.

1. **Difference Filter**

   Starting with the raw waveform, the difference filter replaces each point with a value F_n, where F_n is the difference between the original value at that point, D_n and the value of a point L points behind it, D_{n-L} as shown in Eqn. 4.11. The result is a trapezoidal shaped function where the flat top of the trapezoid corresponds to when the point D_n is after the rise and $D_{n-\mathrm{L}}$ is on the baseline. Therefore the difference window, L, should be larger than the risetime, r, to ensure that the rise of the signal is preserved. If L is too narrow the full rise will not be seen, resulting in a triangular rather than trapezoid shape. The difference filter acts as a high pass filter and also removes any signal offset, to give an absolute signal amplitude whilst preserving the risetime.

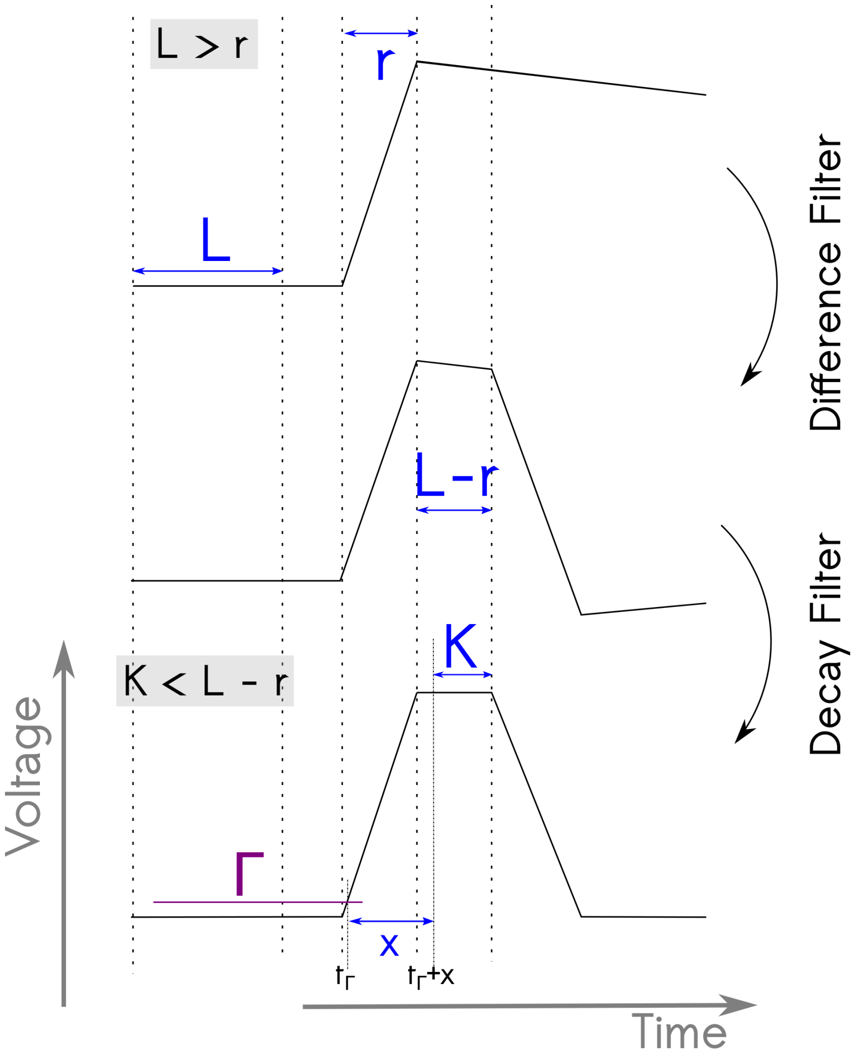

Figure 4.9: The processing of a raw waveform by the TIG10 digitiser in order to evaluate the energy of the signal.

$$F_n = D_n - D_{n-L} \tag{4.11}$$

2. **Decay Filter**

   Taking the output from the difference filter, the decay filter accounts for the fact that the top of the trapezoid is not flat. This is due to the decay of the preamplifier used in the experiment. A fractional amount depending on the decay time constant, τ of the preamplifier in question is added back to each point in an attempt to correct for this. This is done by applying Eqn. 4.12 to the signal, where M is the time constant in units of data samples.

$$G_n = F_n + \frac{1}{M}\sum_{i=1}^{L} D_{n-i} \tag{4.12}$$

3. **Integration Filter**

   Finally, after the first two filters have been applied, the last stage is to take an average over the now flat top of the trapezoid in order to determine the signal amplitude, E. To do this an "integration delay" (x) is set to account for the remaining risetime above the value at Γ, and if set correctly, this will ensure that the integration window is on the flat top of the trapezoid. The integration then is the sum of the points G_n starting with the value of G_n at a time $(t_\Gamma + x)$, as shown in Fig. 4.9, over a window of time, K.

$$E = \frac{1}{K}\sum_{i=1}^{K-1} G_{n-i} \tag{4.13}$$

Once the amplitude of a signal has been evaluated it is used to increment a pulse-amplitude histogram, or spectrum. In this spectrum the width of a peak from a monoenergetic source can be measured to determine the detector's energy resolution, as discussed in Sec. 2.4.

The DAQ must be set up differently depending on the signal anticipated. For example, the signals from TIFFIN have a long risetime compared to signals from a germanium detector (μs compared to ns), and this is accounted for in the DAQ settings which are controlled by the user. The user sets a threshold value for the triggering which is larger than the average random fluctuation in baseline but smaller than the amplitude of a signal in the online interface that is used to control the DAQ. The user also sets the parameters k and l used for triggering, which are known as the "Trigger Integration" and the "Trigger Clip Delay", as well as the values of K, L and M which are used for the signal amplitude evaluation.

4.4 Future Detector Developments

As outlined in Chap. 1, TIFFIN will be used for fission fragment detection. In order to identify fission fragments a mass measurement in conjunction with nuclear charge identification is necessary.

The TIFFIN prototype presented here is a single-sided detector. This design must be extended to a double-sided geometry with segmentation implemented in order to allow the measurement of fission fragment masses and charges. This section will briefly cover these intended upgrades.

4.4.1 Mass Measurement

If the fission fragments detected are selected such that their total kinetic energy is almost that of the Q-value of the reaction, then neutron emission is prohibited and collinear trajectories may be assumed [47]. By measuring the energy of these fragments and knowing the mass of the parent it is possible to deduce the mass of the daughters using the conservation of mass and linear momentum. If the initial momentum of the parent nucleus is zero and the daughter fragments are emitted on collinear trajectories, the conservation of linear momentum implies Eqn. 4.14, where for a parent nucleus of mass A, A_H and A_L are the masses of the heavy and light daughter fragments respectively. Similarly, p_H, p_L, v_H and v_L are the momenta and velocities of the fragments.

$$\begin{aligned} p_L &= -p_H \\ A_L\, v_L &= -A_H\, v_H \end{aligned} \tag{4.14}$$

Each daughter nucleus has kinetic energy equal to $\frac{1}{2}mv^2$, where m is either A_H or A_L. Solving for the velocity, v, for each daughter and substituting into Eqn. 4.14 yields Eqn. 4.15, which can be rearranged to Eqn. 4.16. E_H and E_L are the kinetic energies of the fragments.

$$A_L\sqrt{\frac{2E_L}{A_L}} = A_H\sqrt{\frac{2E_H}{A_H}} \tag{4.15}$$

$$A_L E_L = A_H E_H \tag{4.16}$$

Since the sum of the masses of the two daughter fragments is equal to the parent, $A = A_L + A_H$, it is possible to eliminate one fragment mass and solve for the other, as shown in Eqn. 4.17 and similarly in Eqn. 4.18.

$$A_H = \frac{AE_L}{E_L} + E_H \tag{4.17}$$

$$A_L = \frac{AE_H}{E_L} + E_H \tag{4.18}$$

To measure two fragments simultaneously the detector must be double sided, hence the advantageous 2 × 2π geometry proposed. Figure 4.10 shows a schematic of the double sided detector and a photograph of the plates to be used for the final design.

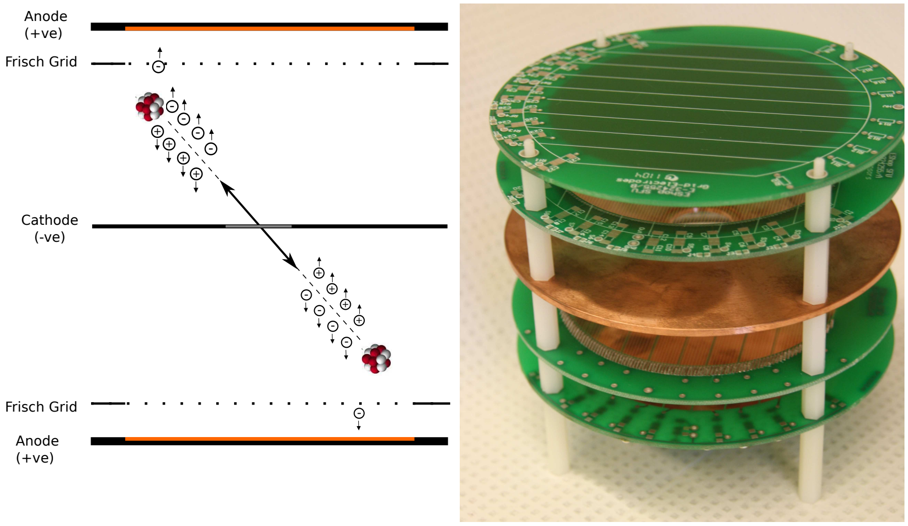

Figure 4.10: A schematic of the full TIFFIN detector and a photograph of the plates without electronics attached.

4.4.2 Charge Measurement

If TIFFIN is to be able to identify the nuclear charge of radiation inside the detector using the Bragg curve spectroscopy method outlined in Chap. 3, it must be able to determine the distribution of free charge created. In the past this has been done using the shape of the signal risetime. TIFFIN will utilize the risetime in addition to segmentation to access the distribution of charge deposition in the detector. Figure 4.11 shows the segmented cathode that will be used, as well as the Frisch grid which has the functionality to implement segmentation. There are nine segments on each electrode, resulting in a total of thirty-six channels.

Due to the isotropic nature of the source the track orientation varies significantly between signals, and this will be evident in the distribution of observed risetimes. As explained in Chap. 2, the distribution of charge deposition along the track of the radiation species is not uniform and depends on the nuclear charge of the incident particle. A particle with a greater nuclear charge will exhibit a faster rate of energy deposition in the gas and therefore a smaller range. Segmentation can therefore be used in order to determine the distribution of this energy deposition. Figure 4.12 illustrates an α particle, emitted at an angle θ to the cathode, depositing charge on multiple segments on the anode after passing through the grid. By taking signals from each of the segments and using the risetime to determine the track orientation, it will be possible to reconstruct the charge distribution along the track, which can be used for identifying the nuclear charge of the particle. Using this information in combination with a mass measurement determined from fragment energies, as shown in Sec. 4.4.1, improved fragment identification is possible.

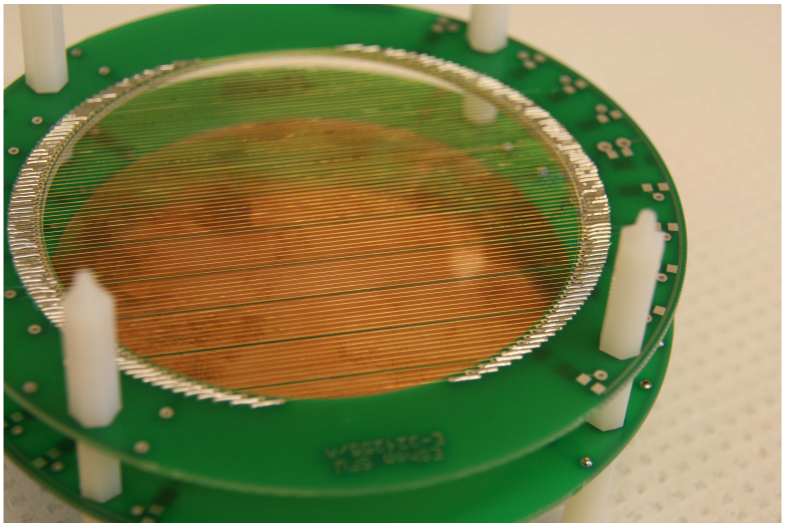

Figure 4.11: A photograph of one segmented plate and segmented Frisch grid.

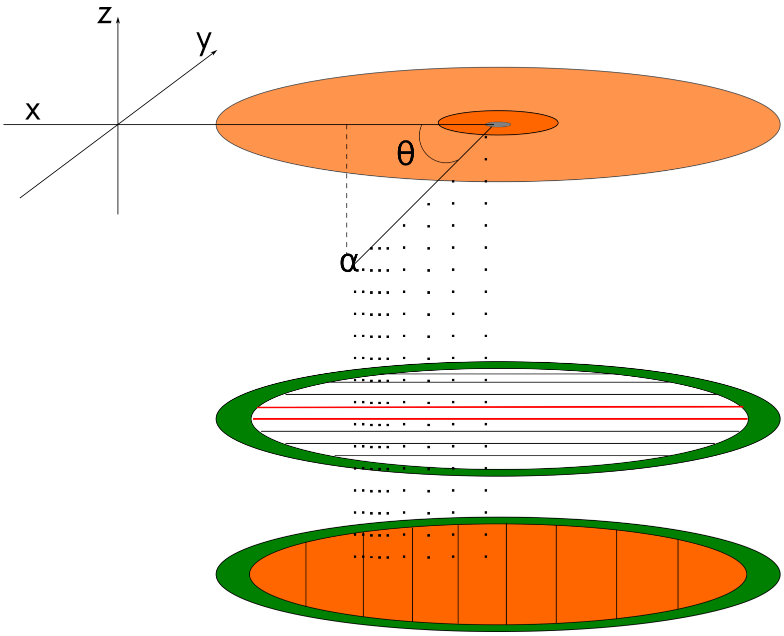

Figure 4.12: An illustration of how segmentation will be implemented. The charge produced by the α particle passes the grid and is detected across multiple segments on the anode. The amplitude of the signal on each segment allows the Bragg curve to be reconstructed. Only the boundaries of the segments on the grid are indicated, not all the wires. In this case the charge passes between the lines highlighted in red. Any signal induced on the wires in this segment can be read out.

Chapter 5

Results

The goal of this work is to find the operating parameters which provide the optimum detection sensitivity for the TIFFIN detector. An iterative and systematic investigation has been carried out to understand the impact of the parameters on the dependent variables, as outlined in Sec. 5.2.

5.1 Radiation Source

To test the detector an ^{241}Am source was used, as it decays via the emission of α-particles:

$$^{241}_{95}\mathrm{Am} \rightarrow ^{237}_{93}\mathrm{Np}^* + \alpha + Q \tag{5.1}$$

It should be noted that although the source can emit α-particles at twenty-five different energies [18], there are only three with an intensity above 1% which dominate the spectrum, these were shown in Fig. 1.7. Table 5.1 lists the relevant α-particle energies and intensities. A second note is that the energy resolution of the detector would have to be less than 45 keV, or 0.8%, in order to distinguish the most prominent energies individually. Without this fine resolution the energies will be detected as one peak. The source is a steel disc with the americium isotope electro-deposited onto one side. It has an activity of approximately 4.9 kBq.

Table 5.1: Major decay energies of α particles emitted by ^{241}Am.

Energy [keV]	Intensity per 100 decays of Parent
5388.00	1.66
5442.80	13.1
5485.56	84.8

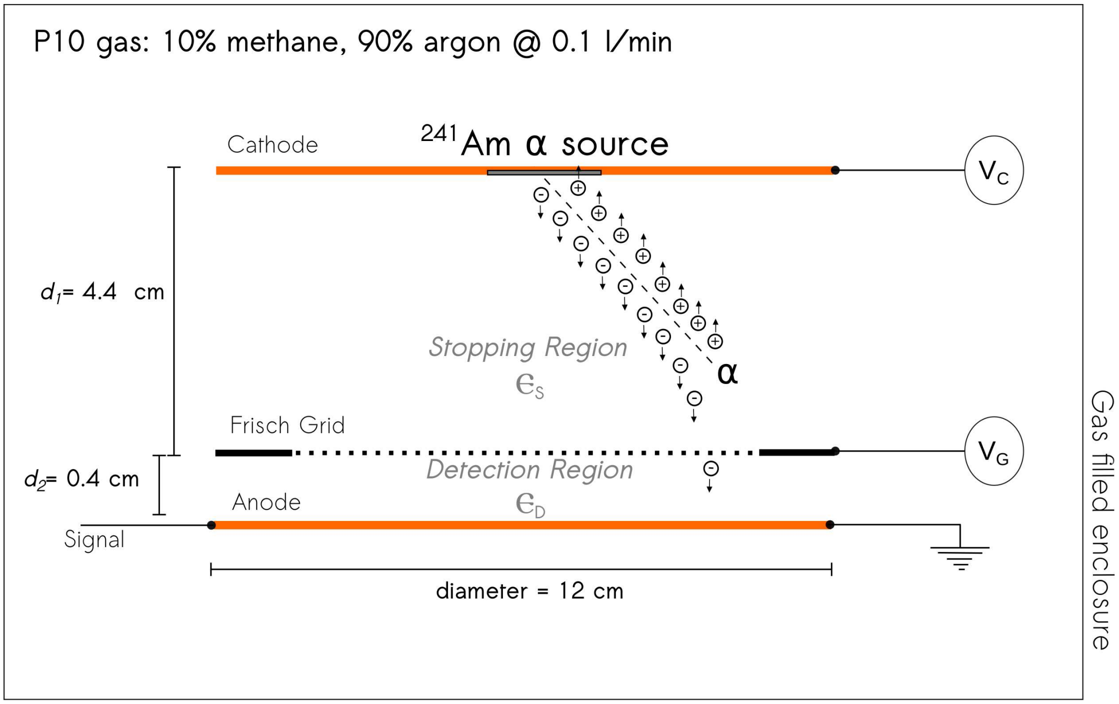

Figure 5.1: A schematic of the set-up of the TIFFIN detector.

5.2 Variables

The parameters which control the operation of the detector that can be changed directly by the user are:

1. Gas pressure,
2. Electric field, which has two components, illustrated in Fig. 5.1
    (a) Stopping region electric field, ϵ_S and
    (b) Detection region electric field, ϵ_D.

Therefore, there is a three dimensional parameter space in which the operation of the detector must be optimized. To understand the effect of these parameters on the detector operation it is convenient to discuss the key variables which depend on them. These variables are:

1. Ratio of the electric fields in the two regions, discussed in Sec. 3.3,
2. Drift velocity of electrons in both electric field regions, discussed in Sec. 2.3.1 and
3. Range of α-particles, discussed in Sec. 2.1.4.

5.3 Detector Preparation

Before taking data, the gas system control devices must be allowed to warm up, to ensure stable operation. Then the detector can be filled to the required gas pressure and allowed to equilibrate. Upon first application of high voltage, contamination of electrode surfaces can cause electrical discharges which are observed as spurious signals. To avoid this, the detector is left to condition under high voltage before use. The conditioning time depends on the level of contamination of the detector plates and has been known to take up to a week.

5.4 Data Analysis

5.4.1 Energy Resolution Evaluation

The optimum operating parameters for the detector are established by monitoring the energy resolution of data collected by the detector. The resolution of the energy spectra collected by the data acquisition system (DAQ) is evaluated with parameters found using a general purpose histogram analysis program called gf3, which is part of the RadWare suite of software [55]. gf3 utilizes a least squares fitting technique for the analysis of one-dimensional spectra. The peaks are fit with a Gaussian function as was shown in Eq. 2.30. The fit parameters may be extracted and used to calculate the energy resolution as explained in Sec. 2.4.

The FWHM as a fraction of the centroid energy of the peak is used to establish the energy resolution of the detector, using Eq. 2.35, which is a dimensionless quantity often expressed as a percentage [24]. Figure 5.2 illustrates the centroid and FWHM for an energy peak. The energy resolution in this case was calculated using Eq. 2.35 to be 12.01(2)%.

5.4.2 Risetime Evaluation

As outlined in Sec. 2.3.1, the drift velocity of the free charge is anticipated to change as ϵ/P is changed. It is not possible in this investigation to measure the drift velocity directly, but the risetime, which is related to the drift velocity, may be observed.

The signal on the anode starts to rise when the first electron passes into the detection region, and in an ideal case reaches its full amplitude when the last electron has been collected. The risetime is the time it takes the signal to rise from zero to 100% of its amplitude. However, this can be hard to determine due to noise, so for evaluation purposes the risetime is defined as the time it takes to get from 10% to 90% of this total amplitude, which provides a more consistent measurement.

The predominant factor affecting the risetime is the drift velocity. If the drift velocity is constant (due to constant electric field and pressure) then the distribution of risetimes observed depends on the track orientation of the radiation within the detector. Those particles emitted perpendicular to the electric field will have shorter risetimes than those emitted parallel thus a

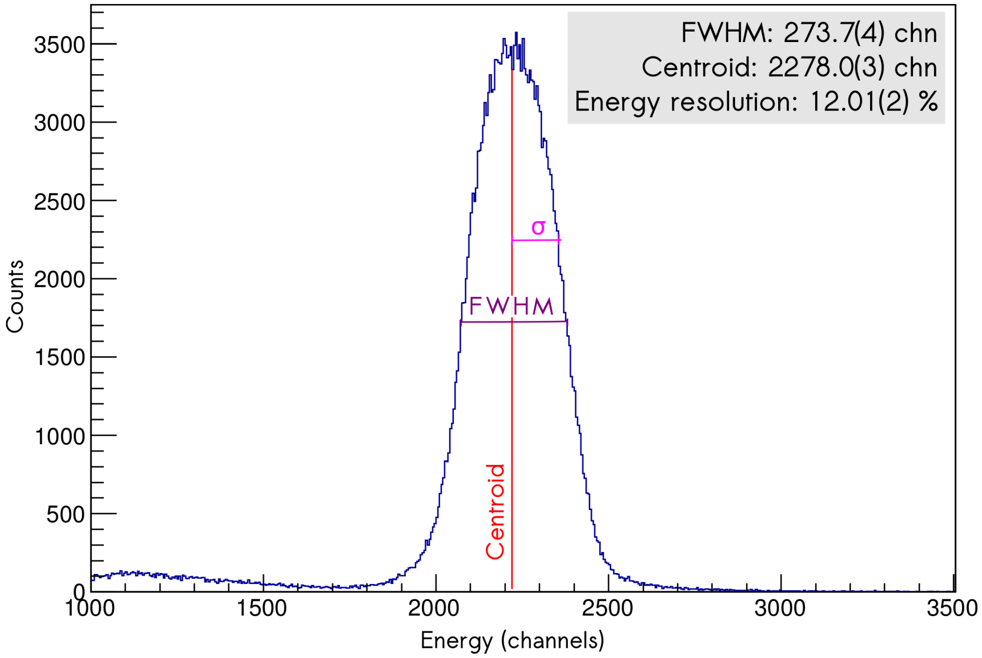

Figure 5.2: An example of the centroid and FWHM for an energy spectrum.

distribution of risetimes dependant on track orientation is seen, this was explained in more detail in Sec. 2.3.3.

Assessment of the risetime of the signal was done by analysing the recorded waveforms on an event-by-event basis. This is illustrated in Fig. 5.3. The first 128 samples of each waveform are averaged to create an estimate of the baseline. To find the maximum of the waveform a low-pass filter is first applied in order to smooth out some of the high frequency noise. Each point in the waveform, n_i, is replaced with an average of the 50 points around it, as shown in Eqn. 5.2 where $N = 50$.

$$n_j = \frac{1}{N+1} \sum_{j=i-N/2}^{i+N/2} n_i \tag{5.2}$$

Next the maximum of the waveform is found by cycling through all the averaged points, evaluating if each point is greater than the largest value. When all values have been tested the maximum is reported. The amplitude is then established as the maximum value with the baseline average subtracted. The time when the signal equals the baseline average plus 10% of the maximum amplitude is referred to as t_{10}, and the corresponding value when the signal equals the baseline average plus 90% of the amplitude is referred to as t_{90}. The risetime is equal to $t_{90} - t_{10}$. Once the risetime has been evaluated for each waveform, the values are plotted as a histogram which is then fit in order to establish the average risetime. The distribution of risetimes is assumed to be Gaussian in character (see Fig. 5.4), so it may be fit in the same way as the energy histograms described above in Sec. 5.4.1. The example shown in Fig. 5.4 has a

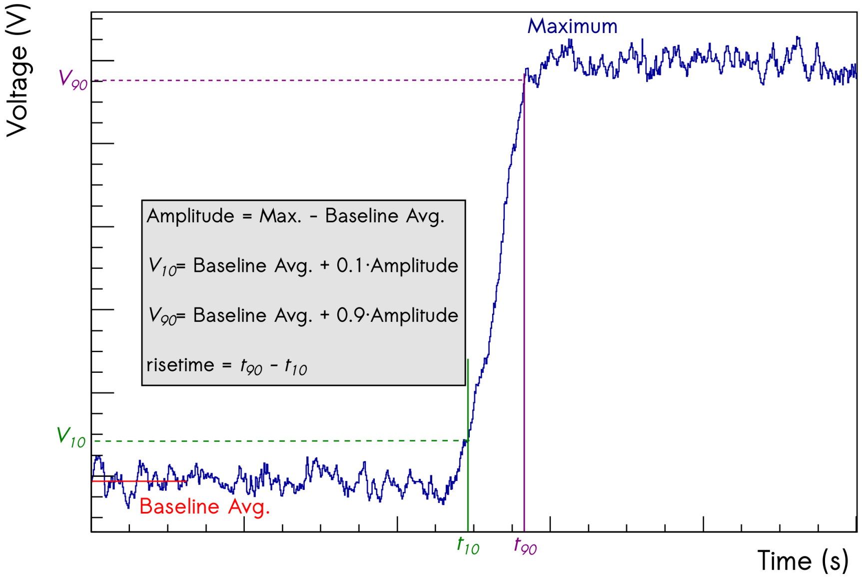

Figure 5.3: An example of how the risetime is assessed for each waveform.

central value of 118 samples with FWHM of 19, which corresponds to an average risetime of 1180 ns and a distribution width of 190 ns.

5.4.3 Risetime-Energy Correlation Evaluation

In Sec. 4.3.1, ballistic deficit was outlined as a consequence of the design of the preamplifier used for this work. It is expected that ballistic deficit will cause a reduction in signal height for signals with a longer risetime due to their increased exposure to the decay effects of the preamplifier, leading to a negative correlation between energy and risetime. A second reason an energy-risetime correlation may arise is incomplete charge collection depending on track orientation. This would predominantly affect those signals with short risetimes from radiation emitted perpendicular to the electric field. These particles create ion pairs near the perimeter of the detector where the field may be less uniform, thereby preventing the full amount of charge from being collected and resulting in a positive correlation between risetime and energy measured. Both of these effects may affect the energy resolution achievable by the detector.

5.5 Settings and Results

The settings outlined in Table 5.2 and Table 5.3 were used to test the detector's response to changing its electric field ratio and the drift velocity of electrons. The field in the detection region was optimized first, and then starting with the settings of the point with the best energy

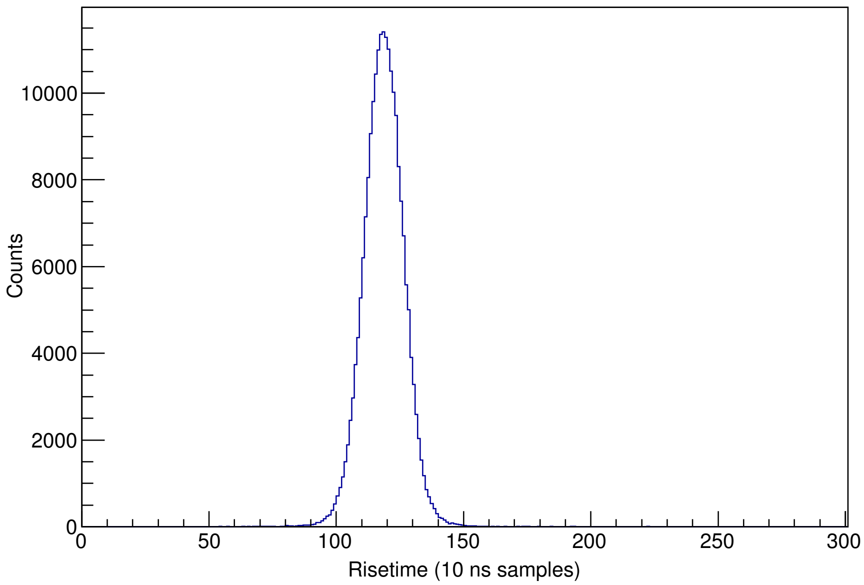

Figure 5.4: An example of the distribution of risetimes for one data run. In this example ϵ_S/P was 0.075 Vcm^{-1}Torr^{-1} and ϵ_D/P was 0.21 Vcm^{-1}Torr^{-1}.

resolution, the field in the stopping region was optimized. Once values for the electric fields were established, the settings in Table 5.4 were used to investigate the effect of changing the range of the α-particles in the detector by varying the gas pressure.

5.5.1 Electric Field Ratio Results

The electric field in the stopping region, ϵ_S, and that in the detection region, ϵ_D, are different, depending on the bias applied to the detector plates. The electric field ratio, R, given by Eqn. 5.3 is manipulated by adjusting the bias applied to the plates.

$$R = \frac{\epsilon_D}{\epsilon_S} \tag{5.3}$$

The electric field between two electrodes is the potential difference between them, ΔV divided by the distance separating them, d. Therefore the values for ϵ_S and ϵ_D are given by Eqn.s 5.4 and 5.5. The bias applied to the cathode is V_C, the bias applied to the Frisch grid is V_G and the bias applied to the anode is V_A. The distances between the cathode and grid and between the grid and anode are d_1 and d_2 respectively as illustrated in Fig. 5.1.

$$\epsilon_D = \frac{V_C - V_G}{d_1} \tag{5.4}$$

$$\epsilon_S = \frac{V_G - V_A}{d_2} \tag{5.5}$$

The anode is at ground so $V_A = 0$ and Eqn. 5.5 can be simplified to $\epsilon_S = \frac{V_G}{d_2}$.

Therefore the ratio may be written in terms of the bias applied as shown in Eqn. 5.6.

$$R = \frac{V_C - V_G}{V_G}\frac{d_2}{d_1} \tag{5.6}$$

Effects due to variation of the ratio of electric fields in the two regions of the detector were investigated by changing one and keeping the other constant to find the optimum response, then maintaining that electric field and changing the field in the other region. The ratio of electric fields between the detector electrodes affects the number of electric field lines that pass the grid compared to the number that end on the grid wires [39] resulting in a loss of electrons to the wires. The recommended ratio, R, indicated by [39] depends entirely on the geometry of the detector. For the geometry of TIFFIN, $R \geqslant 1.6$, with the electric field in the detection region 1.6 times that of the field in the stopping region as implied by Eqn. 5.3.

The energy resolution achieved by the detector as a function of R is shown in Fig. 5.5 and listed in Table 5.3. There is a clear correlation between the energy resolution and the ratio of electric fields. When R is adjusted by changing ϵ_D/P a plateau is reached: above a ratio of approximately 2.7 the energy resolution varies less than 0.5%. However, when R is adjusted by changing ϵ_S/P, a minimum is seen and the energy resolution deteriorates at large R. In both cases the smallest energy resolution occurs at a ratio of 2.8, and so an optimum value of $R = 2.8$ is concluded. This optimum value of R is larger than the predicted value. The Frisch grid was wired by hand and the tension, separation and diameter of the wires may be inconsistent, resulting in a larger experimental value of R. In addition, the criteria outlined in [39] stipulates a uniform electric field which may not be the case in this detector. The correlation between energy resolution and R was expected to plateau in both instances. Changing R by varying ϵ_S/P did not lead to this result due to the resolution being dependant on R for low values of R and dependent on supplementary factors at large values of R. Diffusion of the free charge in the gas increases with decreasing electric field. When $R = 6$, the electric field in the stopping region, $\epsilon_S/P = 0.035$ Vcm^{-1}Torr^{-1}, and diffusion due to the low electric field strength at this point may be causing the diminished energy resolution.

Table 5.2: Settings and results for the variation of R by changing ϵ_D whilst keeping ϵ_S constant. Pressure was maintained at 1600 Torr, which leads to an estimated maximum α-particle range of 2.26 cm [31].

ϵ-field Ratio	ϵ_S/P $[\mathrm{Vcm}^{-1}\mathrm{Torr}^{-1}]$	ϵ_D/P $[\mathrm{Vcm}^{-1}\mathrm{Torr}^{-1}]$	Cathode Voltage [-V]	Frisch Grid Voltage [-V]	Energy			Risetime	
					Centroid [channels]	FWHM [channels]	Resolution [%]	Centroid [10 ns samples]	FWHM [10 ns samples]
1	0.075(3)	0.075(3)	576(2)	48(2)	2093.0(3)	276.6(4)	13.22(2)	112.96(2)	16.60(2)
1.25	0.075(3)	0.094(3)	588(2)	60(2)	2196.7(3)	276.9(5)	12.61(2)	111.98(2)	16.06(2)
1.5	0.075(3)	0.113(3)	600(2)	72(2)	2278.0(3)	273.7(4)	12.01(2)	111.10(1)	15.67(2)
1.75	0.075(3)	0.131(3)	612(2)	84(2)	2338.5(3)	268.8(4)	11.49(2)	110.64(1)	15.30(2)
2	0.075(3)	0.150(3)	624(2)	96(2)	2378.0(3)	262.8(4)	11.05(2)	110.16(1)	15.10(2)
2.4	0.075(3)	0.180(3)	643(2)	115(2)	2415.6(3)	267.9(4)	11.09(2)	109.19(1)	14.92(2)
2.8	0.075(3)	0.209(3)	662(2)	134(2)	2424.2(3)	253.7(4)	10.47(2)	109.61(1)	14.90(2)
3	0.075(3)	0.225(3)	672(2)	144(2)	2423.9(2)	256.6(4)	10.58(2)	109.34(1)	14.89(2)
3.4	0.075(3)	0.255(4)	691(2)	163(2)	2424.1(3)	259.8(3)	10.72(1)	109.36(1)	14.79(1)
3.8	0.075(3)	0.284(4)	710(2)	182(2)	2424.0(3)	261.5(3)	10.79(1)	109.66(1)	14.85(1)
4	0.075(3)	0.300(4)	720(2)	192(2)	2423.9(3)	262.3(3)	10.82(1)	109.62(1)	15.14(1)
5	0.075(3)	0.375(4)	768(2)	240(2)	2423.6(3)	266.1(3)	10.98(1)	110.28(1)	15.17(1)
6	0.075(2)	0.450(4)	816(2)	288(2)	2403.3(3)	266.3(3)	11.08(1)	111.58(1)	16.75(1)

Table 5.3: Settings and results for the variation of R by changing ϵ_S whilst keeping ϵ_D constant. Pressure was maintained at 1600 Torr which leads to an estimated maximum α-particle range of 2.5 cm [31].

			Cathode	Frisch Grid	Energy			Risetime	
ϵ-field	ϵ_S/P	ϵ_D/P	Voltage	Voltage	Centroid	FWHM	Resolution	Centroid	FWHM
Ratio	$\mathrm{Vcm^{-1}Torr^{-1}}$	$\mathrm{Vcm^{-1}Torr^{-1}}$	[-V]	[-V]	[channels]		[%]	[samples]	
1.0	0.210(3)	0.210(3)	1613(3)	134(2)	2211.5(2)	283.0(6)	12.80(3)	76.68(1)	10.21(1)
1.25	0.168(3)	0.210(3)	1317(2)	134(2)	2293.9(2)	284.8(6)	12.42(2)	77.56(1)	10.38(1)
1.5	0.140(2)	0.210(3)	1120(2)	134(2)	2354.9(2)	280.2(5)	11.90(2)	80.62(1)	10.91(1)
1.75	0.120(2)	0.210(2)	979(2)	134(2)	2399.2(2)	273.5(4)	11.40(2)	85.08(1)	11.75(1)
2.0	0.105(2)	0.210(2)	874(2)	134(2)	2426.3(2)	272.1(4)	11.21(2)	90.91(1)	12.81(1)
2.4	0.088(1)	0.210(1)	750(2)	134(2)	2443.1(2)	265.2(3)	10.86(1)	103.04(1)	15.04(1)
2.8	0.075(1)	0.210(1)	662(2)	134(2)	2436.8(2)	263.9(4)	10.83(1)	118.05(1)	17.75(2)
3.0	0.070(1)	0.210(1)	627(2)	134(2)	2433.1(2)	264.5(4)	10.87(1)	125.93(1)	18.50(2)
3.4	0.062(1)	0.210(1)	569(2)	134(2)	2428.5(2)	272.4(4)	11.22(2)	144.01(1)	20.44(2)
3.8	0.055(1)	0.210(1)	523(2)	134(2)	2421.2(2)	275.9(3)	11.40(1)	165.39(2)	25.18(2)
4.0	0.053(1)	0.210(1)	504(2)	134(2)	2415.8(2)	281.3(3)	11.64(1)	175.15(2)	27.32(2)
5.0	0.042(1)	0.210(1)	430(2)	134(2)	2381.2(2)	292.5(4)	12.28(2)	239.93(3)	37.31(4)
6.0	0.035(1)	0.210(1)	381(2)	134(2)	2366.2(2)	280.4(3)	11.85(1)	312.70(4)	51.61(5)

5.5.2 Electron Drift Velocity Results

As mentioned in Sec. 2.3.1, the drift velocity of the electrons depends on both the electric field (ϵ) and the gas pressure (P) inside the detector [56]. The ratio ϵ/P, is therefore varied to change the drift velocity. The drift velocity cannot be directly measured so any change is monitored by examining the risetime of the signals seen. The risetimes from the data sets outlined in Table 5.2 and Table 5.3 were used to investigate the effects of drift velocity.

It was anticipated that the risetime would decrease as the drift velocity was predicted to increase. Figures 5.6 and 5.7 show the change in risetime as ϵ_D/P and ϵ_S/P are changed respectively. Also shown are the calculated drift velocity values from [26], scaled for direct comparison with the risetime. Changing ϵ_D/P was not seen to have a strong impact on the risetime measured. The risetime remains almost constant across the data set even when the calculations indicate the drift velocity is increasing. In comparison, changing ϵ_S/P had a significant impact on the risetime measured, in line with the velocity predictions. It can be concluded that the strength of ϵ_S/P is the dominating factor which decides the risetime and should be manipulated to ensure a desired risetime is achieved which may be beneficial for data acquisition purposes. Changing ϵ_S/P had a more prominent affect on the risetime than changing ϵ_D/P because a larger fraction of the distance travelled by the electrons is incorporated in the stopping region, thus changes to the electrons drift velocity in the stopping region has a greater impact on the risetime.

5.5.3 Alpha Range Results

Changing the gas pressure whilst maintaining the same value of ϵ/P in the detector changes the range of the α-particles without changing the drift velocity of the free charge. The detection range of α-particles in TIFFIN has a hard limit defined by the inner radius of the Frisch grid, which is 4.5 cm and the distance from the cathode to the grid, which is 4.4 cm. If the range of the α-particles is greater than this radius then incomplete charge collection becomes an issue for those alphas emitted perpendicular to the electric field, as they will travel further than the grid radius, and therefore the electrons produced in the gas will not be collected as they drift in the direction of the anode. If the range of the α-particles is greater than the cathode-to-grid distance, α-particles travelling parallel to the electric field may not stop before reaching the grid, resulting in a reduced signal height and a greater spread on the energy distribution measured. The pressure settings chosen should ensure that the α-particles do not reach these limits. According to [31], the maximum range of 5.5 MeV α-particles in P10 gas at a pressure of 900 Torr is 4.0(2) cm, and 4.6(2) cm at 800 Torr. The cathode and grid have a separation of 4.4 cm. Therefore the pressure should not be much lower than 900 Torr.

After investigating the effects of the electric field in the previous sections, an electric field ratio, ϵ_D/ϵ_S of 2.8 was chosen and maintained whilst pressure was optimized. The settings outlined in Table 5.4 were used to evaluate the effect of pressure on the detector's energy resolution.

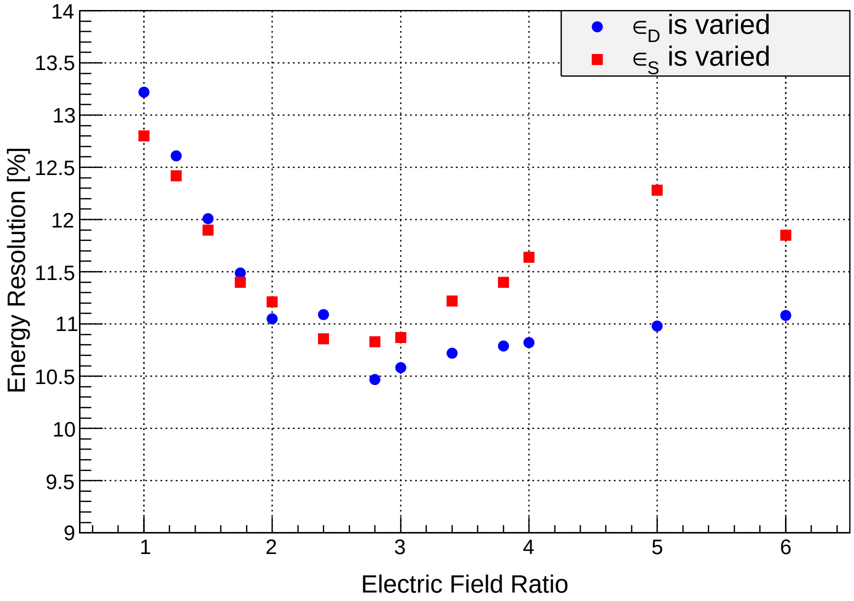

Figure 5.5: The effect on the energy resolution achieved by the TIFFIN detector as the ratio of electric fields in the detector are varied. ϵ_S/P was held constant at 0.075 $\mathrm{Vcm^{-1}Torr^{-1}}$when ϵ_D/P was varied and ϵ_D/P was held constant at 0.21 $\mathrm{Vcm^{-1}Torr^{-1}}$ when ϵ_S/P was varied. The error bars are smaller than the points on the graph. This data was taken at non-optimum pressure.

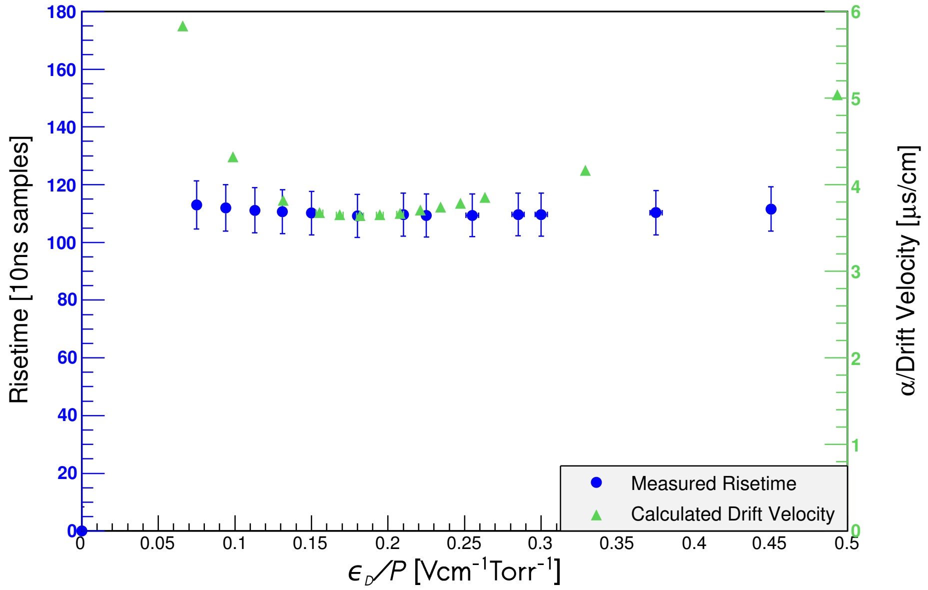

Figure 5.6: On the left axis (blue), the signal risetime seen by the TIFFIN detector as ϵ_D changes, is shown. On the right axis (green), the simulated α/drift velocity is shown for the same electric field range [26]. This data was taken at non-optimum pressure. The error bars are smaller than the points, where not visible.

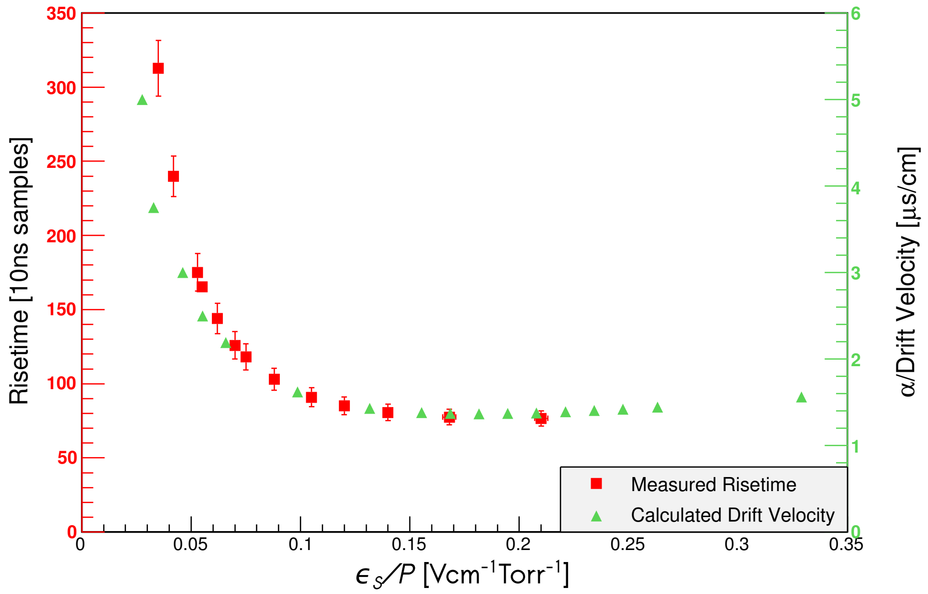

Figure 5.7: On the left axis (red), the signal risetime seen by the TIFFIN detector as ϵ_S changes, is shown. On the right axis (green), the simulated α/drift velocity is shown for the same electric field range [26]. This data was taken at non optimum pressure. The error bars are smaller than the points, where not visible.

Table 5.4: Settings and results for the variation of pressure in the detector chamber whilst maintaining the ϵ_S/P of 0.075 Vcm^{-1}Torr^{-1} and ϵ_D/P of 0.21 Vcm^{-1}Torr^{-1}. The electric field ratio, R is 2.8. The range was estimated using SRIM [31].

				Energy			Risetime	
Pressure Torr]	Maximum Range [cm]	Cathode Voltage [-V]	Frisch Grid Voltage [-V]	Centroid [channels]	FWHM [channels]	Resolution [%]	Centroid [samples]	FWHM [samples]
1800 (9)	2.01(9)	745(2)	151(2)	2422.7(1)	214.6(3)	8.69(1)	107.33(1)	12.48(1)
1700 (9)	2.1(1)	704(2)	143(2)	2415.5(2)	223.3(3)	9.30(1)	107.02(1)	12.59(1)
1600 (8)	2.3(1)	662(2)	134(2)	2409.0(2)	240.8(3)	9.94(1)	106.52(1)	12.64(1)
1500 (8)	2.4(1)	621(2)	126(2)	2393.4(2)	254.0(3)	10.70(1)	106.17(1)	12.70(1)
1400 (7)	2.6(1)	580(2)	118(2)	2381.1(2)	273.2(4)	11.33(1)	105.86(1)	12.79(1)
1300 (7)	2.8(1)	538(2)	109(2)	2362.8(2)	294.4(4)	12.38(1)	105.68(1)	12.95(1)
1200 (6)	3.0(1)	497(2)	101(2)	2348.8(2)	327.1(4)	13.66(2)	105.31(1)	13.84(1)
1100 (6)	3.3(1)	455(2)	92(2)	2326.9(2)	363.5(5)	15.45(2)	103.61(1)	13.69(1)
1000 (5)	3.6(2)	414(2)	84 (2)	2295.2(2)	426.3(9)	18.23(4)	102.52(1)	13.73(1)
900(5)	4.0(2)	373(2)	76 (2)	2256.9(2)	483.5(9)	21.77(4)	101.84(1)	13.85(1)

Figure 5.8 shows the relationship between pressure and energy resolution. The α-particle range which was predicted with the SRIM software [31] is also shown for comparison. The energy resolution is clearly reduced as pressure increases. From this it may be concluded that the detector should be run at as high a pressure as possible to achieve the best energy resolution.

At low pressure, the range of the particle gets longer and so the α-particles are closer to the edge of the detector when they stop. The detector has nothing to maintain the linearity of the electric field lines between the plates. The anode and the chamber are both at the same ground potential. Therefore it is likely that the electric field lines may be curved outwards towards the chamber walls, which would affect the path of the electrons. These so-called "fringe effects" could lead to incomplete charge collection which would result in a greater spread in detected energies and result in poor energy resolution. The resolution as a function of range is plotted in Fig. 5.9.

It is expected that the energy resolution achievable by increasing the pressure should plateau at some point, when the range of the α-particle is such that the electrons produced are confined to a central region in the detector where fringe effects have no impact. However, this investigation has been limited by what pressure the instruments and fittings can withstand. The limit for the gas flow control system is 2000 Torr [48] [49]. However the fittings used in the system are not rated to above atmospheric pressure. When running the system it was possible to monitor the pressure using the online interface of the πPC, and at 1800 Torr the system struggled to maintain the pressure so it was therefore deemed a good place to stop.

Figure 5.10 shows that changing the pressure to change the range of the α-particles in the detector has little effect on the risetime, although as the pressure is directly related to the drift velocity. This is contrary to expectations. As previously stated, the shortest risetimes correspond to the α-particles emitted perpendicular to the electric field. These are ones that would be most affected by fringe effects as they travel close to the detector edge. It is possible that the short risetimes are therefore not seen due to electron loss and the average risetime is thus artificially higher. In conclusion, a field cage should be installed in order to maintain a uniform field in the detector. With a uniform field the risetime ought to vary with pressure and the energy resolution should plateau.

5.5.4 Electric Field Magnitude

Once the effects of electric field ratio, electron drift velocity and α particle range had been tested it was found that high pressure results in better energy resolution and an electric field ratio of 2.8 was optimal for the TIFFIN detector in its current configuration. Further measurements were taken in order to establish if the particular electric fields selected previously to achieve $R = 2.8$ were optimum, or if any fields at a ratio of 2.8, could be used and still achieve the same energy resolution.

The settings and results for changing the electric field magnitude are tabulated in Table 5.5 and Table 5.6.

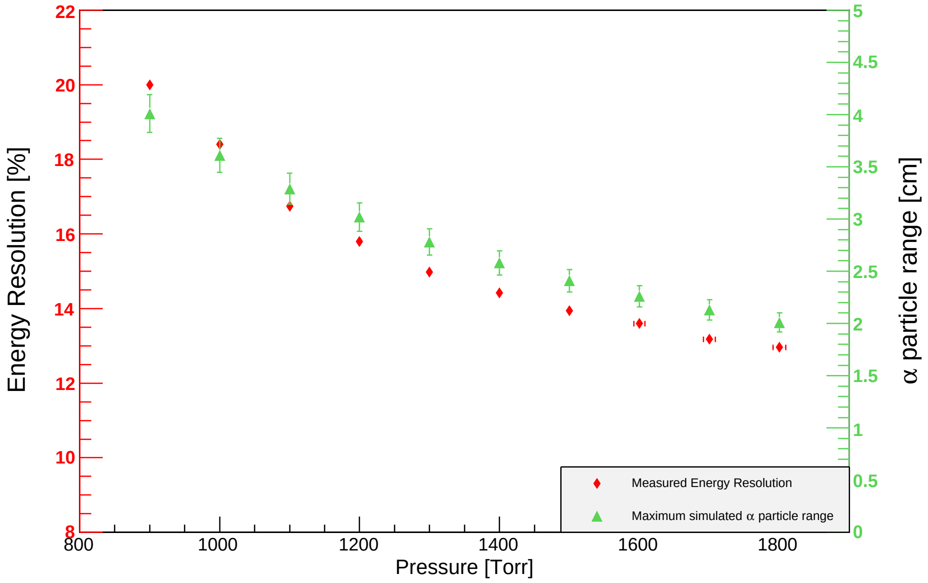

Figure 5.8: The effect on the energy resolution achieved by the TIFFIN detector as the pressure of P10 gas in the detector is varied is shown. $R = 2.8$ with $\epsilon_S/P = 0.075$ Vcm^{-1}Torr^{-1} and $\epsilon_D/P = 0.21$ Vcm^{-1}Torr^{-1}. The resolution error bars are smaller than the points on the graph. For comparison, the calculated range of the α-particles in P10 gas for the pressures measured is shown in green. Values for the range were calculated using the software package, SRIM [31].

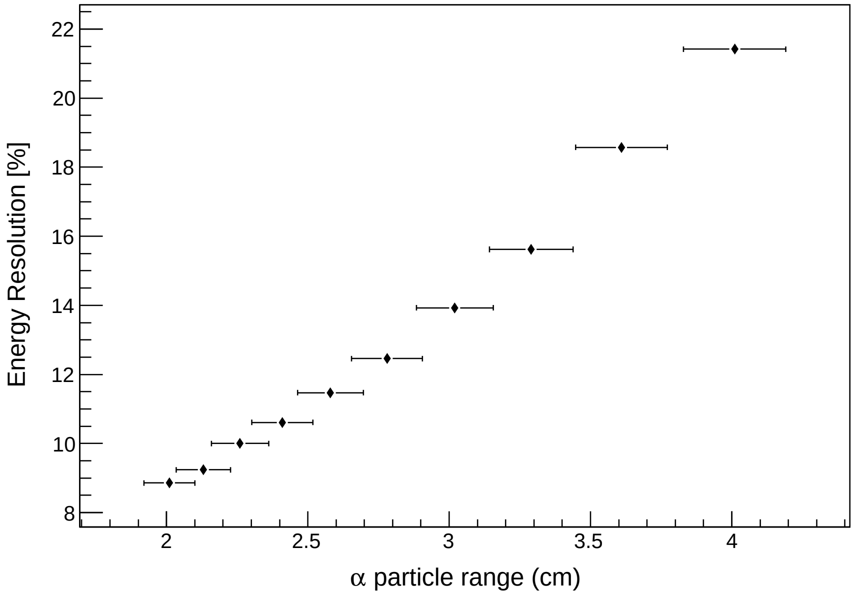

Figure 5.9: The effect on energy resolution is plotted as a function of α-particle range, which changes when the gas pressure in the detector is changed, as shown in Fig. 5.8. Values for the range were calculated using the software package, SRIM [31].

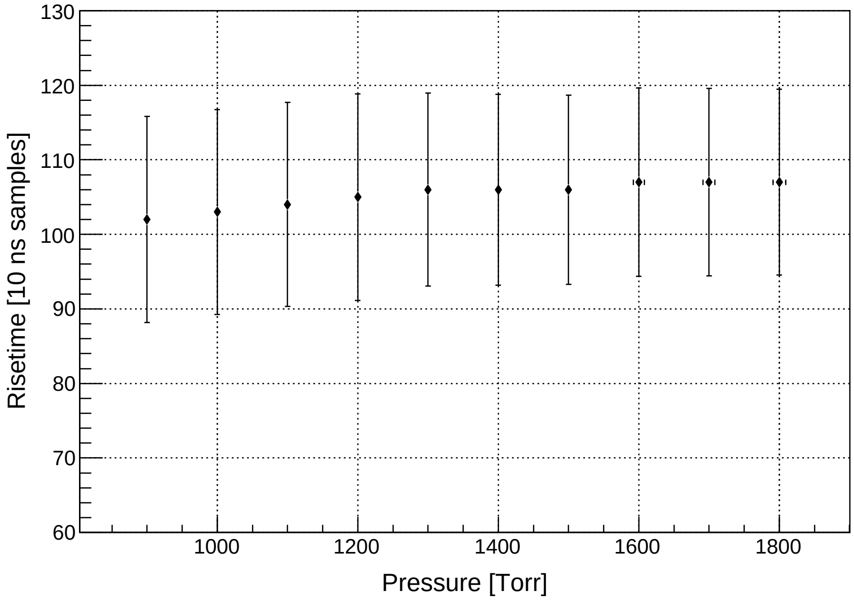

Figure 5.10: The effect on the risetime seen by the TIFFIN detector as the pressure of P10 gas in the detector is varied. ϵ/P is kept constant so that the drift velocity does not change; only the range of the α-particle is changing. Note that the error bars represent the distribution of measured risetimes, not the error on the risetime measurement itself.

Figure 5.11 shows that changing the magnitude of the electric field has no clear effect on the energy resolution achievable by the detector beyond what has already been established at this point. Figure 5.12 covers a wider range of drift velocities in the stopping region than has been observed thus far in this investigation. Previously the maximum value of ϵ_S/P was 0.21 Vcm^{-1}Torr^{-1} and ϵ_D/P reached 0.45 Vcm^{-1}Torr^{-1}, whereas here ϵ_S/P and ϵ_D/P reach 0.375 Vcm^{-1}Torr^{-1} and 1.05 Vcm^{-1}Torr^{-1} respectively. Despite this wide range of drift velocities investigated, the resolution does not change significantly, leading to the suggestion that the drift velocity of electrons is not a limiting factor in this range. The risetime results are plotted in Fig. 5.12 with ϵ_S/P on the x-axis as previous results have shown that the field in this region has more effect on the results than the field in the detection region. The scaled reciprocal of the predicted drift velocities has also been plotted for comparison.

Table 5.5: Electric field magnitude settings. Data taken at a pressure of 1750 Torr, which corresponds to a maximum α-particle range of 2.1(1) cm. See Table 5.6 for results.

ϵ-field Ratio	Stopping Region ϵ_S/P [V/cm/Torr]	Detection Region ϵ_D/P [V/cm/Torr]	Cathode Voltage [-V]	Frisch Grid Voltage [-V]
2.8	0.075(1)	0.210(1)	725(2)	147(2)
2.8	0.150(1)	0.420(1)	1449 (3)	294(2)
2.8	0.225(2)	0.630(2)	2174 (3)	441(2)
2.8	0.300(2)	0.840(2)	2898 (3)	588(2)
2.8	0.375(2)	1.050(3)	3623 (4)	735(2)

Table 5.6: Electric field magnitude results. Data taken at a pressure of 1750 Torr, which corresponds to a maximum α-particle range of 2.1(1) cm. See Table 5.5 for settings.

	Energy			Risetime	
Ratio	Centroid [channels]	FWHM [channels]	Resolution [%]	Centroid [samples]	FWHM [samples]
2.8	2458.5(3)	244.2(7)	9.93(3)	108.52(1)	15.24(2)
2.8	2485.7(3)	243.5(4)	9.80(2)	78.16(1)	9.76(1)
2.8	2493.0(3)	247.0(5)	9.91(2)	78.59(1)	9.85(1)
2.8	2495.3(3)	257.6(6)	10.32(2)	83.69(1)	10.70(1)
2.8	2476.5(3)	265.8(6)	10.73(2)	89.32(1)	11.74(2)

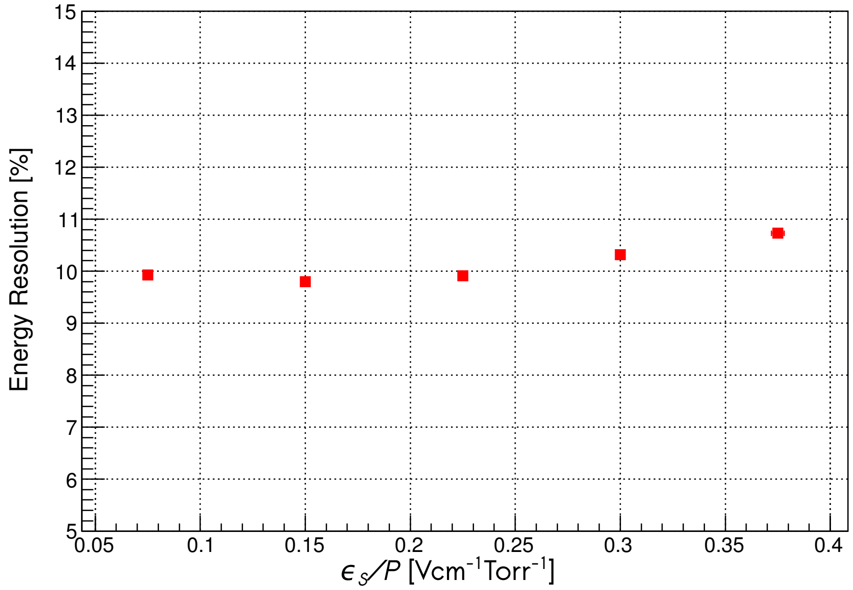

Figure 5.11: The resolution as a function of ϵ_S/P is plotted, showing the effect of increasing the magnitude of ϵ/P at a ratio $\epsilon_D/\epsilon_S = 2.8$. The error bars are smaller than the points on the graph. This data was taken at optimum pressure.

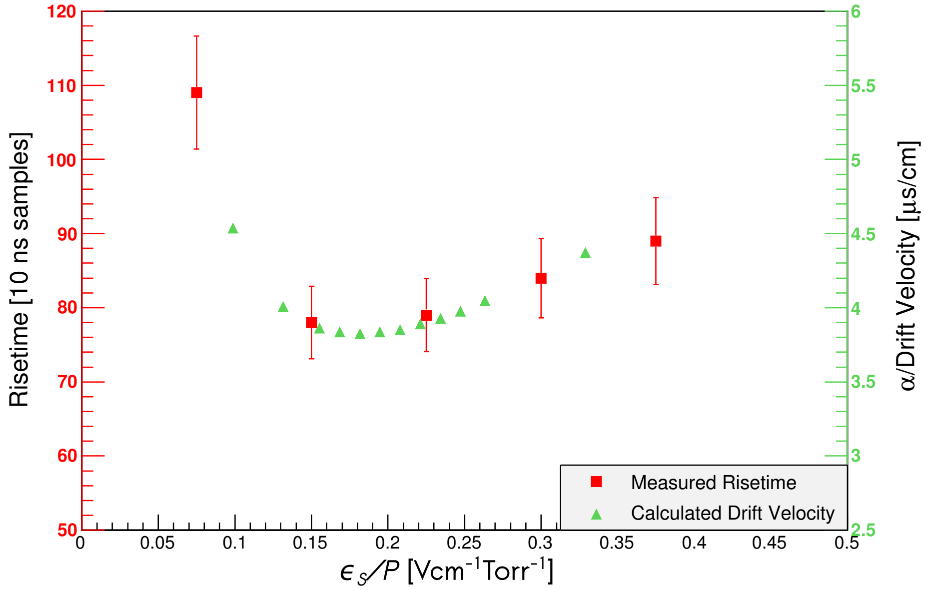

Figure 5.12: The risetime as a function of ϵ_S/P is plotted, showing the effect of increasing the magnitude of both ϵ_S/P and ϵ_D/P at a constant ratio of 2.8. This data was taken at optimum pressure.

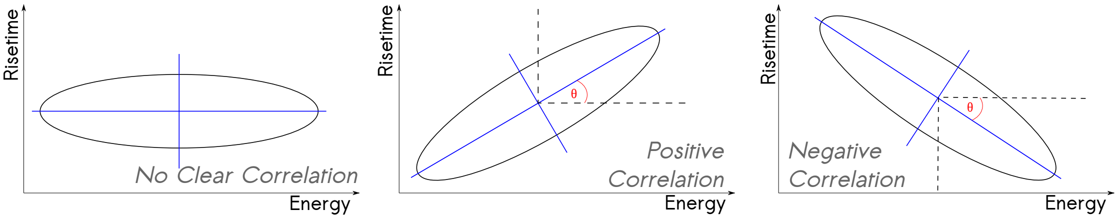

Figure 5.13: The difference in two dimensional spectra of energy against risetime if there is no clear correlation between energy and risetime (left), there is positive correlation (centre), or there is negative correlation (right).

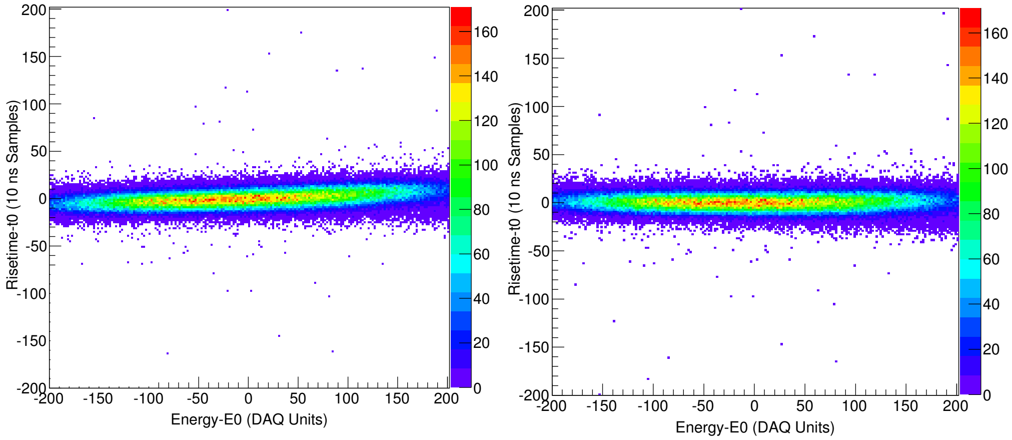

Figure 5.14: Left: the 2D spectrum before rotational correction. The data has been centred at the origin. Right: 2D spectrum after rotational correction.

5.5.5 Risetime - Energy Correlation Results

In Sec. 5.4.3 the two reasons a risetime energy correlation might be seen were outlined. These were: ballistic deficit, which would manifest as a negative correlation between energy and risetime, and incomplete charge collection, which would manifest as a positive correlation. These scenarios and the event of no correlation between energy and risetime are shown in Fig. 5.13.

In order to establish the existence and degree of correlation, two dimensional spectra of energy against risetime were generated as shown in Fig. 5.14. The spectrum on the left is the raw data, which show a slightly positive correlation, which, as previously explained, could be due to incomplete charge collection. The magnitude of the correlation may be estimated by rotating the data points until the distribution lies parallel to the energy axis. The resulting rotated spectrum is shown on the right of Fig. 5.14.

Before the points could be rotated they were first centred. The energy and risetime distributions were centred at zero by subtracting the average value of their respective distributions from each point. Using the rotation matrix shown in Eqn. 5.7, each point in the distribution was rotated through an angle θ. In this equation, E_{rot} and t_{rot} are the rotated energy and risetime

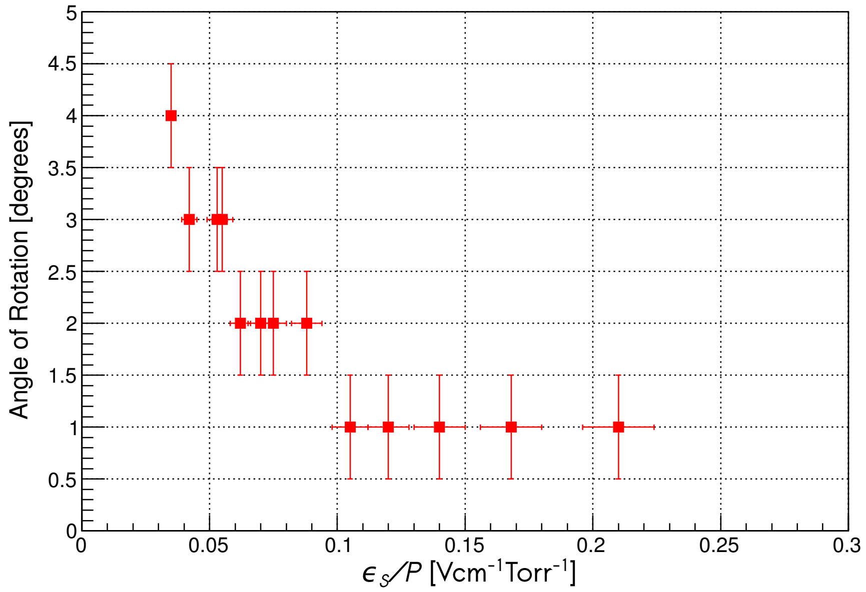

Figure 5.15: The angle of rotation required to remove any correlation between energy and risetime, plotted against ϵ_S/P. ϵ_D/P was held constant at 0.21 Vcm^{-1}Torr^{-1} and pressure was maintained at 1600 Torr (non-optimal pressure). See Table 5.3 for details on the settings.

values respectively, θ is the angle input by the user, and E and t are the un-rotated energy and risetime values.

$$\begin{pmatrix} E_{\text{rot}} \\ t_{\text{rot}} \end{pmatrix} = \begin{pmatrix} \cos\theta & -\sin\theta \\ \sin\theta & \cos\theta \end{pmatrix} \begin{pmatrix} E \\ t \end{pmatrix} \tag{5.7}$$

This method of rotation was applied to all data taken. Most data required little to no rotation (less than 1°), thus demonstrating an insignificant correlation between energy and risetime. The correlation between energy and risetime was found to increase with decreasing ϵ_S/P as shown in Fig. 5.15. At very low ϵ_S/P, the angle of rotation, θ, required was 4°. By rotating the data, the correlation can be corrected for. With this correction applied the energy spectrum can be compared to the un-corrected spectrum; Fig. 5.16 clearly shows that it does not make a significant difference, and as such the energy may be treated as an independent variable, validating the one-dimensional analysis outlined in Sec. 5.4.1.

Ballistic deficit and incomplete charge collection result in opposite correlations. As the energy resolution is significantly worse than the theoretical resolution it may be hypothesized that both effects are impacting the results, but cancelling out the effect manifested as an angular correlation whilst still degrading the resolution.

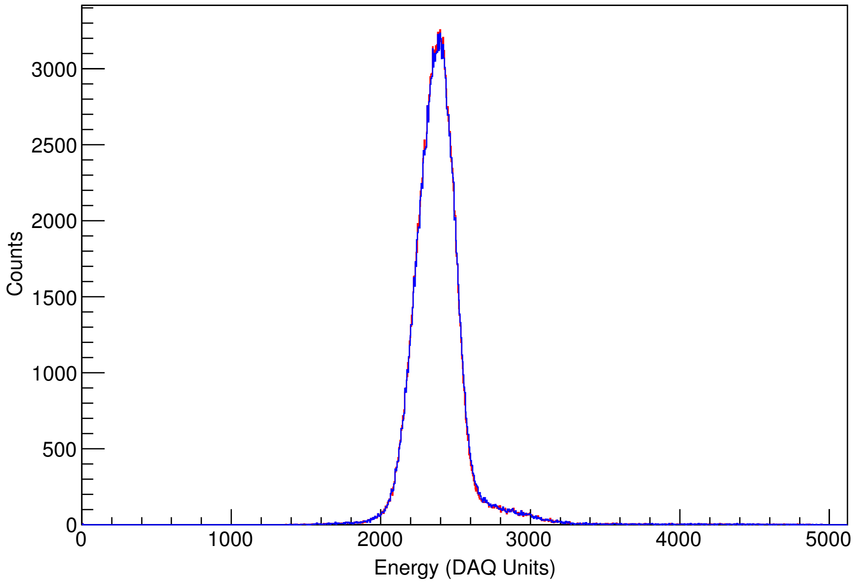

Figure 5.16: The angular dependence is seen most strongly at high electric field ratio, see Fig. 5.15. This spectrum has been corrected for its angular dependence (blue) and overlaid on the un-corrected spectrum (red). The correction does not significantly change the spectrum.

5.6 Reversed Orientation Test

It was suspected that a significant factor in limiting the energy resolution was incomplete charge collection due to inconsistencies in the electric field in the non-central regions of the detector. In order to test this theory, the detector orientation and biasing were changed so that there is a potential difference between the anode and the chamber walls. The field lines should therefore curve preferentially inwards, ensuring more complete electron collection. The detector orientation was reversed from what is shown in Fig. 5.17 to Fig. 5.18, so that the plate holding the source is now the closest plate to the base of the chamber and is grounded. The signal is taken from the anode, which is now located close to the center of the chamber. The anode is positively biased, as is the Frisch grid, and signals can be taken from both the Frisch grid and the anode. The operating parameters are listed in Table 5.7 with the previous best for comparison.

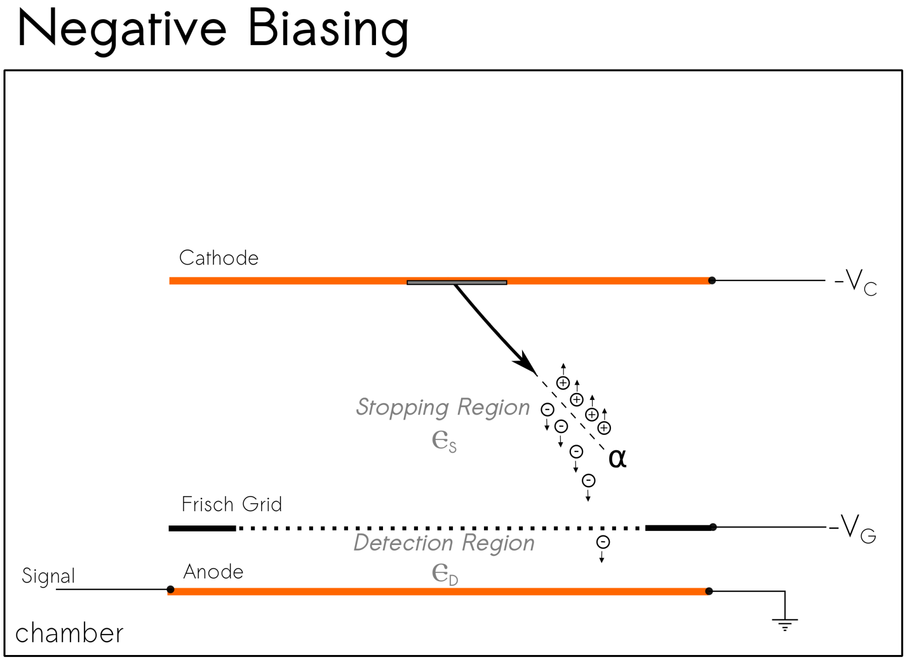

Figure 5.17: The schematic of the detector as it was used for the main body of work in this thesis.

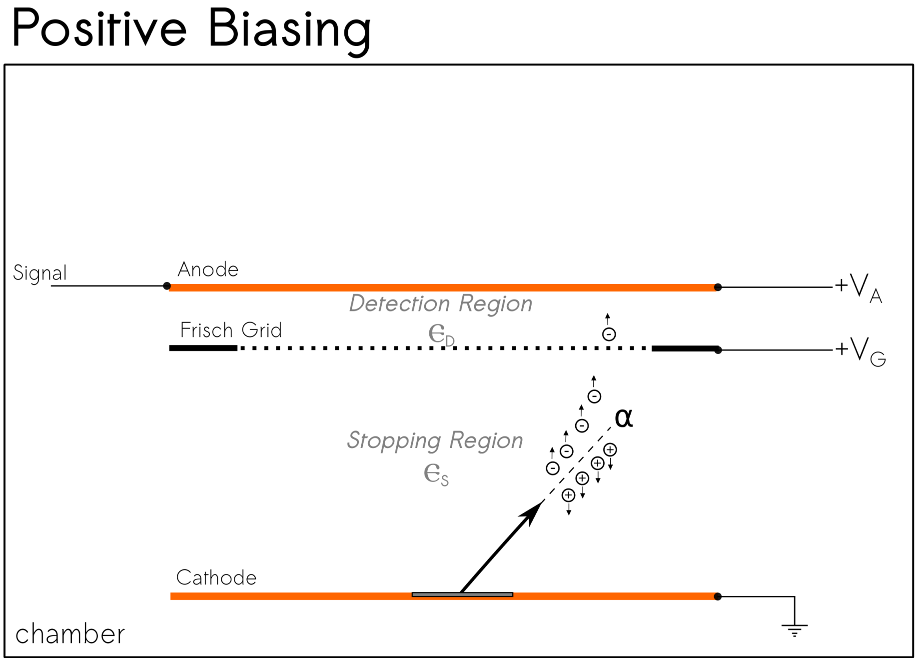

Figure 5.18: The schematic of the detector after reversing the orientation and changing the biasing scheme.

Table 5.7: Settings and results for the two orientations.

				Cathode Voltage [V]	Frisch Grid Voltage [V]	Anode Voltage [V]	Energy		
Orientation	ϵ-field Ratio	ϵ_S/P [$\mathrm{Vcm^{-1}Torr^{-1}}$]	ϵ_S/P [$\mathrm{Vcm^{-1}Torr^{-1}}$]				Centroid [channels]	FWHM	Resolution [%]
Old	2.8	0.075	0.21	-745	-151	0	2422.71(15)	214.6(3)	8.69(1)
New	2.8	0.075	0.21	0	+578	+798	3133.82(13)	107.68(19)	3.44(1)

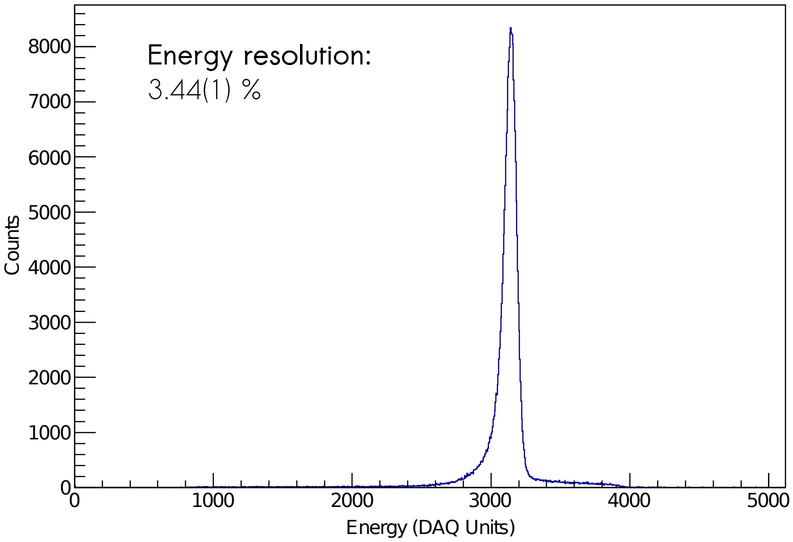

Figure 5.19: Energy spectrum taken after changing the detector orientation and biasing scheme. The energy resolution is 3.44(1)%.

The energy resolution was improved to 3.44(1)% (see Fig. 5.19), at 1750 Torr and an electric field ratio of 2.8 with ϵ_S/P at 0.075 Vcm^{-1}Torr^{-1} and ϵ_D/P at 0.21 Vcm^{-1}Torr^{-1}. The pressure used here was slightly lower, at 1750 Torr, than that used for the previous best measurement, as it was felt that the instruments were struggling to maintain the higher pressure of 1800 Torr. An ideal next step for improvement would be to install an electric field cage. A field cage may take the form of a series of metal rings, installed between the cathode and the Frisch grid. These rings would have an intermediary bias applied, such that the electric field gradient between the electrodes is controlled. This would encourage straight field lines in the whole volume between the detector plates as opposed to curved field lines (either towards the collecting plate or away from it). Although the energy resolution has been improved, curved field lines of any sort may affect the timing response of the detector, which would be detrimental to future work involving Bragg curve spectroscopy.

The distribution of risetimes seen with this test set-up is shown in Fig. 5.20. The shape of this distribution is significantly different to what has been seen previously and it is unknown whether or not this is an improvement without further investigation.

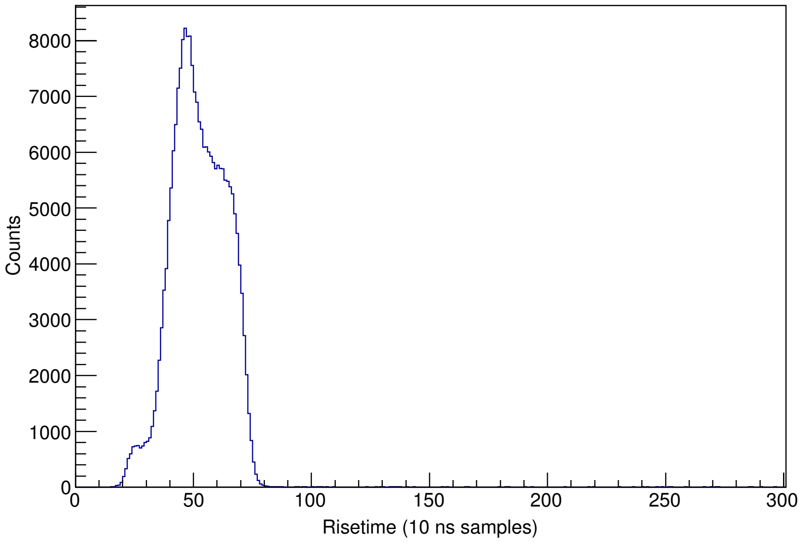

Figure 5.20: Distribution of risetimes taken after changing detector orientation and biasing scheme.

Chapter 6

Conclusions

The Nuclear Science Laboratories at Simon Fraser University are embarking upon a research program with an overall goal of providing experimental information on the origin, production, composition and structure of exotic, neutron-rich isotopes that are of great interest to nuclear science. The properties of these isotopes will be explored by detecting fragments produced from a spontaneous fission source using the Twin Ionization chamber for Fission Fragment Investigation (TIFFIN), which is currently under development at SFU.

The detector is being developed in stages. The first stage prototype of the TIFFIN detector - a single-sided, parallel plate detector with a Frisch grid and digital readout, which allows the analysis of signals on an event-by-event basis - has been completed. It has been tested using an α source in order to characterize its response in terms of energy resolution as a function of detector bias and gas pressure, and to establish where improvements can be made.

The best energy resolution achieved with the TIFFIN detector during this work was 8.69(1)%. This occurred when the detector was run at a gas pressure of 1800 Torr and the detector's electric fields were at a ratio of 2.8 with ϵ_S/P at 0.075 Vcm^{-1}Torr^{-1} and ϵ_D/P at 0.21 Vcm^{-1}Torr^{-1}. In order to be used effectively for fission spectroscopy, the detector must have an energy resolution of 1% or better, so further improvements are necessary.

The statistical limit on energy resolution for this detector is 0.23%. It is suspected that a significant factor limiting the energy resolution possible is incomplete charge collection due to inconsistencies in the electric field in the non-central regions of the detector. The way the detector was biased for this work meant that the collection plate (the anode) was at the same potential as the walls of the chamber, which means the electric field lines will curve out towards the chamber walls. Changing the detector orientation and biasing so that the field lines curve inwards should therefore lead to an improvement in energy resolution due to improved charge collection. When this theory was tested, the energy resolution was improved to 3.44(1)%, at 1750 Torr and an electric field ratio of 2.8 with ϵ_S/P at 0.075 Vcm^{-1}Torr^{-1} and ϵ_D/P at 0.21 Vcm^{-1}Torr^{-1}. However, the field lines are likely still curved, which is not optimal for timing characteristics. Therefore a field cage is necessary in order to take precise risetime measurements.

Bibliography

[1] TRIUMF. TRIUMF: Canada's National Laboratory for Particle and Nuclear Physics, www.triumf.ca. Accessed: 2011. 1

[2] C.E. Svensson, R.A.E. Austin, G.C. Ball, P. Finlay, P.E. Garrett, G.F. Grinyer, G.S. Hackman, C.J. Osborne, F. Sarazin, H.C. Scraggs, M.B. Smith, and J.C. Waddington. Radioactive beam experiments with large gamma-ray detector arrays. *Nuclear Instruments and Methods in Physics Research Section B: Beam Interactions with Materials and Atoms*, 204:660–665, May 2003. xiii, 1, 14, 16

[3] S.S.M. Wong. *Introductory Nuclear Physics*. John Wiley & Sons, Inc., second edition, 1998. x, xii, 1, 4, 5, 11

[4] K.S. Krane. *Introductory Nuclear Physics*. John Wiley & Sons, Inc., 1988. 2, 7, 13

[5] G. Audi, O. Bersillon, J. Blachot, and A.H. Wapstra. The NUBASE evaluation of nuclear and decay properties. *Nuclear Physics A*, 2003. xii, 6

[6] E.M. Henley and A. Garcia. *Subatomic Physics*. World Scientific Publishing, third edit edition, 2007. 8, 9

[7] C.J. Pearson, B.J. Varley, W.R. Phillips, and J.L. Durell. A spectrometer for prompt mass identification of fragments from low-energy fission. *Review of Scientific Instruments*, 66(5):3367, 1995. xii, 8

[8] F. Tovesson, C. Arnold, R. Blakeley, A. Hecht, A. Laptev, D. Mader, K. Meierbachtol, L. Snyder, and M. White. SPIDER: A new instrument for fission fragment research at the Los Alamos Neutron Science Center. *EPJ Web of Conferences*, 62:05002, December 2013. 9

[9] I. Ahmad and W.R. Phillips. Gamma rays from fission fragments. *Reports on Progress in Physics*, 1415, 1995. 9

[10] W. Urban, W.R. Phillips, N. Schulz, B.J.P. Gall, I. Ahmad, M. Bentaleb, J.L. Durell, M.A. Jones, M.J. Leddy, E. Lubkiewicz, L.R. Morss, A.G. Smith, and B.J. Varley. Excited states in 139Te and the properties of r-process nuclei with Z 50 and N 86. *Physical Review C*, 62:4–8, 2000. 10

[11] T. Rzca-Urban, M. Czerwiski, W. Urban, A.G. Smith, I. Ahmad, F. Nowacki, and K. Sieja. First observation of excited states in 87Se: Collectivity and j1 anomaly at N=53. *Physical Review C*, 88(3):034302, September 2013. 10

[12] J.K. Hwang, A.V. Ramayya, J.H. Hamilton, E.F. Jones, P.M. Gore, S.J. Zhu, C.J. Beyer, J. Kormicki, X.Q. Zhang, L.K. Peker, B.R.S Babu, T.N. Ginter, Y.T. Oganessian, A.V. Daniel, W.C. Ma, P.G. Varmette, J.O. Rasmussen, I.Y. Lee, J.D. Cole, R. Aryaeinejad,

M.W. Drigert, M.A. Stoyer, S.G. Prussin, R. Donangelo, and H.C. Griffin. Possible octupole correlation in 147Pr and pi-h(11/2) bands in 149,151Pr. *Physical Review C*, 62:1–5, 2000. 10

[13] Y.X. Luo, J.H. Hamilton, J.O. Rasmussen, A.V. Ramayya, C. Goodin, S.J. Zhu, J.K. Hwang, K. Li, D. Fong, I. Stefanescu, I.Y. Lee, G.M. Ter-Akopian, A.V. Daniel, M.A. Stoyer, R. Donangelo, W.C. Ma, and J.D. Cole. New level schemes and octupole correlations of light neutron-rich lanthanum isotopes 143, 144La. *Nuclear Physics A*, 818(3-4):121–138, March 2009. 10

[14] J.K. Hwang, A.V. Ramayya, and J. Gilat. Rotational bands in 101103Nb and 98, 100Y nuclei and identification of yrast bands in 146La and 149Pr. *Physical Review C*, 58(6):3252–3259, 1998. 10

[15] M. Wang, G. Audi, and A.H. Wapstra. The Ame2012 atomic mass evaluation - II. *Chinese Physics C*, 36(12):1603–2014, 2012. x, 11

[16] C.J. Gallagher and J.O. Rasmussen. Alpha-decay hindrance-factor calculations. *Journal of Inorganic and Nuclear Chemistry*, 3(6):333–344, January 1957. xii, 13

[17] K.P. Santhosh, S. Sahadevan, and J.G. Joseph. Alpha decay of eveneven nuclei in the region to the ground state and excited states of daughter nuclei. *Nuclear Physics A*, 850(1):34–52, January 2011. 12, 14

[18] M.S. Basunia. National Nuclear Data Center, Nuclear Data Sheets 107, 3323, 2006. xiii, 13, 15, 62

[19] K. Siegbahn. *Alpha-, beta- and gamma-ray spectroscopy.* North-Holland Pub. Co., 1965. 14

[20] E. García-Toraño. Current status of alpha-particle spectrometry. *Applied radiation and isotopes : including data, instrumentation and methods for use in agriculture, industry and medicine*, 64(10-11):1273–80, 2006. 14

[21] J. Pore. *An Examination of the Mixing of Low-Lying Excited 0+ States in 116Sn.* PhD thesis, 2013. 16

[22] Thermo Scientific. Thermo Scientific Neutron Generator Datasheet, http://www.thermoscientific.com/en/product/p-385-neutron-generator.html. Accessed: 2013. 16

[23] S. Tavernier. *Experimental Techniques in Nuclear and Particle Physics.* Springer, 2010. 18, 35

[24] G.F. Knoll. *Radiation detection and measurement.* Second edition, 1989. x, xiii, 19, 27, 34, 36, 53, 64

[25] W.N. English and G.C. Hanna. Grid ionization chamber measurements of electron drift velocities in gas mixtures. *Canadian Journal of Physics*, 1953. xiii, 24

[26] R. Bossingham. Calculated Drift Velocities for P10 using Magboltz2 V3.1, http://www.star.bnl.gov/public/tpc/ hard/tpcrings/p10_magboltz2.html. Accessed: 2012. xiii, xv, 25, 71, 73, 74

[27] S.F. Biagi. Monte Carlo simulation of electron drift and diffusion in counting gases under the influence of electric and magnetic fields. *Nuclear Instruments and Methods in Physics Research Section A: Accelerators, Spectrometers, Detectors and Associated Equipment*, 421(1-2):234–240, January 1999. xiii, 25

[28] P. Schattschneider. *Fundamentals of Inelastic Scattering.* Springer-Verlag, Wien-New York, 1950. 23

[29] O.R. Frisch. Isotope analysis of uranium samples by means of their α-ray groups. Unpublished report. *British Atomic Energy Project*, (BA-49), 1944. 29

[30] D. R. Lide, editor. *CRC Handbook of Chemistry and Physics.* CRC Press, 70th editi edition, 1990. 30

[31] J.F. Ziegler. SRIM-2003. *Nuclear Instruments and Methods in Physics Research Section B: Beam Interactions with Materials and Atoms*, 219-220:1027–1036, June 2004. x, xv, 30, 69, 70, 71, 75, 76, 77, 78

[32] National Institute of Standards and Technology. The NIST reference on constants, units, and uncertainty. CODATA value for alpha particle mass, http://physics.nist.gov/cgi-bin/cuu/Value?mal. Accessed: 2013. 30

[33] G.D. Alkhazov, A.P. Komar, and A.A. Vorob'ev. Ionization fluctuations and resolution of ionization chambers and semiconductor detectors. *Nuclear Instruments and Methods*, 48(1):1–12, February 1967. 35

[34] L. Meitner and O.R. Frisch. Products of the fission of the uranium nucleus. *Nature*, 143:471 – 472, 1939. 37

[35] O.R. Frisch. *What Little I Remember.* Cambridge University Press, 1979. 37, 38

[36] O.R. Frisch. Physical evidence for the division of heavy nuclei under neutron bombardment. *Nature*, 1939. 37

[37] Hans A. Bethe. Atoms and Nuclei. In *Atoms and Nuclei.* US Government, 1946. 38

[38] O.R. Frisch and R. Peierls. Radioactivity and sub-atomic phenomena. *Annual Reports on the Progress of Chemistry*, pages 7–32, 1939. 38

[39] O. Bunemann, T.E. Cranshaw, and J.A. Harvey. Design of grid ionization chambers. *Canadian Journal of Research*, 27:191 – 206, 1949. 38, 68

[40] I. Ogawa, T. Doke, and M. Tsukuda. The double-grid ionization chamber. *Nuclear Instruments and Methods*, 13:169–176, August 1961. xiii, xiv, 39, 40, 41

[41] H. Sann, H. Damjantschitsch, D. Hebbard, J. Junge, D. Pelte, B. Povh, D. Schwalm, and D.B. Tran Thoai. A position-sensitive ionization chamber. *Nuclear Instruments and Methods*, 124(2):509–519, March 1975. xiv, 41, 42

[42] G. Rosner, B. Heck, J. Pochodzalla, G. Hlawatsch, B. Kolb, and A. Miczaika. A new position measurement for ionization chambers. *Nuclear Instruments and Methods in Physics Research*, 188(3):561–569, October 1981. xiv, 41, 43

[43] C.R. Gruhn, M. Binimi, and R. Legrain. Bragg curve spectroscopy. *Nuclear Instruments and Methods in Physics Research*, 1982. xiv, 44

[44] Ch. Schiessl, W. Wagner, K. Hartel, P. Kienle, H.J. Körner, W. Mayer, and K.E. Rehm. A bragg-curve spectroscopy detector. *Nuclear Instruments and Methods in Physics Research*, 192(2-3):291–294, February 1982. xiv, 44, 45

[45] F. Gönnenwein. Recent developments of experimental techniques. *Nuclear Physics A*, 502:159–176, October 1989. xiv, 44, 45

[46] H.H. Knitter, C. Budtz-Jø rgensen, D.L. Smith, and D. Marletta. Angular distribution measurements for the reaction 6Li(n,t)4He. *Nucl. Sci. Eng*, 1982. 46

[47] C. Budtz-Jø rgensen, H.H. Knitter, Ch. Straede, F.-J. Hambsch, and R. Vogt. A twin ionization chamber for fission fragment detection. *Nuclear Instruments and Methods in Physics Research*, 258:209–220, 1987. xiv, 46, 59

[48] MKS Instruments. MKS Type 100B Mass-Flo Controller and M10MB Mass-Flo Meter Instruction Manual. Technical report. 49, 76

[49] MKS Instruments. PiPC PC99 Integrated Pressure Controller with Flow Meter Manual. Technical report. 49, 76

[50] MKS Instruments. MKS Baratron Type 722B Absolute Pressure Transducer. Technical report. 49

[51] R.C.A. Brown and D. Peach. Gas Control Technology II - DESY Systems. Technical report, 1982. 50

[52] J.H. Moore, C.C. Davis, and M.A. Coplan. *Building Scientific Apparatus*. Cambridge University Press, 4th edition, 2009. xiv, 52

[53] Cremat. CR-110 Charge Sensitive Preamplifier: application guide, http://www.cremat.com/CR-110.pdf. Accessed: 2013. 50

[54] J. Martin, C. Mercier, N. Starinski, C.J. Pearson, and P. Amaudruz. The TIGRESS DAQ / Trigger System. 55(1):84–90, 2008. 55

[55] D. Radford. RadWare Website: http://radware.phy.ornl.gov/gf3/gf3.html#3.1.2. 64

[56] A. Peisert and F. Sauli. Drift and diffusion of electrons in gases: A compilation. Technical report, CERN, Geneva, 1984. 71

Appendix A

Preamplifier Electronics Drawings

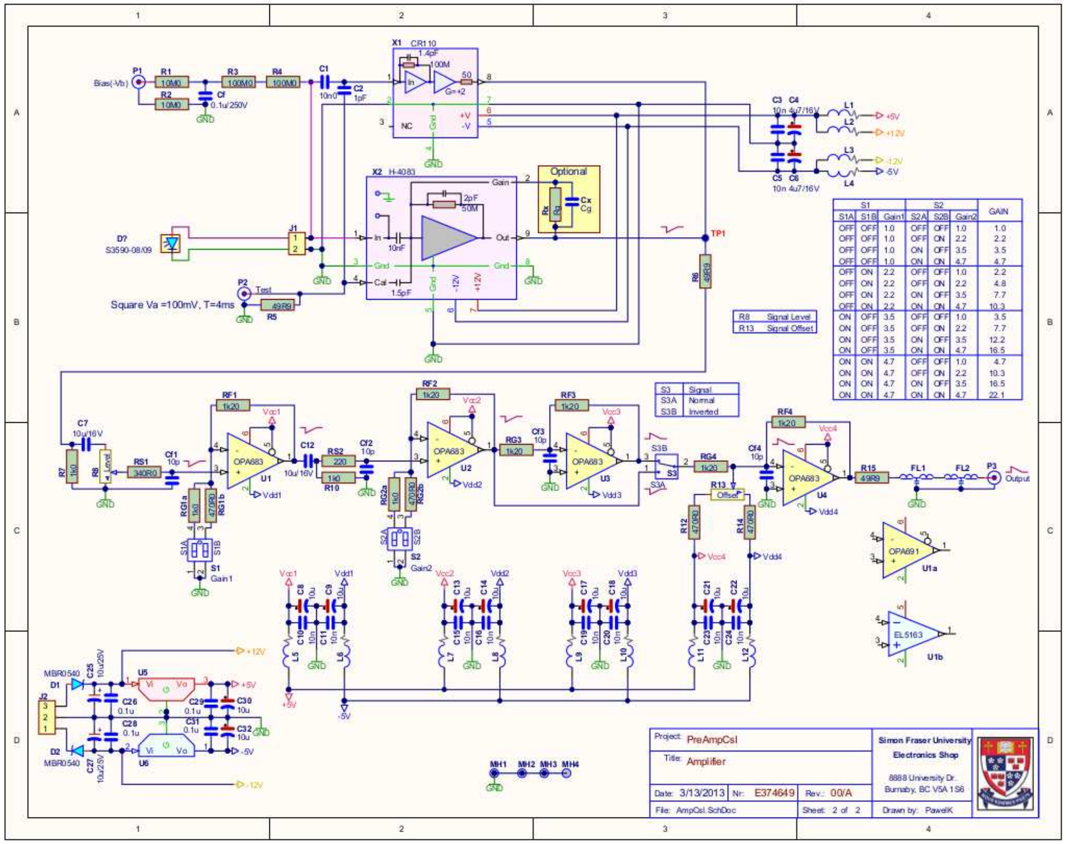

S1			S2			GAIN
S1A	S1B	Gain1	S2A	S2B	Gain2	
OFF	OFF	1.0	OFF	OFF	1.0	1.0
OFF	OFF	1.0	OFF	ON	2.2	2.2
OFF	OFF	1.0	ON	OFF	3.5	3.5
OFF	OFF	1.0	ON	ON	4.7	4.7
OFF	ON	2.2	OFF	OFF	1.0	2.2
OFF	ON	2.2	OFF	ON	2.2	4.8
OFF	ON	2.2	ON	OFF	3.5	7.7
OFF	ON	2.2	ON	ON	4.7	10.3
ON	OFF	3.5	OFF	OFF	1.0	3.5
ON	OFF	3.5	OFF	ON	2.2	7.7
ON	OFF	3.5	ON	OFF	3.5	12.2
ON	OFF	3.5	ON	ON	4.7	16.5
ON	ON	4.7	OFF	OFF	1.0	4.7
ON	ON	4.7	OFF	ON	2.2	10.3
ON	ON	4.7	ON	OFF	3.5	16.5
ON	ON	4.7	ON	ON	4.7	22.1

Figure A.1: Electrical drawing of the preamplifier made by the SFU Electronics workshop used for this work.